
DOWNSCALING DYNAMIC MAGNETIC SYSTEMS: FROM MICROSWIMMERS TO NANOROTORS

Dissertation

Christoph Pauer



Fakultät für Physik
der Ludwig-Maximilians-Universität München

München 2024

VERKLEINERUNG DYNAMISCHER
MAGNETISCHER SYSTEME: VON
MIKROSCHWIMMERN ZU NANOROTOREN

Fakultät für Physik
der Ludwig-Maximilians-Universität München

Dissertation

vorgelegt von

Christoph Pauer
geboren in Bad Mergentheim

München, 01.07.2024

Erstgutachter: Prof. Dr. Tim Liedl
Zweitgutachter: Prof. Dr. Pietro Tierno
Tag der mündlichen Prüfung: 06.09.2024

Zusammenfassung

Die Erforschung dynamischer magnetischer Mikro- und Nanosysteme kann zu futuristischen Anwendungen wie kontrollierbarer Botenstofftransport, Zellmanipulation und minimal invasive Operationen führen. Magnetische Systeme für die medizinische Anwendung sind deshalb so vielversprechend, da magnetische Felder in geringer Stärke keinen Einfluss auf biologische Systeme haben. Diese semi-kumulative Doktorarbeit zeigt die Verkleinerung magnetischer Systeme von $100\ \mu\text{m}$ auf $400\ \text{nm}$ in drei Schritten: von Mikroschwimmern auf einer Längenskala von $40\text{-}100\ \mu\text{m}$ über $2\text{-}3\ \mu\text{m}$ große Mikroschwimmer zu $400\ \text{nm}$ langen Nanorotoren. Diese Verkleinerung wurde durch die Kombination von DNA Origami und magnetischen Mikro- und Nanoteilchen realisiert. Durch seine beliebige Formbarkeit und chemische Addressierbarkeit kann DNA Origami sowohl als flexibler Schwanz für die Mikroschwimmer benutzt werden, als auch als Schablone zur Positionierung magnetischer Nanoteilchen für magnetische Nanorotoren. Die primären Ergebnisse dieser Dissertation sind im folgenden zusammengefasst:

1. Die vielseitige Herstellungsmethode des weichen Lithographieverfahrens ermöglicht die Erzeugung modularer magnetischer Mikroschwimmer mit verschiedenen Längen von $40\text{-}100\ \mu\text{m}$ und verschiedenen Formen der einzelnen Module. Die magnetischen Module werden durch ein statisches magnetisches Feld ausgerichtet und zusammengefügt, anschließend durch ein wackelndes magnetisches Feld zum Schwimmen angeregt. Die Geschwindigkeiten wurden abhängig von der Frequenz des Feldes und der Art des Schwimmers verglichen. Auch das kollektive Verhalten zahlreicher Schwimmer einer Schwimmerart wurde erforscht.

2. Magnetische Mikroteilchen wurden mit DNA Origami Filamenten dekoriert. Wenn ein externes wackelndes magnetisches Feld angelegt wird, zeigen die Teilchen abhängig des Bedeckungsgrades entweder diffuses oder ballistisches Verhalten. Die Orientierung der gerichteten Bewegung kann durch das Ausrichten des magnetischen Dipolmoments des magnetischen Teilchen mit der Bedeckung der Filamente zu einem gewissen Grad kontrolliert werden.

3. Ein einseitig an der Oberfläche befestigtes DNA Origami Filament kombiniert mit magnetischen Nanoteilchen wird mit rotierenden magnetischen Feldern zur Rotation angeregt. Durch die Ermittlung der kritischen Frequenz, wenn viskose und magnetische Kräfte gerade noch im Gleichgewicht sind, kann das magnetische Drehmoment, das auf

die Struktur wirkt, berechnet werden. Durch das Anlegen eines statischen magnetischen Feldes ist es möglich die Drehsteifigkeit der Struktur zu bestimmen.

Zusätzlich zu den magnetischen Themen beinhaltet diese Arbeit die Datenverarbeitungspipeline um die Farben und Farbveränderung einzelner Teilchen in Abhängigkeit ihrer Polarisierung aus Dunkelfeldmikroskopiebildern plasmonischer physikalischer unklonbarer Funktionen zu extrahieren.

Abstract

The research of dynamic magnetic micro- and nanosystem can lead to futuristic applications like targeted drug delivery, cell manipulation and minimal invasive surgery. Magnetic systems are promising for medical applications since biological systems are inert to magnetic fields at low field strength. This semi-cumulative dissertation shows the downscaling of magnetic systems from scales of 40-100 μm to 2-3 μm to 400 nm. The realization of this downscaling was due to the combination of DNA origami and magnetic micro- and nanoparticles. With its variability in design and chemical addressability, DNA origami can serve both as flexible tail for microswimmers and as template to position nanoparticles for nanorotors. The main results of this thesis are as follows:

1. The versatility of a soft lithographic approach enables the production of modular magnetic microswimmers with variable lengths of 40-100 μm . The magnetic modules are aligned and assembled by a static magnetic field, before actuating the swimmers by a wagging magnetic field. The velocities depending on the frequency of the field and type of swimmer were compared. Additionally, the collective behavior of one type of swimmers was investigated.

2. Magnetic microbeads were decorated with DNA origami appendages. Depending on the particle's surface coverage, they displayed either Brownian or ballistic behavior when applying a wagging magnetic field. The orientation of the ballistic motion can be controlled to a certain degree by aligning the easy axis of the magnetic bead perpendicular to side of the DNA origami attachment.

3. Magnetic nanoparticles were attached to a DNA origami appendage mounted on one side to a surface. To rotate this compound structure, an external rotary magnetic field was applied. By determining the critical frequency of the rotor, where viscous and magnetic forces are still balanced, it is possible to calculate the magnetic torque acting on the structure. Applying a static magnetic field can reveal the rotors torsional stiffness.

In addition to the magnetic projects, this thesis includes a data processing pipeline to extract the colors and track the color changes of individual particles depending on the polarization measured via darkfield microscopy for plasmonic physical uncloneable functions.

Publications

Publications based on the results of this thesis

[1] **Pauer, C.**, Du Roure, O., Heuvingh, J., Liedl, T., & Tavecchi, J. (2021). Programmable design and performance of modular magnetic microswimmers. *Advanced Materials*, 33(16), 2006237.

[2] **Pauer, C.**, Venczel, A., Dass, M., Liedl, T., & Tavecchi, J. (2022). Propulsion of magnetic beads asymmetrically covered with DNA origami appendages. *Advanced Materials Technologies*, 7(12), 2200450.

[3] Lak, A., Wang, Y., Kolbeck, P. J., **Pauer, C.**, Chowdhury, M. S., Cassani, M., & Lipfert, J. (2024). Cooperative dynamics of DNA-grafted magnetic nanoparticles optimize magnetic biosensing and coupling to DNA origami. *Nanoscale*, 16(15), 7678-7689.

[4] Dass, M., Raab, L., **Pauer, C.**, Sikeler, C., Heinze, L., Tavecchi, J., & Liedl, T. (2023). Self-assembled physical unclonable function labels based on plasmonic coupling. *arXiv preprint arXiv:2310.19587*.

Further publications

[5] Junot, G., Leyva, S. G., **Pauer, C.**, Calero, C., Pagonabarraga, I., Liedl, T., & Tierno, P. (2022). Friction Induces Anisotropic Propulsion in Sliding Magnetic Microtriangles. *Nano Letters*, 22(18), 7408-7414.

Contents

1. Introduction	11
2. Fundamentals	13
2.1. Magnetic particles	13
2.1.1. Types of magnetism	13
2.1.2. Magnetic interactions in a liquid	15
2.2. Swimming at low Reynolds numbers	17
2.2.1. Sperm number	18
2.2.2. Mason number	20
2.2.3. Artificial swimmers	21
2.3. Colloids	24
2.4. DNA and DNA Nanotechnology	27
2.4.1. DNA	27
2.4.2. DNA nanotechnology	28
2.4.3. Nanomachine actuations	30
3. Experimental methods	33
3.1. Shape-casting with superparamagnetic dispersion	33
3.2. Folding DNA Origami	34
3.3. Functionalization of nanoparticles	35
3.4. Purification	36
3.5. PEG surface modification	37
3.6. Visualization methods	37
3.6.1. Brightfield microscopy	37
3.6.2. DFM - Darkfield Microscopy	38
3.6.3. TIRFM - Total Internal Reflection Fluorescence Microscopy	38
3.6.4. Resolution of DFM and TIRFM	39
3.6.5. TEM - Transmission Electron Microscopy	40
3.7. Magnetic setups	40

4. P1: Programmable Design and Performance of Modular Magnetic Microswimmers	43
5. P2: Propulsion of Magnetic Beads Asymmetrically Covered with DNA Origami Appendages	55
6. Magnetic nanorotor	65
6.1. Rotation	66
6.2. Clamping	69
7. Data analysis of darkfield images and videos	71
7.1. PUF fabrication	71
7.2. Image/video processing and analysis	72
7.2.1. Image processing and hue analysis of plasmonic PUFs	72
7.2.2. Polarization dependent color change	73
8. Conclusion and future directions	77
A. Appendix	79
A.1. Supporting Information for Publication P1	79
A.2. Supporting Information for Publication P2	91
A.3. Protocols	102
A.4. Magnetic nanoswitch	109
A.5. Scripts	112
Bibliography	120

1. Introduction

Mobility and transport of microorganisms in fluids are fundamental aspects of life enabling microorganisms to search for food, orient towards light, spread offspring, and form colonies, all of which are crucial for their survival and reproduction [6]. At the microscale, where viscous forces dominate over inertial forces, locomotion is only achieved through non-reciprocal movement patterns. Propulsion mechanisms developed by nature to overcome this challenge include the rotating helical flagella [7] used by many bacteria and the snake-like motion utilized by spermatozoa [8]. Inspired by nature, artificial microswimmers have been developed being driven [9] either by a fueled or a fuel-free approach. The fueled approach requires the presence of fuel, i.e. hydrogen peroxide (H_2O_2), for propulsion [10]. This work concentrates on a fuel-free approach operating with external magnetic fields.

Magnetic particles are a crucial building block in order to build artificial magnetic microswimmers. These particles are developed to be used in wide range of technical applications such as biosensing [11], targeted drug delivery [12][13], contrast agents in magnetic resonance imaging (MRI) [14][15] or water purification[16].

Experimental and theoretical background in what has been achieved in these different research areas are elucidated in chapter 2. It starts with the fundamentals of magnetism, followed by the basics of movement at low Reynolds number and some examples of artificial microswimmers. After that, the different types of interactions in colloidal dispersions are discussed, finished by DNA nanotechnology and its actuation methods.

The experimental methods used to achieve the results for this thesis are described in chapter 3, explicitly the production of superparamagnetic dispersions, DNA origami folding, functionalization of metallic and magnetic nanoparticles, purification methods such as gel electrophoreses and PEG precipitation and visualization methods such as bright-field microscopy (BF), darkfield microscopy (DFM), total internal reflection fluorescence microscopy (TIRFM) and transmission electron microscopy (TEM).

Chapter 4-6 lay down the results for the magnetic projects. Chapter 4 presents a soft lithographic approach for the simultaneous production of modular magnetic microswimmers, ranging from 40-100 μm . In chapter 5, magnetic microbeads are asymmetrically

covered to fabricate microswimmers on the single digit microscale. Combining magnetic nanoparticles with DNA origami in order to realize a magnetic nanorotor is explained in chapter 6.

In chapter 7, a data processing and visualization pipeline is explained to harvest the individual colors of optical responsive physical uncloneable functions (PUF).

An outlook to what can be done in the future using this thesis's findings are discussed in chapter 8.

2. Fundamentals

2.1. Magnetic particles

2.1.1. Types of magnetism

Electrons carry magnetic dipole moments due to their atomic spin and orbital momentum. The magnetic property of any given material originates from the contribution of all individual magnetic dipole moments from its electrons. The magnetization \mathbf{M} of a material can be calculated with the magnetic susceptibility χ_m , a scalar in the simplest case, and the magnetic field strength \mathbf{H} . Typically, for small field strengths, this relationship is linear [17]:

$$\mathbf{M} = \chi_m \mathbf{H} \quad (2.1)$$

The magnetic field \mathbf{B} stands in relation with the magnetic field strength \mathbf{H} by:

$$\mathbf{B} = \mu(\mathbf{H} + \mathbf{M}) \quad (2.2)$$

with μ being the permeability. Most of the time, the system of interest is outside of a magnetized body, so $\mathbf{M} = 0$ and $\mathbf{B} = \mu\mathbf{H}$. The magnetization of a particle $\mathbf{M} = \mathbf{m}/V$ depends on its magnetic moment \mathbf{m} and its volume V .

Materials, which are not magnetized in the absence of a magnetic field are materials without magnetic order and respond very weakly to external magnetic fields. Such materials are considered *non-magnetic* and can have any state of matter. *Diamagnetic* materials induce magnetic dipoles in the opposite orientation of the applied field, so the resulting magnetic field inside the material is weaker than the applied magnetic field. Examples are hydrogen, noble gases and copper. The magnetic dipoles in *paramagnetic* materials are oriented in random directions with zero net magnetization for most time windows. When an external magnetic field is applied, the dipoles align with the orientation of the magnetic field and enhance it. Examples of paramagnetic materials are sodium, oxygen and aluminum.

Some solid state materials exhibit magnetic order meaning they can keep their magne-

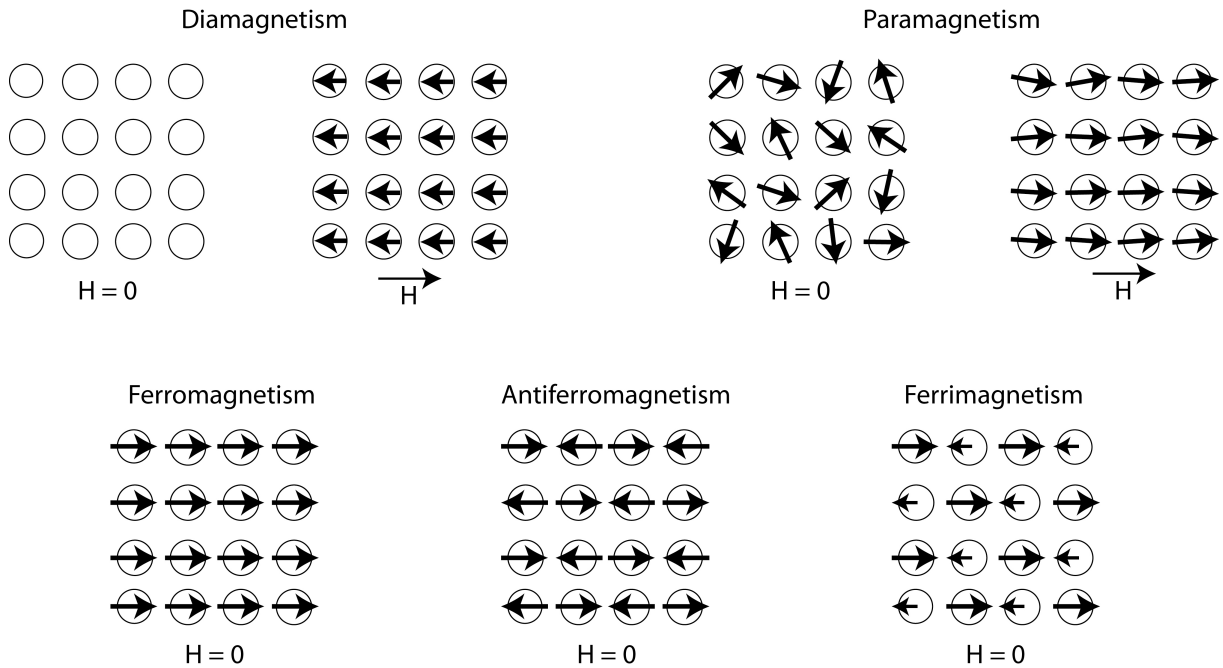


Figure 2.1.: Schematic of the magnetic dipole orientation for different types of magnetic materials, with or without an applied magnetic field H . Image adapted from [19].

tization in absence of an external magnetic field (figure 2.1) and they respond strongly to external magnetic fields. The maximal magnetization of a material is achieved when all magnetic dipoles are aligned with the external field. This saturated magnetization M_S and the ability to keep their magnetization without an applied magnetic field M_r lead to the typical hysteresis curve (figure 2.2). Magnetically ordered materials in absence of a magnetic field can be ordered parallel and antiparallel. *Ferromagnetic* materials align their magnetic dipoles parallel leading to a highly positive magnetization. Examples are iron, nickel and cobalt. In contrast, *antiferromagnetic* and *ferrimagnetic* materials have antiparallel coupling. The dipoles of ferrimagnetic materials are weaker in one direction, resulting in a net magnetization. Antiferromagnetic materials most of the time have a net magnetization of zero due to the antiparallel coupling. The material can have a non-zero magnetization only in cases of spin canting the material. A materials magnetization can be reduced to zero by either heating the material over the curie temperature [18] or exposing it to an external magnetic field H_c called coercivity field [19].

In ferromagnetic materials, neighboring spins pointing in the same direction form domains. A particle small enough, 5-100 nm for Fe_3O_4 [20], consists only of a single domain where the domains orientation can flip randomly due to thermal fluctuation. Such *superparamagnetic* particles have a magnetization of zero when the external field is zero.

In this thesis, superparamagnetic iron oxide (Fe_2O_3) nanoparticles and ferrimagnetic cobalt doped iron nanoparticles were employed.

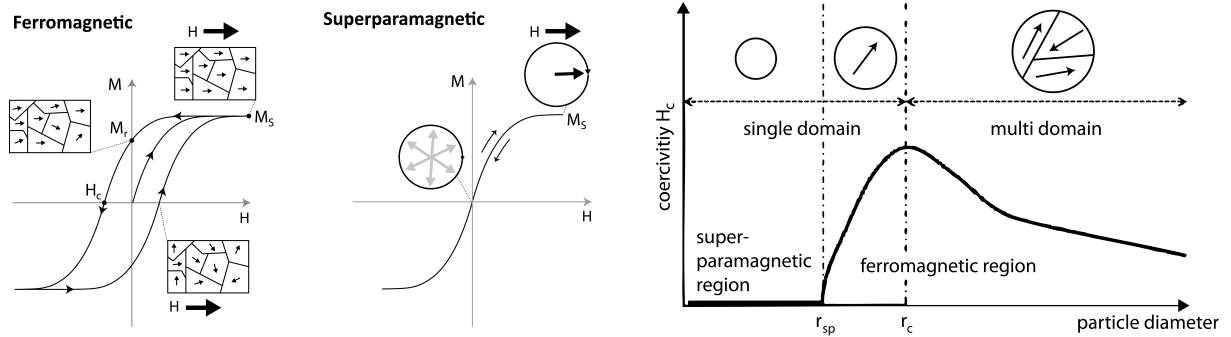


Figure 2.2.: Magnetization M depending on the magnetic field strength H for **a** ferromagnetic materials and **b** superparamagnetic particles. **c** shows the coercivity field H_c needed to remove a magnetic particles magnetization in dependence of its parameter. **c** was adapted from [21].

2.1.2. Magnetic interactions in a liquid

In a collection of magnetic particles, each particle experiences a local magnetic field caused by the magnetic moment of its neighboring particle. The magnetic interaction potential U_m of two particles in the point dipole approximation with magnetic moments \mathbf{m}_i , \mathbf{m}_j and the interparticle distance of r_{ij} is given by [17]:

$$U_m = \frac{\mu_m}{4\pi} \left(\frac{\mathbf{m}_i \cdot \mathbf{m}_j}{r_{ij}^3} - \frac{3(\mathbf{m}_i \cdot \mathbf{r}_{ij})(\mathbf{m}_j \cdot \mathbf{r}_{ij})}{r_{ij}^5} \right) \quad (2.3)$$

where μ_m is the magnetic permeability of the dispersion medium. In the special case of the two particles in the point dipole approximation having the same magnetic moment \mathbf{m} , equation 2.3 reduces to:

$$U_m = -\frac{\mu_m m^2}{2\pi r_{ij}^3} P_2(\cos \theta) \quad (2.4)$$

with $P_2 = (3x^2 - 1)/2$ being the second-order Legendre polynomial and θ being the angle between \mathbf{m} and \mathbf{r}_{ij} . At the magic angle $\theta_m = 54.7^\circ$ [22] the magnetic interaction disappears. For angles lower than θ_m , the potential is attractive, for higher angles it is repulsive. This effect can be used so assemble magnetic compound structures by the application of a static field [23].

Besides static assemblies, rotating magnetic fields can be used to induce rotation into

magnetic particles in a liquid. The magnetic torque \mathbf{T}_m acting on a particle is [24]:

$$\mathbf{T}_m = \mu_m(\mathbf{m} \times \mathbf{H}) \quad (2.5)$$

At low Reynolds numbers (see section 2.2), the magnetic torque and the viscous torque counteract each other resulting in a torque balance:

$$\mathbf{T}_m + \mathbf{T}_v = 0 \quad (2.6)$$

with the viscous torque \mathbf{T}_v being:

$$\mathbf{T}_v = -\zeta\Omega \quad (2.7)$$

where ζ is the rotational friction coefficient and Ω the angular velocity. When a rotational magnetic field is applied to a magnetic particle, it rotates synchronously with the external field up to a critical frequency f_c . For higher frequencies than f_c , the viscous forces dominate and lead to a back-and-forth motion of the particle, resulting in an overall lower rotating frequency [25].

In the special case of a magnetic rod rotating with the critical frequency f_c in a Newtonian fluid, the torque acting on the rod T_r can be calculated by the following equation [26]:

$$T_r = 2\pi\gamma f_c \quad (2.8)$$

where γ is the drag constant of the rod. When the viscosity η of the liquid is known, the drag constant γ can be calculated by:

$$\gamma = \frac{\eta L^3 \pi}{3 \ln\left(\frac{L}{D}\right) - A} \quad (2.9)$$

with the rod length L , the rod thickness D and $A \approx 2.4$ [27].

While a uniform magnetic field can induce torques, it does not create a translational force. For that, a magnetic field gradient is required. The attractive magnetic force \mathbf{F}_m on the magnetic moment \mathbf{m} from the magnetic field \mathbf{B} can be written as [28]:

$$\mathbf{F}_m = \nabla(\mathbf{m} \cdot \mathbf{B}) \quad (2.10)$$

2.2. Swimming at low Reynolds numbers

Time doesn't matter. The pattern of motion is the same, whether slow or fast, whether forward or backward in time.

- The scallop "theorem" [29]

In nature, there are two main approaches to swimming at low Reynolds number are *the flexible oar* and *the corkscrew*.

Spermatozoon is a typical example of a *flexible oar*. It propels by inducing a sinoidal wave at the head which then propagates through the tail (figure 2.3a).

Prokaryotic cells, like bacteria, generally use *the corkscrew* approach for locomotion. Depending on the species, a bacterium has one or several left handed helical filaments called flagellum/flagella. A rotary motor inside the bacterial cell wall is connected to the flagellum via a flexible hook. To propel forwards, the flagellum rotates counterclockwise screwing through the liquid. If the bacterium has more than one flagellum, they arrange themselves into a bundle which acts then as one big flagellum (figure 2.3b) .

To describe the dynamics of an incompressible fluid, e.g. water, surrounding microswimmers, the hydrodynamic equations developed by Navier and Stokes can be applied [30]:

$$\nabla \cdot \mathbf{v} = 0, \quad (2.11)$$

$$\rho \left(\frac{\partial \mathbf{v}}{\partial t} + \mathbf{v} \cdot \nabla \mathbf{v} \right) = \eta \nabla^2 \mathbf{v} - \nabla p \quad (2.12)$$

with ρ being the fluid density, η being the viscosity of the fluid, $\mathbf{v}(\mathbf{r}, t)$ is the position- and time-dependent fluid velocity field and $p(\mathbf{r}, t)$ is the pressure field. Bringing equation 2.12 into a dimensionless form by introducing $v = U\mathbf{v}'$, $\mathbf{x} = L\mathbf{x}'$, $t = Lt/U$ and $p = \eta U/L \cdot p'$ with the dimensionless velocity \mathbf{v}' , position \mathbf{x}' , time t' and pressure p' and the characteristic velocity U and the characteristic length L results in:

$$Re \left(\frac{\partial \mathbf{v}'}{\partial t'} + \mathbf{v}' \cdot \nabla' \mathbf{v}' \right) = \nabla'^2 \mathbf{v}' - \nabla' p' \quad (2.13)$$

with Re being the Reynolds number [31]:

$$Re \equiv \frac{UL\rho}{\eta} \quad (2.14)$$

The Reynolds number is a dimensionless number and gives the relation between inertial and viscous forces. For $Re > 1$ the inertial forces dominate and for $Re < 1$ the viscous

forces dominate. For example, a human swimming in water with $U = 2$ m/s, $L = 2$ m, $\rho = 1000$ kg/m³ and $\eta = 1$ mPas has a Reynolds number of $Re = 4 \cdot 10^6$. An Escherichia Coli bacterium swimming in water with $U = 30$ μ m/s, $L = 1$ μ m, has an Reynolds number of $Re = 30 \cdot 10^{-6}$.

For small Reynolds numbers $Re \ll 1$, equation 2.13 reduces to the Stokes equation as the inertial terms can be neglected [30]. For better readability, the primes are dropped:

$$\nabla p - \eta \nabla^2 v = 0 \quad (2.15)$$

Equation 2.15 is time independent, therefore inertia based movement patterns, for example when scallops open their shells slowly and close them fast, cannot be used to generate propulsion. Generally, reciprocal patterns like this cannot be used to drive motion at low Reynolds numbers, the patterns have to be non-reciprocal. A simple example for non-reciprocal movement pattern introduced by Purcell is a two hinged swimmer. The two arms of the swimmer can each move around their pivot points with an angle θ_1 and θ_2 (figure 2.3c). Depending on the amplitude of the angles, the swimmer can swim forwards, backwards or rotate [32].

When an external force field $\mathbf{f}(t)$ is applied to the system, i.e. a magnetic field, equation 2.15 turns into [30]:

$$\nabla p - \eta \nabla^2 v = \mathbf{f}(t) \quad (2.16)$$

This implies that the external forces act against the viscous forces.

2.2.1. Sperm number

The swimmers studied in this thesis are of the kind *flexible oar*. Their way of swimming can be approximated as a flexible filament being periodically oscillated at one end with an amplitude y_0 and a angular frequency $\omega = 2\pi f$ (figure 2.4a). The displacement h from the horizontal axis depends highly on the sperm number S_p , also known as re-scaled polymer length, a dimensionless parameter which describes the relation of viscous and bending forces [33].

$$S_p = l \left(\frac{\omega \zeta_{\perp}}{A} \right)^{\frac{1}{4}} = \frac{l}{l_{eh}(\omega)} \quad (2.17)$$

with the viscous drag coefficients ζ_{\parallel} and ζ_{\perp} parallel and perpendicular to the long axis of a slender body, with l being the objects length and a its the radius while $l \gg a$:

$$\zeta_{\parallel} = \frac{2\pi\eta}{\ln(\frac{l}{a}) + C_1} \quad \text{and} \quad \zeta_{\perp} = \frac{4\pi\eta}{\ln(\frac{l}{a}) + C_2} \quad (2.18)$$

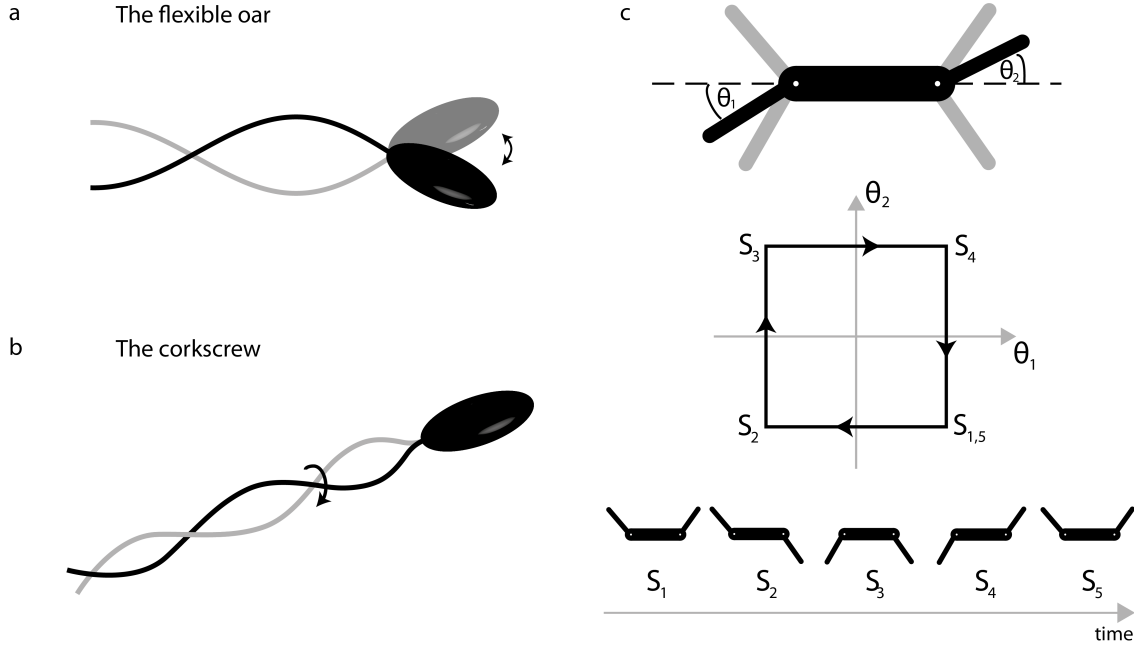


Figure 2.3.: Schematics of **a** the flexible oar and **b** the corkscrew swimmer. **c** shows the two hinged swimmer proposed by Purcell and its different configuration in its non-reciprocal movement pattern. Images inspired by [29].

$l_{eh}(\omega)$ is the elastohydrodynamic penetration length and C_i is a constant depending on the shape of the body. The bending stiffness $A = k_B T l_p$ depends on the thermal energy $k_B T$, consisting of the Boltzmann constant k_B and the temperature T , and the persistence length l_p .

The swimming velocity (figure 2.4b) depending on the sperm number for small amplitudes y_0 was introduced by Lagomarsino et al. [33]:

$$v = \left(1 - \frac{\zeta_{\perp}}{\zeta_{\parallel}}\right) \frac{y_0^2 \omega}{4\sqrt{2}L} \Upsilon(S_p) \quad (2.19)$$

with the scaling function $\Upsilon(S_p)$ [34] being responsible for the characteristic shape of the graph. The following observations can be made on the graph in figure 2.4b:

- $S_p < 4$: Filament oscillates around a pivot point exhibiting close to reciprocal movement patterns, therefore the swimming speed goes to zero. $S_p = 2.45$ is plotted in figure 2.4c.
- $S_p \simeq 4$: greater than the length of the filament leading to maximal swimming velocities. $S_p = 4.29$ plotted in figure 2.4d.

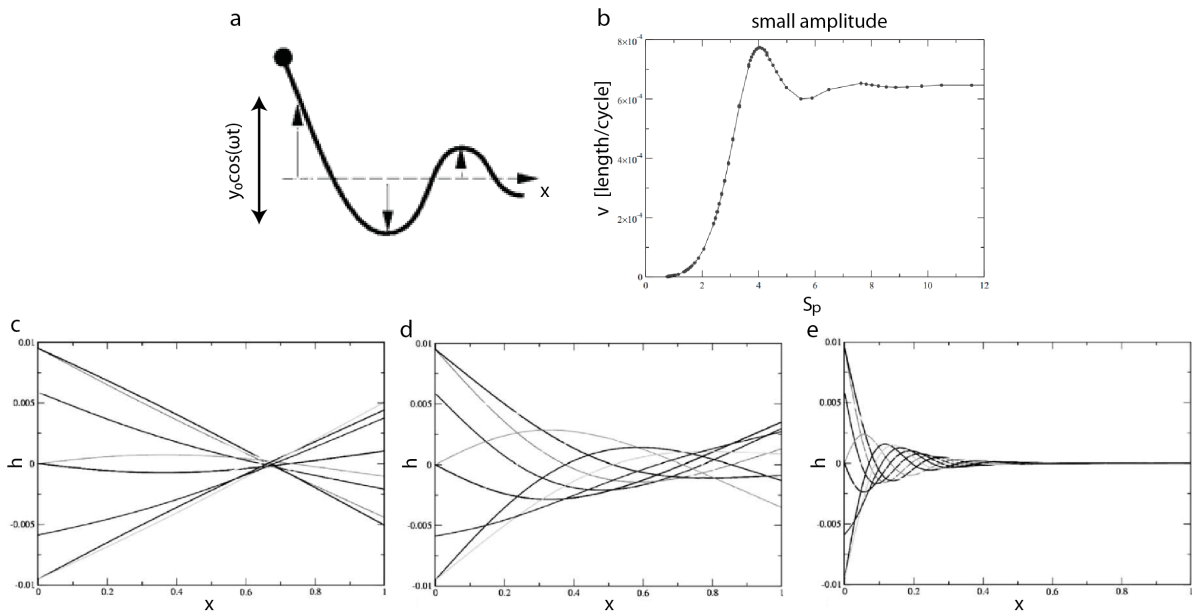


Figure 2.4.: **a** Schematic of an elastic filament oscillated at one end with an amplitude y_0 . **b** Swimming velocity depending on sperm number for small y_0 . Resulting waveforms of the filaments displacement $h(x)$ for different sperm numbers are shown in **c** $S_p = 2.45$, **d** $S_p = 4.29$ and **e** $S_p = 22.61$. Images adapted from **a** [34] and **b-e** [33].

- $S_p \gg 4$: Bend in the filament allows non-reciprocal movement patterns. The swimming velocity plateaus at sub maximal values. $S_p = 22.61$ plotted in figure 2.4e.
- Swimming is not possible when $S_p = 0$ or the drag coefficients $\zeta_{\parallel} = \zeta_{\perp}$.

For larger amplitudes, the plateau for higher sperm numbers drops (figure 2.5a). The wave pattern of an oscillating constraint for the optimal case $S_p = 4$ with an amplitude of $y_0 = 0.6l$ is shown in figure 2.5b.

In this thesis, microswimmer with flexible non-magnetic tails with the potential to create small and large amplitudes y_0 are subject to publication P2 (chapter 5).

2.2.2. Mason number

The swimmers in publication P1 (chapter 4) completely consist of magnetic material and thus can be approximated as magnetic filaments. In cases where the bending forces can be neglected, the relation between the magnetic forces and the viscous forces for a magnetic filament can be described by the Mason number M_a [35]:

$$M_a = \frac{\text{viscous force}}{\text{magnetic force}} = \frac{\zeta_{\perp} \omega \mu_0 l^2}{(aB\chi_e)^2} \quad (2.20)$$

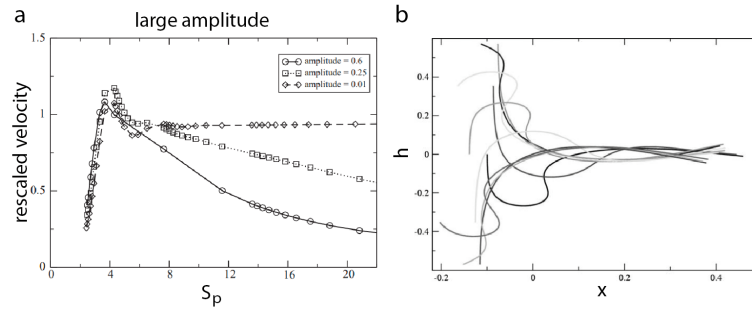


Figure 2.5.: **a** Rescaled velocity depending on the sperm number S_p . **b** Wave pattern of a filament with with $S_p = 4$ displaced with $y_0 = 0.6l$. Images adapted from [33].

with the permeability of free space μ_0 , the filaments radius a and magnetic volume susceptibility χ_e . Analogous to the Sperm number, the square root of the mason number M_a is approximately the filament length l divided by the magnetoviscous length l_{mv} , which is the distance over which the influence of the magnetic field significantly alters the flow characteristics of a fluid.

$$\sqrt{M_a} \approx \frac{l}{l_{mv}} \quad (2.21)$$

This implies the following for the wave pattern of a magnetic filament:

- $\ll 1$: The viscous forces are dominant and magnetic forces have almost no influence on a magnetic swimmer. Therefore only the tips of the swimmer might be able to follow the magnetic, resulting in tip wagging and little to no swimming.
- $\gg 1$: The magnetic forces are dominant, therefore the filament exhibits reciprocal movement patterns like a rigid rod, therefore no swimming.
- $\simeq 1$: When the forces are balanced, the filament can exhibit non-reciprocal movement pattern via bending, which enables swimming.

2.2.3. Artificial swimmers

As mentioned, swimming at low Reynolds numbers is a challenge that nature has solved. Towards creating artificial micro- or nanorobots that can perform controlled movements at the nanoscale, humankind has been greatly inspired by nature's solutions. Next to the fundamental physics that can be explored with these systems, one keyword being collective motion [36][37], several futuristic applications come to mind like targeted drug delivery [38][39], cell manipulation [40][41] and minimal invasive surgery [42][43]. In the last two decades, multiple variations of swimmers were developed, grouped below into four categories (figure 2.6).

Stiff helical *corkscrew swimmers* can be fabricated by different methods [44][45][46] at different sizes, ranging from $1.5 \mu\text{m}$ to $50 \mu\text{m}$ (figure 2.6a-c). These swimmers are generally controlled by an external rotating magnetic field. Through the rotation the helices drilling through the surrounding fluid like a corkscrew enabling them to propel forwards or backwards, depending on their chirality and the direction of rotation.

Swimming Janus particles are named after Janus, the roman god of the beginning and end, known for his two faced head. Janus particles have two sides consisting of different materials, where each side reacts different to an external stimulus enabling the particle to propel. Such particles are not necessarily spherical [10], they can be rectangular [47] or tree-like [48] as well (figure 2.6d-f). Their sizes can range from half a micrometer [10] to centimeters [47].

Flexible oar swimmers propel via a propagating wave through the body. These types of swimmers are typically actuated by a wagging magnetic field when incorporating some magnetic materials (figure 2.6g,h,j) [49][50][51]. An non-magnetic actuation approach is by the usage of contractile cells at the intersection of head and tail to induce the propagating wave (figure 2.6i) [52]. The sizes of such swimmers range from $20 \mu\text{m}$ to 15 mm.

A magnetic particle loosely connected to a non-magnetic particle via a flexible silver bridge is actuated by a rotating magnetic field. The field rotates the magnetic part of the swimmer which induces rotation with a amplitude and phase difference into the non-magnetic part. The two rotations with different phase and amplitude prove to be a non-reciprocal pattern, which enables swimming (figure 2.6k) [53]. Another type of swimmer propels by periodic light induced deformations (figure 2.6l) [54].

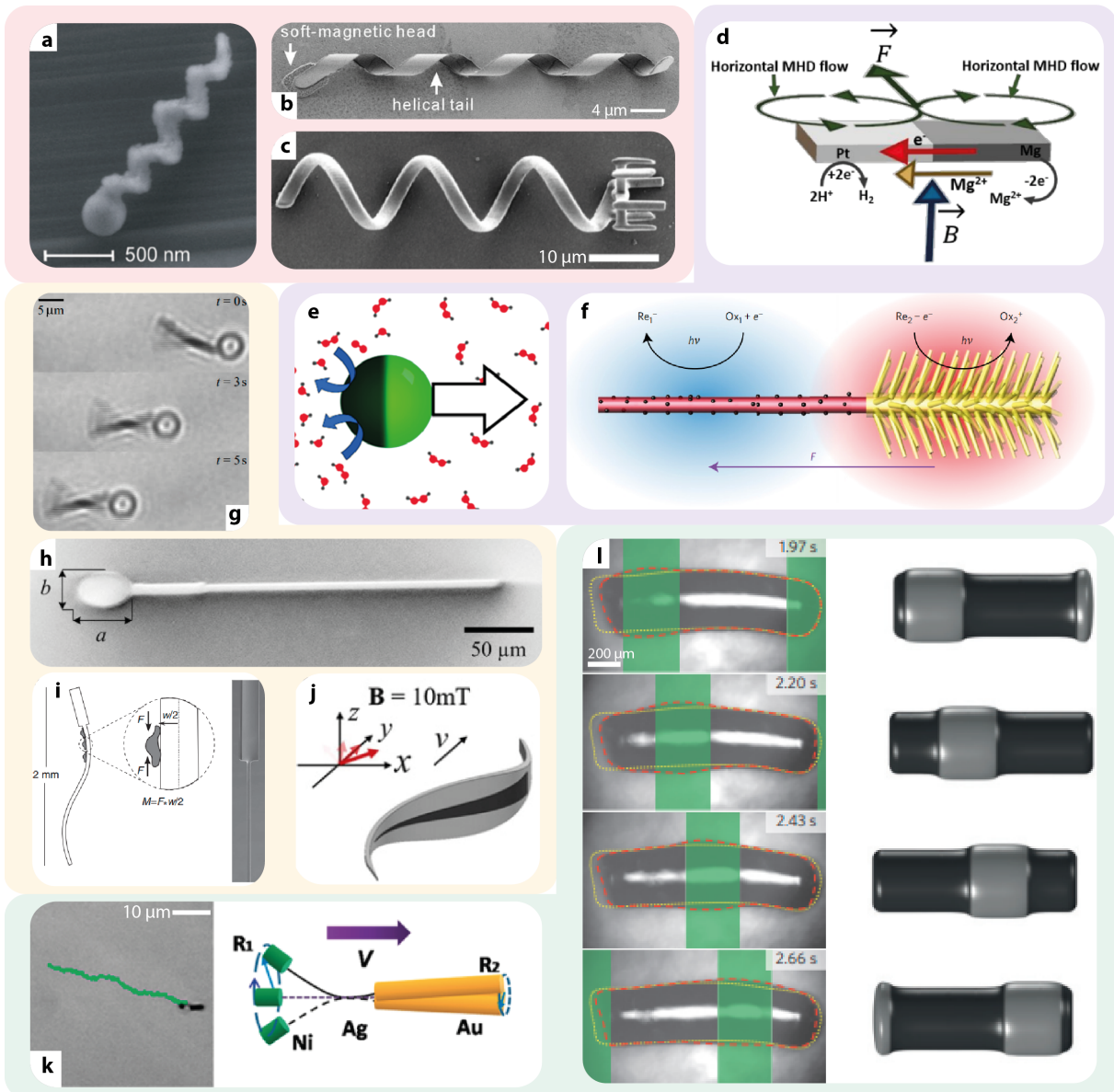


Figure 2.6.: Examples of **a-c** corkscrew swimmers: **a** Glancing angle deposition fabricated SiO_2 nanostructured propellers, made magnetic by a 30 nm layer of cobalt deposited via thermal evaporation [44]. **b** Top down multilayer process fabricated swimmers, wet etching of sacrificial layer results in a helical twisted structure with a thin Cr/Ni/Au film as soft magnetic head [45]. **c** 3D direct laser writing and physical vapor deposited helical micromachines, consisting of SU-8 or IP-L coated with Ni/Ti for magnetic properties [46]. **d-f** Swimming Janus particles: **d** Mg/Pt Janus particle consisting of a magnesium and a platinum foil attached together. In acidic solutions, oxidation of Mg and reduction of H_3O^+ on Pt occur spontaneously. In case of Mg, a net flux of ions from metal to bulk is produced. For Pt, the ion flux goes from the bulk to the metal. When a magnetic field is applied orthogonal to the Janus particles surface, a Lorentz force is induced, creating two macro-MHD (magnetohydrodynamic effect) vortices visualized by the green arrows. The vortices produce an overall amplified horizontal driving force F at the center of the swimmer that can be used for propulsion [47].

Figure 2.6.: **e** A Janus colloid hemispherically coated with platinum moves in hydrogen peroxide due to the catalysis of the reaction $2\text{H}_2\text{O}_2 \rightarrow \text{H}_2\text{O} + \text{O}_2$. The catalytically formed gas bubbles detach from the platinum, driving the particle in the direction of the non-catalytic side of the colloid. Smaller diameters of particles exhibit higher velocities, with the maximum around $36 \mu\text{m/s}$ at a diameter of $0.5 \mu\text{m}$ [10]. **f** The nanotree, with a long axis of around $10 \mu\text{m}$, consists of TiO_2 nanowires (yellow), acting as photoanode, grown on silicon nanowire (pink), the photocathode. Platinum nanoparticles (black) on the silicon wire serve as a electrocatalyst. On illumination, photoelectrochemical (PEC) reactions generate asymmetrically distributed charged PEC products propelling the nanotree by electrophoresis [48]. **g-i** Flexible oar swimmers: **g** The Dreyfus swimmer consists of a flexible magnetic filament which is attached to a red blood cell. The filament is composed of magnetic beads connected via DNA strands [49]. **h** The swimmers head consists of an ellipsoidal CoNi core surrounded by exposed SU-8 and its tail purely consists of SU-8 [50]. **i** Contractile cells added to the interface between head and tail of a PDMS skeleton. Periodic contraction of the cells generate a bending wave, propagating through the tail and propelling the swimmer [52]. **j** Magnetic fish-like microrobot, with a long axis of $15 \mu\text{m}$, composed of a magnetic flexible skeleton (ecoflex and NdFeB particles) with encoded magnetization and a non-magnetic soft body (ecoflex) [51]. **k,l** Other: **k** Flexible nanowire with a gold head and a nickel tail connected by a partially dissolved silver bridge can be magnetically driven. When an external rotating magnetic field is applied, a cone-shaped rotation of the nickel segment is created leading to the rotation of the gold segment at different amplitudes and with a phase difference [53]. **l** A cylinder consisting of liquid crystal elastomers (LCE) changes its thickness when irradiated by light. A traveling wave moving from left to right creates a non-reciprocal deformation propelling the swimmer [54]. All images are adapted from their referred original publications.

2.3. Colloids

Liquid or solid particles sizing from around 10 nanometer to several micrometer [55] dispersed in a medium (gas, liquid) are called colloids or colloidal dispersions. Some variations are mist (liquid/gas), smoke (solid/gas), foam (gas/liquid), emulsion (liquid/liquid) and suspension (solid/liquid). The dispersed particles can be of any shape and any material, including magnetic materials. Colloidal particles can be used as model to understand collective effects in atomic systems as they are small enough to get influenced by thermal fluctuations but big enough to measure them with common microscopy techniques and their interactions can be tuned from attractive, repulsive and hard-sphere like [56].

In a colloidal dispersion, attractive forces lead to aggregation and repulsive forces prevent it. The force acting on a particle can be derived from the interaction potential $U(r)$

[57]:

$$F(r) = -\frac{dU(r)}{dr} \quad (2.22)$$

Van der Waals interactions

Van der Waals interactions describe the attractive interaction between permanent or fluctuating dipoles. In the case of two identical spheres with radius R and interparticle distance D , the van der Waals interaction potential is:

$$U_A(D) = -\frac{A_H}{12D}R \quad (2.23)$$

with the nonretarded Hamaker constant A_H for the symmetric case of two identical phases 1 interacting across a medium 3 :

$$A_H = \frac{3}{4}k_B T \left(\frac{\epsilon_1 - \epsilon_3}{\epsilon_1 + \epsilon_3} \right)^2 + \frac{3h_p \nu_e (n_1^2 - n_3^2)^2}{16\sqrt{2} (n_1^2 + n_3^2)^{3/2}} \quad (2.24)$$

where ϵ_i, n_i are the dielectric constant and the refractive index of medium i , h_p is the Planck constant and ν_e is the electronic absorption frequency. Minimizing the attractive van der Waals forces to prevent aggregation can be achieved by minimizing the nonretarded Hamaker constant by matching the refractive indices of the two materials.

Electrostatic interactions

Particles with the same charge repel each other with the interaction potential of

$$U_C(r) = \frac{q_1 q_2}{4\pi\epsilon\epsilon_0 r}, \quad (2.25)$$

where ϵ_0 is the dielectric permittivity in a vacuum, ϵ is the relative permittivity or dielectric constant, which is material dependent, q_i is the electric charge and r is the distance between the charged particles. When multiple types of particles are dispersed in a medium, their interaction can be attractive or repulsive depending on the charge. When ions are dissolved in the medium (i.e. salts in aqueous solutions) they can shield the electrostatic potential from the particles.

A charged surface in a liquid is balanced out by oppositely charged counterions, with counterions closely bound to the surface building the *Stern* layer. Originally it was thought the surface and the Stern layer behave like a capacitor, hence the name *double layer*. However, an atmosphere of free ions with rapid thermal motion is formed close to the

surface, called the *diffuse electric double layer*.

The electric *double-layer* interaction potential between two identical spheres with radius R and the closest distance between the particles surfaces D is given by:

$$U_C(D) = \frac{1}{2}ZR e^{-\kappa D} \quad (2.26)$$

with Z being the interaction constant defined by:

$$Z = 64\pi\epsilon_0\epsilon \left(\frac{k_B T}{e} \right)^2 \tanh^2 \frac{ze\phi_0}{4k_B T} \quad (2.27)$$

with the electron charge e , the electrolyte valency z and the surface potential ϕ_0 of the isolated surface (at $D = \infty$). κ^{-1} is the Debye length, which measures how far the electrostatic potential has an effect :

$$\kappa = \sqrt{\sum_i \frac{\rho_{\infty i} e^2 z_i^2}{\epsilon_0 \epsilon k_B T}} \quad (2.28)$$

with $\rho_{\infty i}$ being the ionic concentration in the bulk. The magnitude of the Debye length only depends on the properties of the solution, the surface properties such as charge or surface potential does not effect it.

Steric interactions

When polymer covered particles approach each other, once their polymers start to overlap, they experience a repulsive force due to the entropic unfavored composition when compressing a polymeric chain. This effect is referred to as *steric* or *overlap* repulsion and is used in practical systems to stabilize colloidal particles in conditions where they usually would aggregate.

Total interaction potential of magnetic colloids

In contrast to the DLVO (Derjagi, Landau, Verwey, Overbeek) theory [58], where only attractive van der Waals forces and repulsive double layer forces are included to the total interaction potential, the stability of a magnetic dispersion given by the total interaction potential U_{tot} combines all above mentioned interaction potentials (for U_m see section 2.1.2):

$$U_{tot}(r) = U_A(r) + U_C(r) + U_{steric} + U_m(r) \quad (2.29)$$

By adapting these various interactions, colloids can be tuned to be attractive, repulsive and hard-sphere like.

Hard sphere model

A colloidal dispersion without attractive and repulsive forces behaves hard-sphere like. This means, the limiting packing factor is the geometry of the particles. More precisely, two hard spheres cannot penetrate or deform each other when touching. The pairwise interaction potential for hard spheres with a diameter $2R$ is given by:

$$U_{hs}(\mathbf{r}_1, \mathbf{r}_2) = \begin{cases} 0 & |\mathbf{r}_1 - \mathbf{r}_2| \geq 2R \\ \infty & |\mathbf{r}_1 - \mathbf{r}_2| < 2R \end{cases} \quad (2.30)$$

2.4. DNA and DNA Nanotechnology

2.4.1. DNA

Deoxyribonucleic acid, short DNA, consists of a negatively charged sugar-phosphate backbone (figure 2.7a) and the 4 different bases adenine (A), guanine (G), cytosine (C) and thymine (T) [59]. Pentose sugars (ribose) are connected at their third and fifth C-atom to a phosphate, building the directional backbone, 3' to 5' or vice versa. The first C-atom always holds one of the four nitrogenous bases. These bases can interact pairwise building hydrogen bonds (H-bonds) between each other, called Watson-Crick base pairs (bp), where A-T have 2 H-bonds and C-G have 3 H-bonds (figure 2.7b). Two complementary single DNA strands form a double helix [60], where the directionality of the complementary strand is inverted, the 3'-end of one strand connects to the 5'-end of its complementary strand. Besides the hydrogen bonds, the stacking of base pairs provides additional stability to the double helix due to the overlapping of their π -orbitals. The double helix can come in various forms, but under physiological conditions it takes on the B-form, which has a diameter of 2 nm and makes two full turns every 21 bases. Additionally, the B-form exhibits a minor and a major groove and the average distance between bases is 0.34 nm (figure 2.7c) [61].

What makes DNA the optimal construction material for building nanostructures are the following properties: DNA can be stored for a long period or time [63], it is robust under a wide range of conditions [64], it is easy to handle in water or buffers. Additionally, short synthetic strands are commercially available, it is biocompatible, modular, chemically addressable and can be formed into custom shapes.

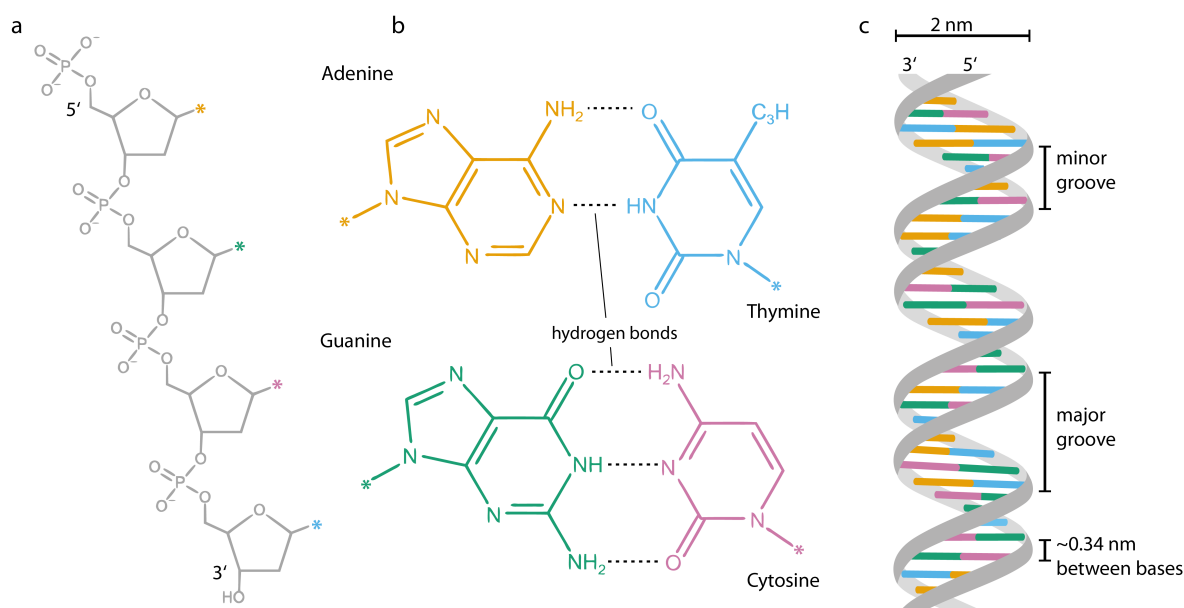


Figure 2.7.: Schematics of **a** sugar-phosphate backbone, **b** complementary base pairing and **c** double stranded DNA in B-form. [62] was used to draw **a** and **b**.

2.4.2. DNA nanotechnology

Ned Seeman, started the field of DNA nanotechnology driven by the vision of creating three dimensional periodic lattices to host and orientate proteins for crystallography. His group started 1991 with a simple DNA cube consisting of six different DNA strands [65] evolved over periodic 2D lattices [66][67] to 3D crystals in 2009 [68].

In 2006, the DNA origami method was introduced by Paul Rothemund [69]. It uses one long (7-9kbp) single DNA strand as a scaffold which folds into the desired shape by the attachment of shorter DNA strands (18-60 bp), so called staples. The scaffold can be harvested from bacteriophages, typically mutations of the M13 bacteriophage, which infects *Escherichia Coli* bacteria. The staples are artificially synthesized and purchasable from specialized companies like IDT [70] or eurofins [71]. As DNA, DNA origami structures are as well fully addressable with nanometer precision.

In the last 20 years, the field of DNA nanotechnology grew extensively and branched out in a lot of areas. Next to exploring the possibilities by creating 2D and 3D megastructures or showcasing the control by creating nanoart, DNA nanostructures are mostly used as a scaffold to create functionality or position functional materials like force spectrometers, plasmonic switches, signal enhancement, photonic band gaps or some kind of motion (figure 2.8).

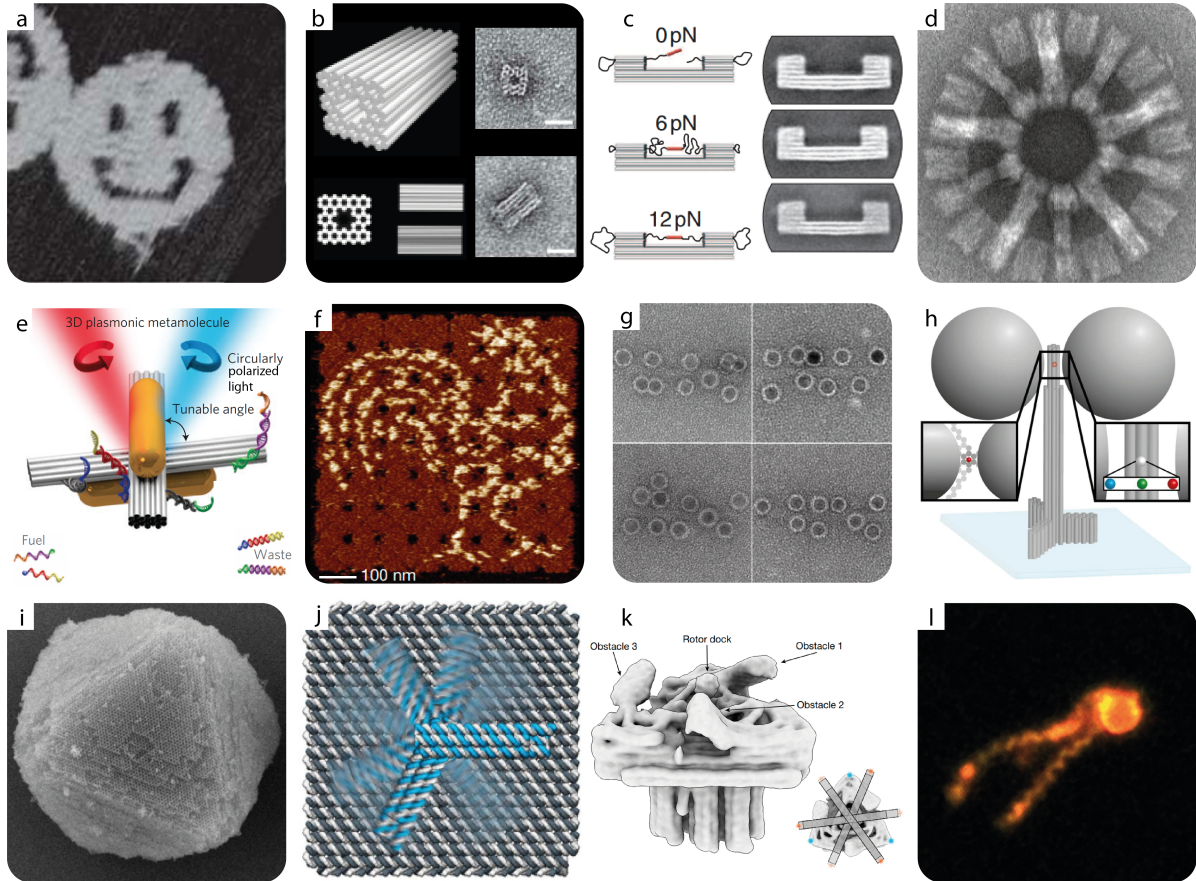


Figure 2.8.: **a** 2D DNA origami [69]. **b** 3D DNA origami [72]. **c** Force clamp, single stranded DNA pulls on molecule of interest by acting like an entropic spring [73]. **d** Gigadalton structure with a radius of 220 nm and a mass of 1.2 GDa [74]. **e** Chiral plasmonic switch via strand displacement [75]. **f** 2D multistructure consisting of individual DNA origami tiles, each having its designated position [76]. **g** Iron oxide nanoparticles attached with spacial control to DNA origami [77]. **h** Plasmonic nanoantenna creating a plasmonic hotspot in-between the silver spheres enhancing a fluorophores signal in its vicinity [78]. **i** Diamond crystal consisting of DNA origami monomers and covered in a silica shell exhibiting a tuneable photonic bandgap in the near UV range [79]. **j** DNA origami arm rotating by applying rotating electric fields [80]. **k** ATPase inspired DNA origami ratchet, driven by electric oscillating fields [81]. **l** Magnetic microswimmer based on DNA tile-tubes attached to a magnetic microbead, actuated by rotating magnetic fields [82]. All images are adapted from their referred original publications.

2.4.3. Nanomachine actuations

Various methods of actuating DNA nanomachines have been established, some depend on fuel (strand displacement), some on buffer conditions like pH (potential of hydrogen), temperature and salt concentration. Other methods are driven externally using light, electric fields or magnetic fields (figure 2.9). In the following, these methods are explained briefly with pointing out the drawbacks of each method, concluding as to why magnetic fields were chosen as the actuation method in this thesis.

Strand displacement: Two complementary strands A, B are bound together, while A is longer than B and has a few free oligonucleotides, the so-called *toehold* sequence. Strand C has the same sequence as B but additionally the complementary sequence to A's toehold. When mixing the compound AB with C, C's complementary toehold sequence first binds to A's toehold and then continues to bind the the rest of the strand while displacing strand B. The result is a compound AC and a free strand B. Strand displacement is a popular technique to create motion on the nanoscale such as steppers [83], switches [75] or rotors [84]. Since the process always needs fuel and anti-fuel strands to drive actuation the practical use for real-world applications is limited.

Changing buffer conditions can also actuate DNA nanostructures. For example on the basis of shape-complementarity and without base pairing, three dimensional reconfigurable DNA nanostructures can be designed to bind in higher salt concentrations or lower temperatures and unbind in lower salt concentrations or higher temperatures [85]. Oscillatory changing of the pH can drive switching of a DNA strand between the random coil and the i-motif formation [86]. Changing buffer conditions requires an external addition of materials limiting the reaction to the mixing time. For potential in-vivo applications, adding material or changing the systems temperature is not suitable.

Light driven actuation is a fast and specific method. Some molecules, such as azobenzene, can change their conformation when irradiated by light. For azobenzene the switch happens from cis to trans state with the irradiation of visible light (450 nm) and back with UV light (350 nm). By incorporating photoswitchable molecules mediating duplexing at the joints of DNA origami structures, it was possible to fabricate photoswitchable DNA origami nanostructures [87][88].

The negative charged backbone of the DNA makes it responsive to *electric fields*. Electrophoretic forces can be used to drive an electric DNA nanorotor as shown in 2009 [89]. In 2018, this simple rotor was evolved by Kopperger et al. to the first electric DNA origami

rotor [80] which was studied in more detail in follow-up publications[90][91][92][93]. Even though the electric actuation works well to study underlying physics of the nanomachine in detail, there are a few drawbacks for potential in-vivo applications, which are the causation of heating problems and all over presence of charges in biological systems, where the impact of electric fields cause unwanted side effects. On top, there is the impossibility of decoupling the DNA origami's morphology from its field response.

An advantage of *magnetic fields* for potential real life applications is that biological systems are inert to magnetic fields. In 2018, the first magnetic DNA origami rotor was created by Lauback et al. [94]. A microscale lever arm attached to a DNA platform fixed to the surface, having a magnetic micro bead attached one end of the arm was rotated by an external in-plane rotating magnetic field. In 2020, Götzfried attempted to downscale that system by attaching magnetic nanoparticles (ferritin) to a the established electric rotor system [95]. However, despite applying significant fields and field gradients, no actuation was observed. This is likely due to the small (< 10 nm) magnetic core of the ferritins, making them not strongly magnetic and the large distance between the particles preventing significant magnetic coupling that could enhance their overall magnetic response. Furthermore, their spherical curvature is not optimal for coupling between two adjacent particles.

In February 2024, a magnetic nanorotor was realized [96]. It consist of a 60 nm gold particle with ferromagnetic core and a 200 nm porous gold cage attached to a supported lipid bilayer platform. A magnetic rotating field constantly rotates the magnetic particle. The magnetic particle can be coupled to the cage using strand displacement, like a clutch in a car. The rotation of the cage is visualized by optical reporters at the end of an 550 nm long DNA rotor blade attached to the cage.

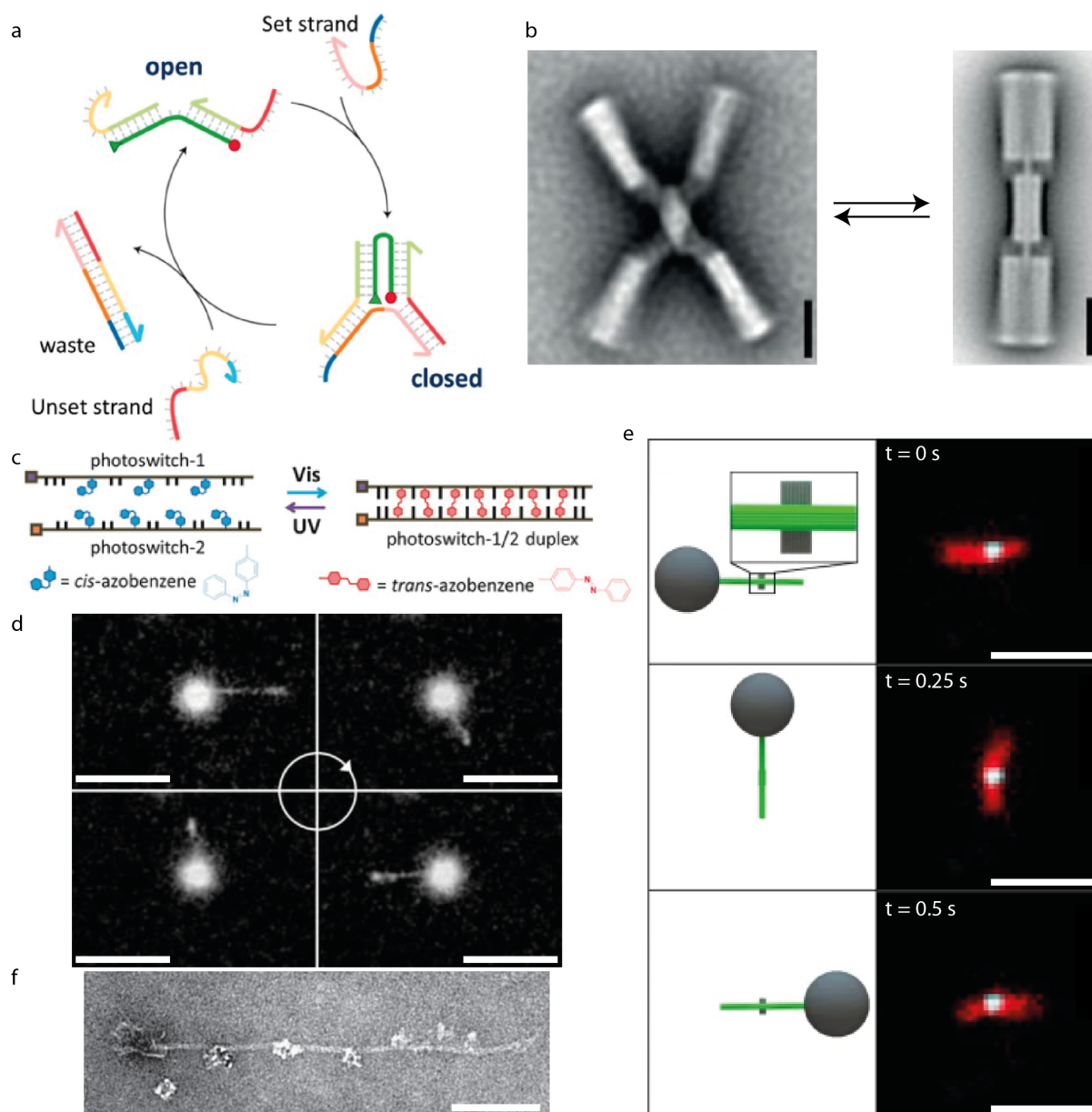


Figure 2.9.: **a** Schematic opening and closing cycle of a DNA switch via strand displacement [97]. **b** TEM micrographs of opened/closed cross in the presence of 5 mM/25 mM MgCl_2 [85]. Scale bars: 20 nm. **c** Schematic of UV-Vis photoswitch mediated duplexing [88]. **d** Fluorescence microscopy images of a rotational DNA nanomotor [89]. Scale bars, 10 μm . **e** DNA origami microrotor actuated by rotational magnetic fields [94]. Scale bars, 1 μm . **f** 5 ferritins attached to a DNA origami pointer structure, to create a magnetic DNA origami nanorotor [95]. Scale bar, 100 nm. All images are adapted from their referred original publications.

3. Experimental methods

In this chapter, the experimental methods used to fabricate, purify and measure the behavior of magnetic structures in response to dynamic and static magnetic fields are detailed: A superparamagnetic colloidal particle dispersion is used to cast magnetic modules which assemble into magnetic microswimmers. Moving down in scale, DNA origami is used as flagella, attached to a magnetic micro bead and as a template to attach magnetic nanoparticles (mNPs) and metallic (gold and silver) nanoparticles. DNA origami is purified by PEG (polyethylene glycol) precipitation and DNA origami nanoparticle hybrids are purified using gel electrophoresis. The nanostructures are visualized using transmission electron microscopy (TEM). For all these experiments, static and dynamic magnetic fields are applied using electromagnetic coils and permanent magnets to the magnetic micro- and nanostructures. The swimmer experiments are taken close to a surface, while the nanorotors are one-sidedly mounted to a PEG-modified surface. The experiments are monitored using microscopy techniques (brightfield microscopy for microstructures and total internal fluorescence microscopy (TIRFM) for nanostructures). Darkfield microscopy was used to observe noble nanoparticles on a DNA origami attached to a surface in a hexagonal pattern. Protocols to all methods, if not stated otherwise, can be found in the appendix.

3.1. Shape-casting with superparamagnetic dispersion

Superparamagnetic nanoparticles were purchased from GE Healthcare, now available from Cytiva [98]. The particle's diameter is around 400 nm and they consist of 2-3 nm superparamagnetic iron oxide particles packed within a silica shell. For the purpose of making magnetic modules, the particles are dispersed in a organic monomer called ETPTA (Ethoxylated trimethylolpropane triacrylate), therefore no double layer interactions. Despite the lack of charge stability, refractive index matching of silica and ETPTA minimizes van der Waals interactions and grafting the molecule 3-((Trimethoxysilyl)propylmethacrylate) to the particles surfaces produces a stable particle dispersion. Without attractive van der Waals and repulsive double layer forces, and no external magnetic

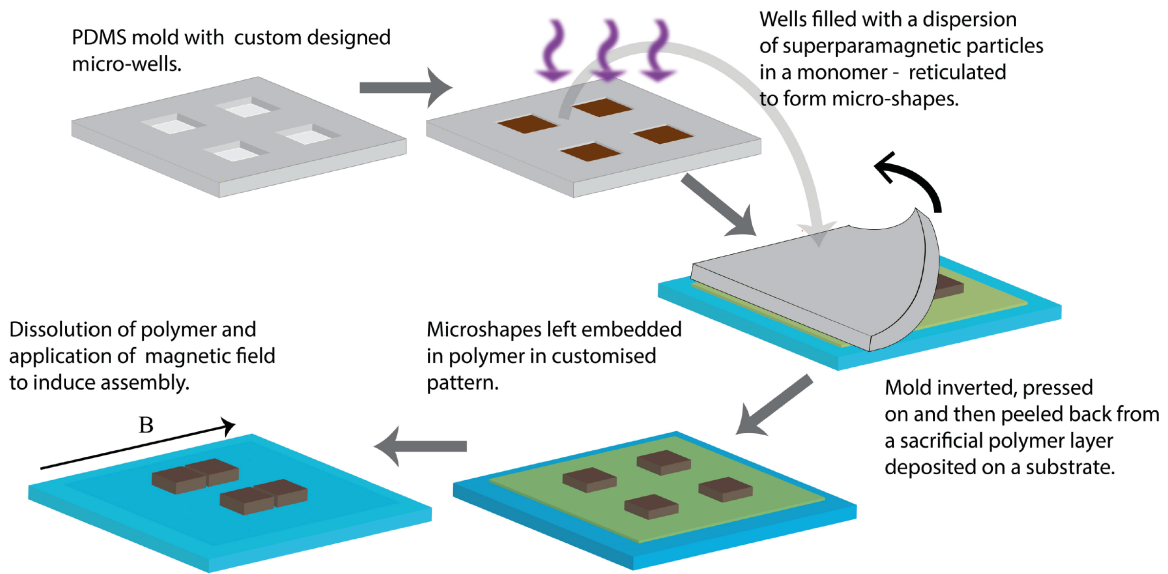


Figure 3.1.: Workflow of magnetic shape-casting using a superparamagnetic dispersion. When exposing the dispersion to UV light, the polymer ETPTA crosslinks, creating a solid module. When these modules are extracted from the PDMS mold and the extraction polymer is dissolved, a magnetic field can be used to assemble the modules into a designed configuration. Image adapted from [99].

field applied, the dispersion can be described with the hard-sphere model. By adding a photoinitiator (2-Hydroxy-2-methylpropiophenone) to the dispersion, the monomer can be crosslinked by exposing the dispersion to UV-light (254 nm). Various shapes in the order of several micrometers can be created by casting the magnetic dispersion into custom designed PDMS (Polydimethylsiloxane) molds. After reticulation via UV light irradiation, the magnetic shapes can be extracted via a sacrificial polymer which itself gets dissolved after a magnetic field was applied to assemble the shapes into compound structures (figure 3.1). The magnetic modules themselves again inherit the superparamagnetic properties of the smaller particles they consist of.

3.2. Folding DNA Origami

DNA origami consists of a scaffold, which is a long, typically circular, single DNA strand and staples, which are shorter oligonucleotides, with a length between 11-60 bp. They are mixed together with an excess of staples in a relation of 1:5 or 1:10 depending on the structure. Since DNA is negatively charged, folding a closely packed structure out of it requires shielding of the charges of the individual strands, using Na^+ and Mg^{2+} ions. The

buffer TAE (Tris(hydroxymethyl)aminomethane, Acetic Acid, Ethylenediaminetetraacetic acid (EDTA)) keeps the pH value stable within a range where DNA is stable (around pH=8). The scaffold, staples, salt and buffer mixture is heated up to 65°C to break up all secondary structures and then slowly annealed to 25°C to avoid entropic traps. The folded DNA origami is purified from excess staples and then can be used afterwards for further experiments [100].

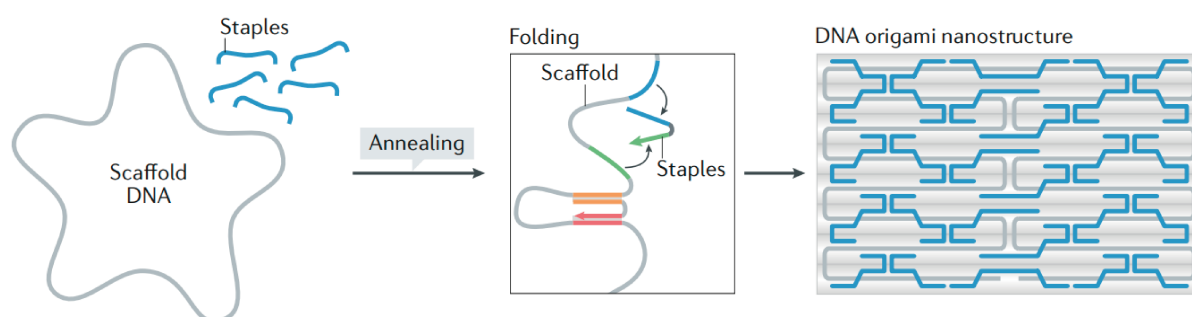


Figure 3.2.: Scheme of DNA origami folding process. Image adapted from [100].

3.3. Functionalization of nanoparticles

To bind nanoparticles to DNA origami structures, DNA strands have to be attached the particle's surface. The functionalized particle can bind to a complementary sequence from a DNA origami extension via hybridization.

To functionalize magnetic nanoparticles (here: cobalt doped iron nanoparticles), they are covered with a PMAO-PEG-amide polymer (PMAO: poly (maleic anhydride-alt-1-octadecene)) and then DBCO (Dibenzocyclooctin) modified single stranded DNA is attached via click-chemistry between the amide and the DBCO group (figure 3.3a) [3]. TEM images of the polymer coated and the DNA functionalized magnetic particles are shown in figure 3.3b and c and the particles' hysteresis curve is shown in figure 3.3d. These experiments were performed by our collaborating group of Dr. Lak in Braunschweig.

Thiol-groups can bind to gold surfaces because of the strong affinity of sulfur to noble metals (figure 3.4) [101]. This effect is used to functionalize surfaces of gold or silver nanoparticles with thiol modified single stranded DNA.

3.4. Purification

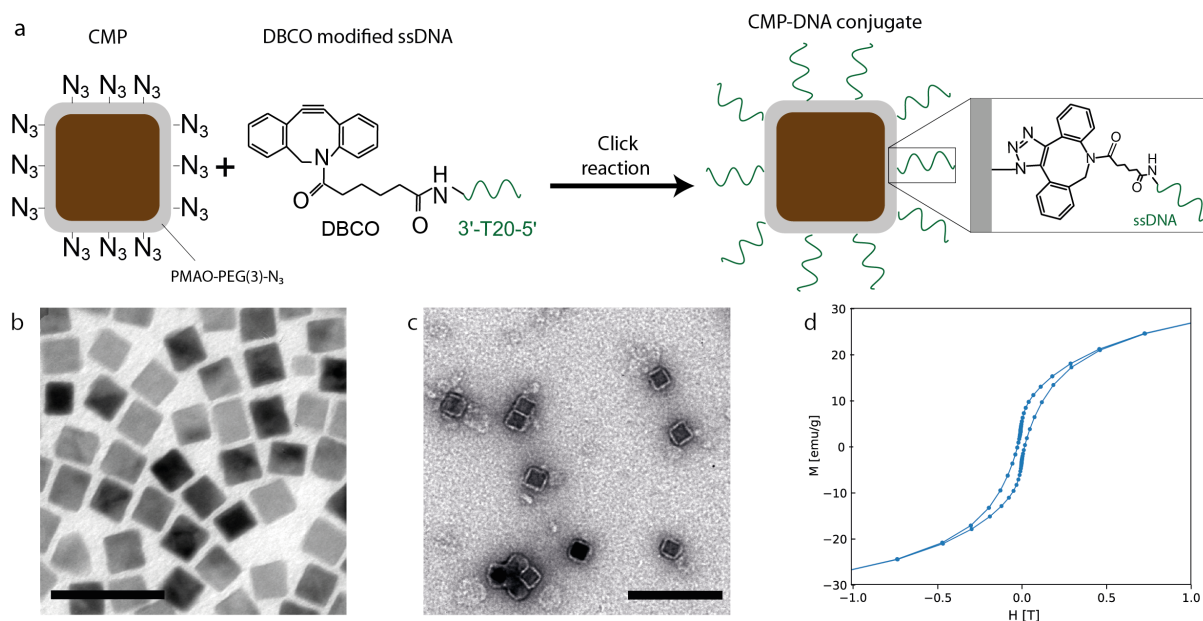


Figure 3.3.: a Schematic of the DNA functionalization of azide labeled magnetic nanoparticles via a click reaction between the azide-labeled CMPs and dibenzocyclooctyne (DBCO)-modified DNA strands. TEM images of b polymer coated mNPs and c DNA functionalized mNPs, scale bars are 50 nm and 100 nm, respectively. d Magnetization curve of CMPs dried mNPs. Images adapted from [3].

3.4. Purification

In order to reliably use DNA origami, DNA functionalized nanoparticles or hybrid structure containing both in experiments, they need to be purified from excess DNA strands and aggregations. Widely used techniques in biochemistry and molecular biology can also be employed to for the purification of DNA origami. The different purification methods were compared by Wagenbauer et al. in 2017 [103]. The main methods used in this thesis were agarose gel electrophoresis and PEG precipitation.

Gel electrophoresis is a simple but effective purification technique, where a voltage is

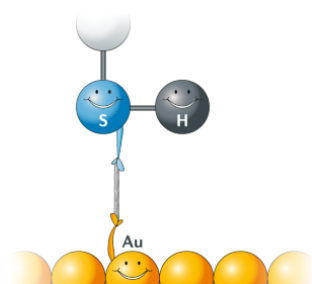


Figure 3.4.: Schematic gold (Au) sulfur (S) bond. Image adapted from [102].

applied to an agarose gel surrounded by buffer. Typically the negative pole is on the top of the gel, resulting in a flow of negative charged entities from top to bottom. With the gels mesh like structure, it acts as a sieve to separate the sample by size and shape. The concentration of the agarose percentage defines the density of the mesh, with higher densities for increasing concentrations. In summary, depending on their size, shape and charge, samples run at different speeds through the gel.

After the purification, the different fractions appear as separate bands in the gel (DNA needs to be stained (SybrSafe) for visualization). The desired bands are cut out of the gel and squeezed to extract liquid aliquots from the agarose gel.

Because of the visual feedback of the bands, gGel electrophoresis can also be used as characterization technique to identify the success of a binding experiment [100]. The drawback of the method is its low yields of 5%-10%.

In 2014, Stahl et al. characterized in detail the method of PEG precipitation to purify DNA origami [104]. The method is easy to operate, scalable and has high yields over 80%. Centrifugation of a mixture of PEG buffer and folded DNA origami at low temperature (4°C) results in a pellet containing DNA origami at the bottom of the tube and the excess staples remain in the supernatant. Removing the supernatant and resolving the pellet leads to a purified and concentrated DNA origami solution. This method was used to purify larger volumes of simple DNA origami structures.

3.5. PEG surface modification

Glass slide were treated with silane-PEG-biotin (SPB), which is a linear heterobifunctional PEG reagent with biotin and silane. The glass surface is modified via the reaction between the surfaces hydroxyl groups and the ethoxyl/methoxyl silane groups of the SPB [105]. The different parts of the SPB provide different functionality: The PEG passivates the surface and minimizes unspecific binding. The biotin enables specific binding of streptavidin or neutravidin. A nanostructure containing streptavidin or neutravidin can then bind to the surface via biotin-streptavidin interactions.

3.6. Visualization methods

3.6.1. Brightfield microscopy

In brightfield microscopy, light shines through the sample (figure 3.6a). A mixture of transmitted light and scattered light is detected. The background is bright and contrast

comes from absorption and scattering. The smallest distance d of two points, at which they can still be separated, is given by the Abbe limit:

$$d = \frac{\lambda}{2NA} \quad (3.1)$$

where λ is the wavelength of emitted light of the sample and $NA = n \sin(\theta)$ is the numerical aperture depending on the refractive index n of the medium between the lens and the objective and θ is half the angle of the light cone entering the objective.

3.6.2. DFM - Darkfield Microscopy

In top illumination darkfield microscopy, the light shines from the top with an angle on the sample, so that the transmitting light bypasses the objective. Only the scattered light from the sample is collected [106], resulting in a typical darkfield image: bright spots on black/dark background. With darkfield microscopy it is also possible to image nanoparticles with sizes below the diffraction limit. A polarizer can be used to observe polarized light effects that are obtained by anisotropic nanoparticles (figure 3.6b) .

3.6.3. TIRFM - Total Internal Reflection Fluorescence Microscopy

Electrons of fluorescent dyes can absorb photons to bring them in a higher energy state (3.5a) [107]. This unstable high energy state loses excessive energy via vibrations and radiation of photons. The emitted photons have a lower energy than the initially absorb photons, where the difference in wavelength is called Stokes-shift (3.5b). In a fluorescent microscope, the emitted light from the fluorescent dye is detected, while potentially reflected light from the source is filtered out via a band-width filter.

Total internal reflection fluorescence microscopy (TIRFM) improves the signal to noise ratio even more than traditional fluorescence microscopy with basically zero background since only fluorophores close to the interface are excited via an evanescent wave.

When light hits the interface of two media with different refractive indices, the light gets refracted following Snell's law with an incident angle α_{in} and an outgoing angle α_{out} [109]:

$$n_1 \cdot \sin \alpha_{in} = n_2 \cdot \sin \alpha_{out} \quad (3.2)$$

When light travels from a medium with higher refractive index to one with lower refractive index, in cases of high incident angles, it would be $\sin \alpha_{out} > 1$, which is impossible in the real space. The physical observation of this phenomena is that the light gets completely reflected, called *total internal reflection*. For the water - air interface ($n_w = 1.333$, $n_a = 1$),

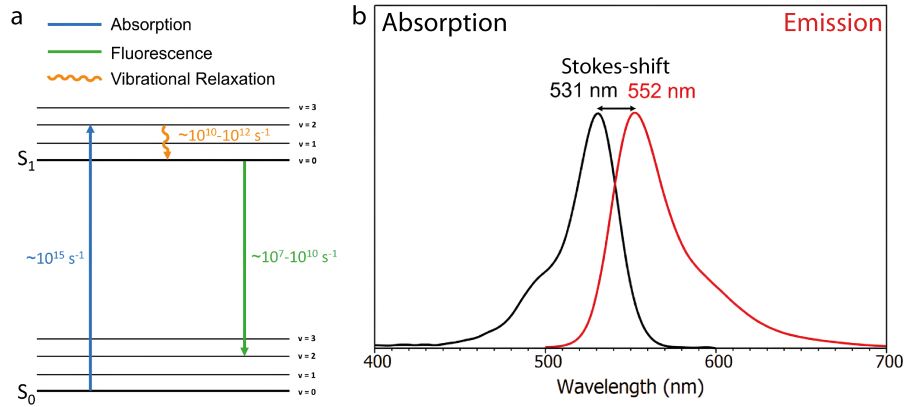


Figure 3.5.: **a** Jablonski diagram for energy states of electrons in a fluorescent dye. **b** Stokes shift, peak emitted wavelength is longer than peak absorbed wavelength. Images adapted from [108].

this effect occurs for incident angles higher than $\alpha_{crit} = 48.6^\circ$. On the interface where the total reflection occurs, an evanescence wave emerges perpendicular to the interface. This evanescence wave excites the fluorescence dyes in the sample. The fluorescent signal is then detected by a camera. Since the evanescence wave decays exponentially, only the dyes close to the interface get excited, which is the reason why the signal to noise ratio is excellent (figure 3.6c).

3.6.4. Resolution of DFM and TIRFM

The microscopy techniques DFM and TIRFM are based on light-emitting specimen, in the darkfields case it sample scatters light in specific wavelengths and in the TIRFM case, the samples fluorescent dye radiates at specific wavelengths. Images of self-luminous points are not points but rather diffraction patterns which can be describe by a point-spread function. The closest distance of two point-spread functions, where they can be still separated, is when the maximum of one point-spread function falls into the first minimum of another. This is called the Rayleigh criteria. The resolution of a microscope with self-luminous specimen is defined by [110]:

$$d = \frac{0.61 \cdot \lambda}{NA} \quad (3.3)$$

With a numerical aperture of $NA = 1.3$, the spacial resolution for $\lambda = 546 \text{ nm}$ is $d = 256 \text{ nm}$ and corresponds to the measured particles radius. This means, it is not possible to separate the signals of two points with a distance smaller than 200 nm at the same

time. Therefore a typical DNA origami with a long axis of 50-500 nm cannot be resolved by visible light without using superresolution techniques.

3.6.5. TEM - Transmission Electron Microscopy

To overcome the resolution limit of light based microscopy techniques, one approach is to use particles with shorter wavelengths than optical photons, i.e. electrons. The wavelength of an electron is dependent on its kinetic energy $E_{kin} = e \cdot V_a$. For biological experiments, the acceleration voltage is $V_a = 80$ kV. At high kinetic energies, the electrons approach the speed of light, so the basic de Broglie equation $\lambda_{dB} = hc/E$ to calculate the wavelength of an electron has to be corrected for relativistic effects [111]:

$$\lambda_{dB} = \frac{h}{\sqrt{2m_e e V_a \left(1 + \frac{e V_a}{2m_e c^2}\right)}} = 4.18 \text{ pm} \quad (3.4)$$

with the mass of an electron $m_e = 9.109 \cdot 10^{-31}$ kg, the electron charge $e = 1.602 \cdot 10^{-19}$ C, the Planck constant $h = 6.626 \cdot 10^{-34}$ m²kg/s and the speed of light $c = 2.998 \cdot 10^8$ m/s. The resolution could even be increased increasing the acceleration voltage (typical 100-300 kV), resulting in $\lambda_{dB} = 1.96$ pm. However, biological samples would get destroyed by these high kinetic energies.

The electron source of a TEM is a tungsten filament, which when heated, radiates electrons to its environment. These free electrons get accelerated through the anode and then focused by magnetic lenses on the sample. The transmitted electrons are then detected by either a fluorescent screen or a camera (figure 3.6d). The contrast of the resulting image depends on the absorption or the scattering of electrons from the sample. Since biological samples are almost transparent to electrons, the contrast of them would be quite poor. In order to improve the contrast, biological samples are stained with heavy elements, e.g. uranium contained in the molecule uranylformate.

3.7. Magnetic setups

For the magnetic microswimmer experiment, a quadrupole was setup by arranging two electromagnetic coils and two permanent magnets opposite of each other on a stage of an optical microscope around the center. With this setup a homogeneous field $B_x = B_0$ produced by the permanent magnets was combined with the oscillating field of the coils $B_y = B_0 \cos(\omega t)$ to create a wagging magnetic field $\mathbf{B} = B_x \hat{\mathbf{x}} + B_y \hat{\mathbf{y}}$, using the unit vectors

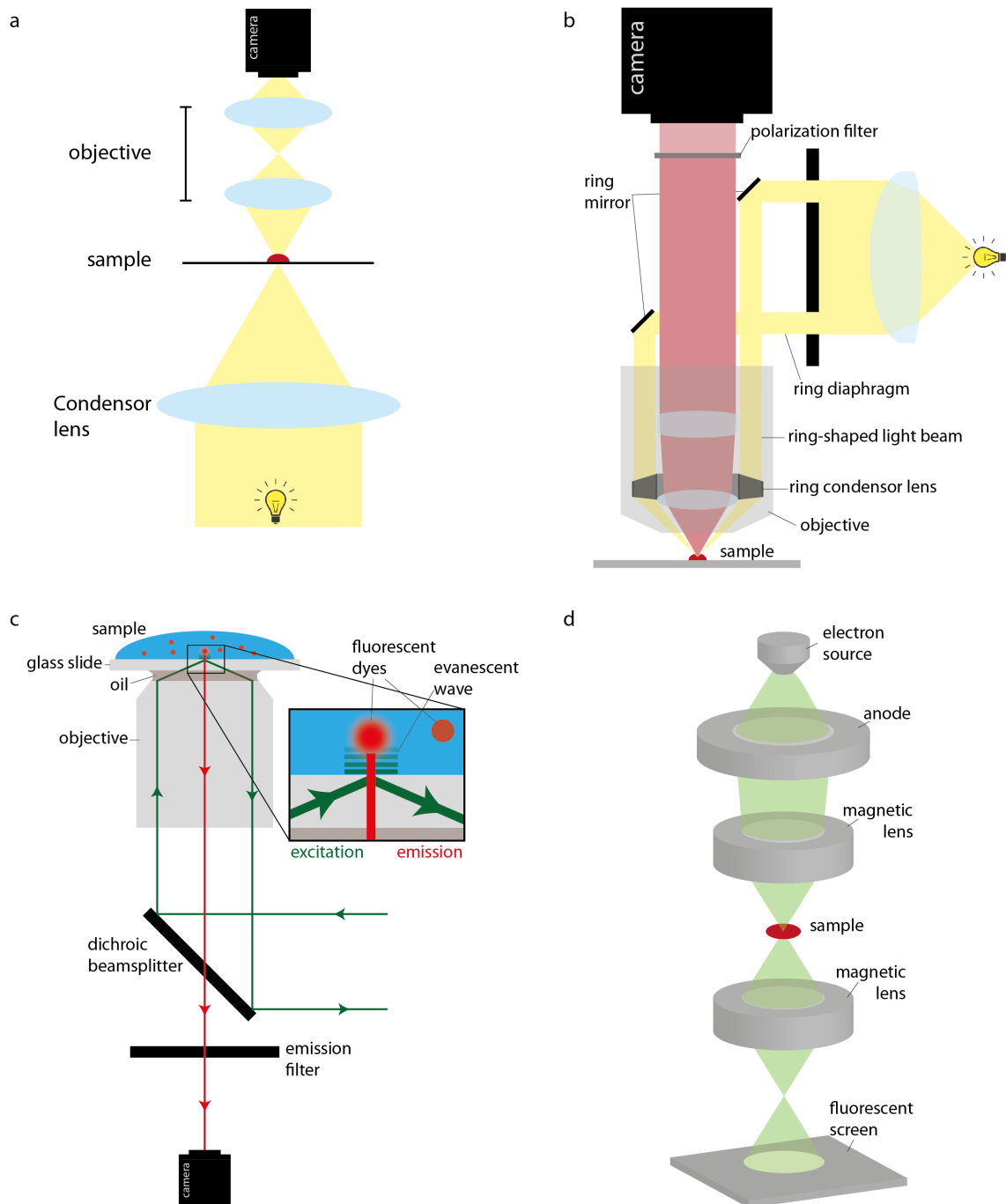


Figure 3.6.: Schematics of **a** brightfield microscopy, **b** darkfield microscopy, **c** TIRFM and **d** TEM. Images inspired by **a** [112], **b** [113], **c** [114], **d** [115].

$\hat{\mathbf{x}} = (1, 0)$, $\hat{\mathbf{y}} = (0, 1)$, which was used to actuate the microswimmers in publication P1 and P2.

For the magnetic nanorotors, a quadrupole was setup by placing four electromagnetic coils around the center of a stage, which was designed and fabricated in house, mounted to a TIRFM. With this setup, rotating ($\mathbf{B} = B_0 \sin(\omega t)\hat{\mathbf{x}} + B_0 \cos(\omega t)\hat{\mathbf{y}}$) and homogeneous ($\mathbf{B} = B_0\hat{\mathbf{y}}$) magnetic fields were applied for actuating the nanorotors.

In the following chapters 4-7, the main results of this thesis, produced by using above experimental methods, are presented, starting with publication P1, Programmable Design and Performance of Modular Magnetic Microswimmers.

4. P1: Programmable Design and Performance of Modular Magnetic Microswimmers

Creating microswimmers of the flexible oar type poses a considerable challenge. This is because engineering at the microscale involves non-trivial tasks, such as connecting tiny components to achieve precise movements. The ability to fabricate artificial microswimmers at scales below $100\ \mu\text{m}$ rapidly, reliably, and with adaptable designs is crucial but complex. General approaches to achieve magnetic and flexible microstructures that swim are self-assembly [49] and top down lithography [116]. The former provides ease and scale of assembly at the expense of tight architectural control whereas the latter provides exact architectural control but requires expensive and laborious fabrication protocols.

The following paper presents a technique that provides the production at scale of self-assembly with the precision of top-down techniques in this area. It builds on publications by Tavaoli et al. [23][99]. Here, a method to develop micron-sized non-spherical particles with virtually any 2D cross section was developed. The process is based on the filling of a PDMS mold that holds micron-sized wells of any cross section and any position down to 2 microns with a magnetic precursor dispersion that, once in the wells, is reticulated into solid magnetic microshapes (see section 3.1). Significantly the shapes are harvested from the mold by *waxing* them out with a sticky polymer that leaves their shape and relative position in tact. The initial use of the magnetic shapes was to compress the protein actin in a controlled manner under magnetic fields to extract its nonlinear mechanics [117]. It was then realized that this technique can be exploited to assemble complex actuating structures by adapting the position, the shape and the orientation of the PDMS wells. It was further recognized that this approach was highly suited to make magnetic micro swimmers, because it enables the magnetic assembly of jointed linear structures at the microscale, in other words: the design criteria for microswimmers.

For this process to be successful, the modules are preoriented, so when then a field is applied, their easy axis, which for a collection of superparamagnetic particles aligns with

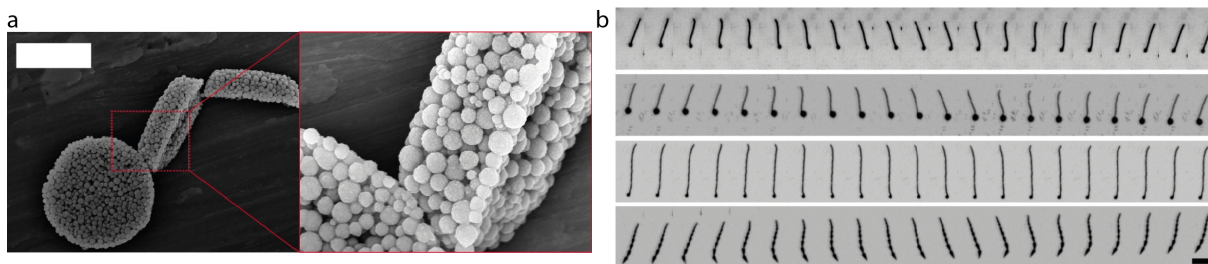


Figure 4.1.: **a** Scanning electron microscopy (SEM) images of magnetic modular microswimmer, head unit and two modules and close-up on connection between head unit and first module. scale bar: $20 \mu\text{m}$. **b** Full strokes of the S (i.), BH (ii.), LT (iii.) and Tr (iv.) swimmers at 19 Hz. Full actuation of the S, BH and Tr swimmers is evident while the LT swimmer performs only end wagging. The strokes were imaged by capturing a 19 Hz beating pattern at 20 fps stroke to produce aliasing. The aliasing produces the optical illusion of swimming in reverse in these captions. Scale bar is 50 microns. Images adapted from [1]

the long axis, wants to align with the applied field and thereby the modules rotate. After rotating, if the modules are distanced close enough together, magnetic dipole interactions lead to the formation of the designed swimmer. The flexibility of the swimmer originates from the weak dipole-dipole interactions and the small connection area between the modules (see figure 4.1a). The swimmers response can be categorized into three types. *i* At low frequencies magnetic forces dominate resulting in an oscillating stiff rod. With minimal flex, the movement pattern is almost reciprocal and therefore low swimming efficiency and velocity. *ii* At intermediate frequencies, the magnetic and the viscous forces are balanced, resulting in flex of the swimmer enabling propagating of a bending wave through the tail leading to high swimming velocities. *iii* At high frequencies the viscous forces dominate. Only the ends of the swimmer are able to follow the magnetic field while the rest of its body behaves like a stiff rod, resulting in low velocity swimming.

The degree of bending in the swimmer defines the direction of swimming, being the direction of the end exhibiting the largest bend. Moreover, qualitatively it can be seen that the relative proportions of flex at each end of the swimmer is related to the swimmer's velocity. It could be observed, that the triangle swimmer is the only swimmer of the four fabricated types which swims head first (figure 4.1b). Out of the four, the triangle swimmer shows the fastest velocities peaking at around $25 \mu\text{m/s}$ at an applied frequency of 20 Hz. The velocity-frequency data can be collapsed into a reduced velocity dependent on the square root of the Mason number, indicating that these swimmers are purely determined by magnetic and viscous forces, elastic forces are neglectable. Based on the results for the four swimmers, a fast swimmer was designed being able to exhibit bend at

higher frequencies and therefore reach higher velocities.

The experiments setup also allows for the observation of multiple swimmers at the same time, which can be used to study collective behavior. Four main interactions have been observed: The head-to-tail aggregation, the head of one swimmer connects to the tail of swimmer in front of it, combining into one long swimmer. Overtaking, one swimmer overtakes another. Side-by-side, two swimmers swim synchronously next to each other. Snap aggregation, two swimmers next to each other connect sideways into one 'wider' swimmer.

Note, due to problems with suppliers, the initial method [23] was adapted for a new set of *superparamagnetic* particles. However, subsequent experimentation revealed a very small permanent magnetic moment [5].

In the future, the soft lithographic approach used in this publication could be used to design and produce more variations of microrobots, not only swimmers. Exploring the design space of such systems could help solving engineering problems on the microscale and to make 2D and even 3D microstructures.

Programmable Design and Performance of Modular Magnetic Microswimmers

Christoph Pauer, Olivia du Roure, Julien Heuvingh, Tim Liedl, and Joe Tavacoli*

Synthetic biomimetic microswimmers are promising agents for in vivo healthcare and important frameworks to advance the understanding of locomotion strategies and collective motion at the microscopic scale. Nevertheless, constructing these devices with design flexibility and in large numbers remains a challenge. Here, a step toward meeting this challenge is taken by assembling such swimmers via the programmed shape and arrangement of superparamagnetic micromodules. The method's capacity for design flexibility is demonstrated through the assembly of a variety of swimmer architectures. On their actuation, strokes characterized by a balance of viscous and magnetic forces are found in all cases, but swimmers formed from a series of size-graded triangular modules swim quicker than more traditional designs comprising a circular "head" and a slender tail. Linking performance to design, rules are extracted informing the construction of a second-generation swimmer with a short tail and an elongated head optimized for speed. Its fast locomotion is attributed to a stroke that better breaks beating symmetry and an ability to beat fully with flex at high frequencies. Finally, production at scale is demonstrated through the assembly and swimming of a flock of the triangle-based architectures to reveal four types of swimmer couplings.

As set out in groundbreaking work by Purcell, locomotion at microscopic length-scales rests on a swimming stroke that is non-time symmetric.^[1] Purcell proposed a minimal example; a three-rod system that generates propulsion through alternative rotation of its front and back appendages. Informed by Purcell and Nature itself, a number of artificial microswimmers have emerged over the last 20 years and are promising agents

for targeted in vivo healthcare as well as important frameworks from which to advance the understanding of locomotion strategies at the microscopic scale.^[2–20] The swimming strategies employed by eukaryotic and prokaryotic cells that generate thrust by the sinusoidal-like beating and the corkscrew rotation of flagellum, respectively, have been of particular inspiration to man-made designs.^[4,7,13,21–23] To mimic the former, and facilitate a non-time-symmetric swimming stroke, artificial microswimmers require jointed and/or inherently flexible frameworks that are typically actuated using external stimuli, for example, magnetic/electric fields, monochromatic light, or acoustic waves.^[2,8,9,11,22,24] A seminal synthetic biomimetic microswimmer is a magnetoelastic one realized by Dreyfus et al., comprising a filament of monodisperse micrometer-sized superparamagnetic beads connected together with DNA chains and tethered to a red blood cell.^[22,25] Via coupling to a sinusoidal mag-

netic field, this swimmer moves through a paddle-like beating of its flexible tail that initiates wave propagation predominately from its free to tethered end. Typically, the stroke of such swimmers and other magnetoelastic filaments depends on a balance of viscous, magnetic, and elastic forces. In cases where elastic forces are negligible, the balance requires only the former two forces, as quantified using the Mason number^[26]


$$M_a = \zeta_{\perp} \mu_0 \omega L^2 / (a B \chi)^2 \quad (1)$$

Here, ζ_{\perp} , μ_0 , ω , L are the perpendicular viscous coefficient, permeability of free space, angular frequency, and filament length, respectively, a is bead radius, B is magnetic field strength, and χ is magnetic volume susceptibility. M_a can be related to a magnetoviscous length scale, l_m , as $M_a^{1/2} \approx L/l_m$, where the size of l_m with respect to L dictates the nature of the stroke in response to the time-varied magnetic field. Specifically, the cases $l_m \gg L$ (magnetic forces \gg viscous forces) and $l_m \ll L$ (viscous forces \gg magnetic forces) are associated with rigid-rod motion and tip wagging of magnetoelastic filaments, respectively, while at $l_m \approx L$ (viscous forces \approx magnetic forces) their full rotation with flex is predicted.^[25–27]

While many derivatives of this type of flexible biomimetic magnetic swimmer now exist, constructing them to specification and in large numbers remains a challenge, limiting their advancement toward application.^[2,9,21–29] Indeed, from an

C. Pauer, Prof. T. Liedl, Dr. J. Tavacoli
Faculty of Physics and Center for NanoScience
Ludwig-Maximilians-Universität
Geschwister-Scholl-Platz 1, München 80539, Germany
E-mail: j.tavacoli@lmu.de

Dr. O. du Roure, Dr. J. Heuvingh
Physique et Mécanique des Milieux Hétérogènes CNRS
ESPCI Paris
Université PSL
Sorbonne Université
Université de Paris
Paris F-75005, France

 The ORCID identification number(s) for the author(s) of this article can be found under <https://doi.org/10.1002/adma.202006237>.

© 2021 The Authors. Advanced Materials published by Wiley-VCH GmbH. This is an open access article under the terms of the Creative Commons Attribution License, which permits use, distribution and reproduction in any medium, provided the original work is properly cited.

DOI: 10.1002/adma.202006237

application perspective other types of synthetic micromotors have proved more fruitful such as rigid micromotors driven by surface-mediated chemical reactions and/or magnetic fields and biohybrid designs that combine a man-made element with a natural microswimmer.^[16–18,28,30–35] Of the former class, rigid magnetically controllable biocompatible microcylinders propelled via reaction with gastric acid with drug release capabilities have been engineered as have magnetic rotators demonstrating long-distance intravitreal propulsion within porcine eyes.^[18,31,34] Of the latter class, sperm cells coupled with magnetic elements have been constructed to allow their remote control and the targeted delivery of drugs or genetic material and, in general, the biohybrid approach is a promising one toward autonomous theranostics, microsurgery, and gene transfection.^[16,17,28,33]

Despite the relative lack of application progress, fully synthetic flexible microswimmers are in principal well suited for application as their fully engineered nature permits great scope to tune their performance for task. Those driven by magnetic fields are further suited for purpose because of the inherently bio compatible nature of the driving field and its capacity to be facily tailored at low cost.^[29,36] A particular bottleneck that effects these types of microswimmers, that more broadly impacts microrobotics, arises from the non-triviality in engineering and then connecting microscale parts into configurations that yield precise actuations and the capacity to fabricate artificial microswimmers, and other microactuators, on the sub 100- μm scale rapidly, robustly, and with design flexibility will greatly accelerate their progression to application and broaden their scope on arrival.^[15,37]

Herein, we outline a pathway to achieve these requirements using a new methodology to assemble modular, jointed magnetic microswimmers of pre-programmable design. The modular units, which can have lengths as small as 2 μm , self-assemble into microswimmers upon application of a homogenous magnetic field. By engineering these swimmers from discrete modules, we endow them with a flexibility essential for their swimming at the low Reynolds number limit.^[1,11] Such flexibility is absent within single modules even at high aspect ratios prohibiting the fabrication of a swimmer from a single piece. To program swimmer architecture we use two handles: the shape of the modules and their spatial arrangement prior to assembly. The combination of these two variables with the applied field produces a magnetic landscape that rotates (magnetic torque) and/or translates (magnetic dipole-dipole attraction/repulsions) the modules, thus assembling them into a structure of choice. The shape and angle dependency of magnetic torques and dipole-dipole interactions allow, in principle, the kinematic responses of our magnetic modules to be ab initio predicted.

We demonstrate the capacity for design flexibility by forming five distinct swimmers and reviewing their locomotion in the context of their form. This coupling brings understanding of the underlying physics and we extract design rules to optimize for swimming speed. Our parallel fabrication procedure allows us to study interactions between multiple beating synthetic biomimetic swimmers and we highlight four different types of couplings between our swimmers.

Control of the shape of our magnetic modules and their starting position is granted via a reported lithographical

protocol to fabricate non-spherical superparamagnetic particles and our fabrication and assembly approach is outlined in **Figure 1a**.^[38–41] The as produced particles—our modules—are composites of a densely and uniformly packed superparamagnetic colloid encased in a crosslinked network of the monomer ethoxylated trimethylolpropane triacrylate (ETPTA). All materials used have shown biocompatibility in ex vivo studies (Section S1, Supporting Information).^[41] Significantly, the homogenous packing of the magnetic colloid within the modules allows their magnetic easy axis to be geometrically defined, yielding a shape-determined response to a magnetic field.^[38–40] In house measurements estimate the unitless magnetic volume susceptibility of our modules to be ≈ 1 , that is, similar to commercial magnetic beads used for biological purifications (Section S2, Supporting Information).

To highlight the design flexibility of our method we start by assembling four populations of distinct swimmer architectures: standard (S), long tail (LT), big head (BH), and triangle (Tr) (Figure 1b). The former three architectures (S, LT, and BH) are the same class of design, being head-tail (HT) swimmers composed of a circular prism “head” connected to a series of smaller ellipsoidal-prism “tail” units (long axis = 8 μm , short axis = 2 μm). These HT swimmers differ only through variation of head size (diameter = 8 μm (S, LT) or 16 μm (BH)) and number of tail units (10 (S, BH) or 20 (LT)). To facilitate the assembly of the HT architectures, the modules are linearly arranged with the major axis of individual tail modules offset 90° along the pattern. On application of a homogeneous magnetic field along the pattern’s major axis (the y -axis), the tail modules rotate, connecting tip-to-tip to form a tail that attaches on one end to the head module (Figure 1c, top). The Tr swimmer, to our knowledge a unique design, has a starting modular pattern of ten isosceles triangles, linearly arranged but with their major axes offset alternately at -80° and $+80^\circ$. The leading two triangles have a long and short side of 20 and 8 μm respectively, thereafter the modules become systematically smaller by a factor $1-0.1n$ for each n th proceeding triangle ($n = 1-8$). The angular arrangement of the triangles induces their alternate counter clockwise/clockwise rotation which, in combination with their linear pattern, guides base-to-tip connections after their full rotation along the y -directed field (Figure 1c, bottom). We emphasize that in both classes of swimmer design, rotation of the tail modules is a necessary assembly feature permitting the vast majority of swimmers to assemble to order (see Section S3, Supporting Information). Rotation of the module’s major axis into the line of assembly allows the space between them to be rapidly reduced bidirectionally, thereby limiting their misalignment due to flow and/or Brownian motion before connection. Indeed, such misalignment was evident in trial designs with circular tail modules (i.e., modules holding no major axis) spaced at the minimum robust distance ($\approx 3 \mu\text{m}$) permitted by standard lithography, where module translation is the only means to close the distance between them (Section S4, Supporting Information). Furthermore, the programmed alternate counter-clockwise rotation of the triangular modules of the Tr swimmer mitigates against undesirable tip-to-corner connections before their complete alignment to the external field.

To initiate locomotion of assembled swimmers, we combine a sinusoidally oscillating x -directed magnetic field

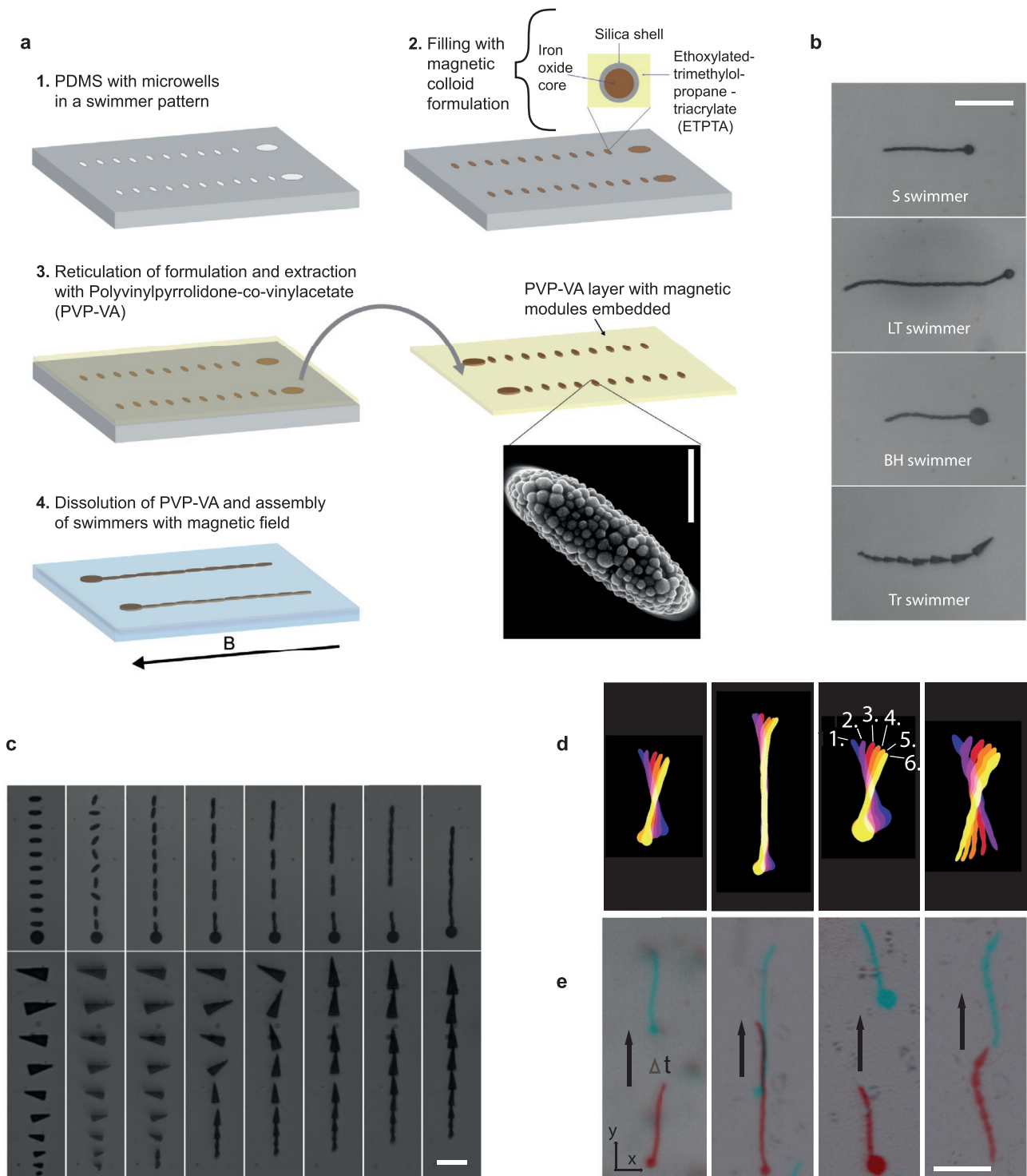


Figure 1. Fabrication, assembly, and swimming of microswimmers. a) Schematic of the fabrication and assembly of magnetic modules to microswimmers. The SEM image shows the packing of the colloid within modules. Scale bar: 2 μm . b) The swimmer designs. Scale bar: 50 μm . c) Assembly of an S swimmer (top) and a Tr Swimmer (bottom) under a magnetic field. The first frames are module release at $t = 0$ s and timings thereafter (left to right) are 9.4, 9.75, 10.55, 11.20, 12.55, 14.55, 21.05 s (S swimmer); and 5.10, 6.20, 9.00, 10.30, 12.50, 15.30, 19.05 s (Tr swimmer). Scale bar: 20 μm . d,e) Time lapses demonstrating the half stroke (d) and locomotion direction (e) of the S, LT, BH, and Tr swimmers driven by a magnetic field alternating in the x - y plane (19 Hz). In (d) temporal evolution of the half stroke is indicated with the color scheme labelled 1–6, imaged by aliasing the 19 Hz beating at 20 fps capture. The aliasing gives the optical illusion of reverse swimming. Time intervals between the swimmers in (e) are 8.85 s (S, B, and LT swimmers) and 4.55 s (Tr swimmer). The arrows indicate travel direction and the red and blue colors indicate swimmer position before and after the time interval, respectively. Scale bar: 50 μm .

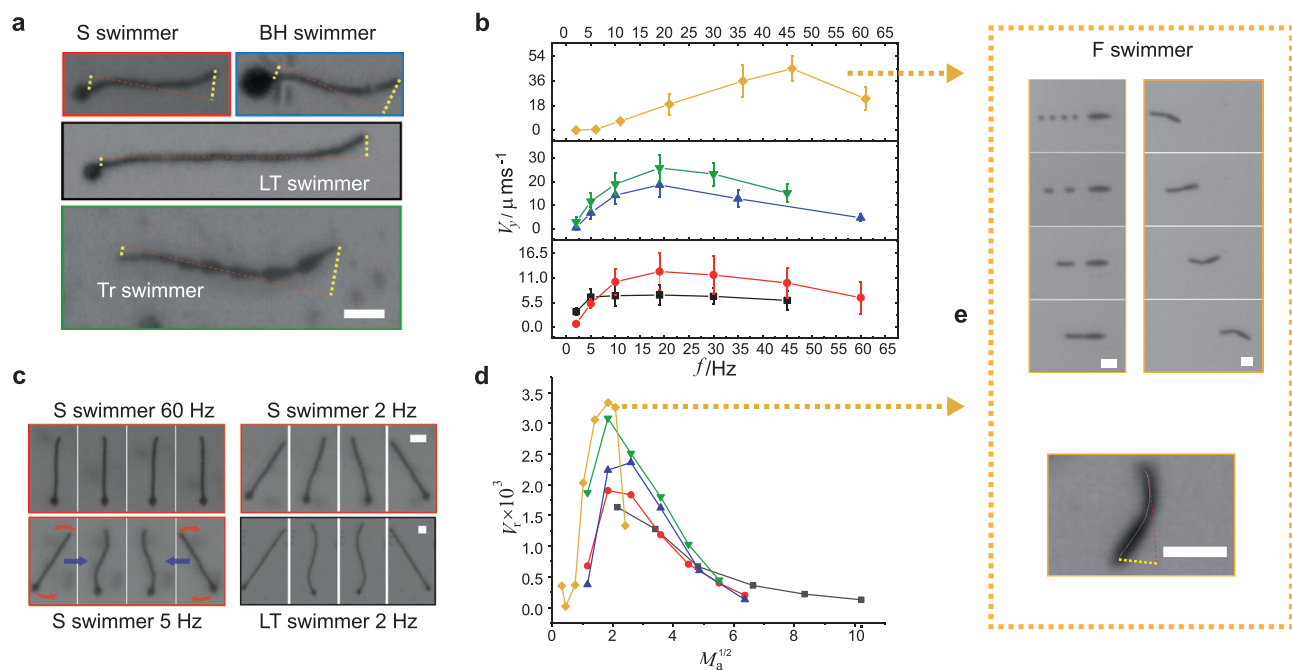


Figure 2. Swimming characteristics. a) Snapshots of S, BH, LT, and Tr swimmers during a stroke at 19 Hz with the amplitude of flex at both ends of the swimmers highlighted by dashed yellow lines. Scale bar: 20 μm . b) The absolute velocity, V_y , of S (\bullet), LT (\blacksquare), BH (\blacktriangle), Tr (\blacktriangledown), and F (\blacklozenge) swimmers with the frequency, f , of the oscillated magnetic field. The error bars are the standard deviation calculated from populations of swimmers. For each measurement between 5 and 35 swimmers were tracked. c) Snapshots of an S swimmer stroke and an LT swimmer stroke at 2 Hz. At 60 Hz, only the tips of the S swimmer actuate whereas at 5 and 2 Hz it rotates fully with flex and with a rigid-rod-like stroke, respectively. In contrast, the LT swimmer still displays flex at 2 Hz. The red arrows indicate the direction of actuation relative to the stroke extrema and the blue arrows point to the subsequent stroke confirmation. Scale bars: 20 μm . d) Plot of $M_a^{1/2}-V_p$ for S, LT, BH, and Tr swimmers. The graph key is the same as in (b). e) Left column: Fast swimmer assembly from its starting pattern of modules (left column). Timings from $t = 0$ (top panel) are 8.35 12.2, and 13.35 s. Right column: locomotion at 61 Hz showing full actuation of the F swimmer and its head first motion. Each image is 1 s apart. Bottom panel: image highlighting the flex along the length of the tail at 46 Hz. Scale bars are 20 μm .

(peak modulus = 20 mT) to the static y -field (25 mT) to produce a directionally time-varied magnetic field in the x - y plane. This moving field induces beating of the swimmers as their dipole moments move to maintain alignment with it (Figure 1d). Strikingly, the vast majority of swimmers stay connected, both during swimming and after field cessation, despite the absence of polymer connections between their modules. Such polymer connections have been required in other microscale magnetic actuators to maintain structural integrity.^[22,25,26,42,43] We suggest the absence of charged groups on our modules permits their close contact (Section S5, Supporting Information, for SEM images of contacts between modules)—contact which is then stabilized by short ranged van der Waals interactions in addition to magnetic dipole–dipole attractions during swimming. We do, however, observe that a fraction of our swimmers breaks up and/or buckle at lower frequencies, particularly in the case of the BH architecture (Section S6, Supporting Information).

On swimming, the HT designs move tail first whereas the Tr swimmers translates with their largest triangle forward (Figure 1e). The tail-first locomotion of our HT swimmers is reminiscent of an earlier magnetic swimmer, being a consequence of a field-unresponsive head restricting the capacity of nearby tail units to follow the changing direction of the magnetic field.^[22] This situation produces bending waves that propagate from the untethered tip to the head producing a greater flow of liquid in the same direction and consequently an

increased tail-first propulsion force.^[25] Likewise, despite their magnetic nature, the head units of our HT swimmers seem able to “clamp” tail motion at the tethered end. Presumably this is because the head units lack a distinctive axis in the x - y plane due to their 2D isotropic shape and homogenous packing of magnetic colloids, which leaves them largely unaffected by the rotation of the field. Nevertheless, in all HT designs head-end motion is not completely damped and some oscillation here is evident, albeit smaller than at the free end (Figure 2a). The reverse situation is true of the Tr swimmers. These swimmers move head first and far more bending originates from the largest front triangle than the smaller ones at the rear. This breaking of beating symmetry takes place despite the fact that none of the Tr modules are clamped via attachment to a non-rotating module, as in the HT swimmer situation.

As a consequence of our design control we are able to link our four distinct swimmer architectures to performance. Moving upward in sinusoidal field frequency from 2 to 60 Hz, we track the magnitude of the y -velocity of our swimmers, V_y , finding that in all cases it increases monotonically before peaking at ≈ 20 Hz and then decreasing more gradually (Figure 2b). Comparing the values of the peak velocity, $V_{y(\text{peak})}$, of our swimmers gives the following trend: Tr swimmer ($\approx 26 \mu\text{m s}^{-1}$) > BH swimmer ($\approx 18 \mu\text{m s}^{-1}$) > S swimmer ($\approx 13 \mu\text{m s}^{-1}$) > LT swimmer ($\approx 7 \mu\text{m s}^{-1}$). That the S swimmer is almost twice as fast as the LT swimmer is consistent with a

$V_y \propto 1/L$ scaling theorized for other magnetoswimmers.^[22,25,26] This scaling arises from the independence of both the magnetoviscous and elastoviscous length scale, l_m and l_p respectively, from the length of the filament, L (the pertinent length scale, either l_m or l_p , depends on the frequency, form, and makeup of the swimmer in question).^[22,25,26] As such, when $l_{m/p}$ falls short of L a greater proportion of a shorter swimmer is providing thrust in comparison to a longer one. In accordance, we find that at 19 Hz the LT swimmer holds a larger rigid, non-oscillating mid-section—that presumably only offers extra load for transport—whereas the S and BH swimmers are almost fully actuated and flexed along their length (c.f. Figure 1d; Section S7, Supporting Information, for a full stroke). Using this argument that non-actuating parts provide only load, it is unintuitive that the top velocity of the BH swimmer should exceed that of the S design; the former has a larger, heavier head that imparts increased drag. However, this bigger head further breaks the flexing symmetry of the tail to give a smaller stroke amplitude at the head end and a larger one at the free end with respect to the other HT designs. The increased tail-first propulsion force that this stroke creates is seemingly more than compensatory for the BH swimmer's greater drag which is qualitatively consistent with simulations run on similar swimmers by Gauger et al.^[27] A similar line of argument can also explain the higher top velocity of the Tr design; its front-end beats with a larger amplitude than the free ends of all HT designs. Furthermore, while a significant proportion of head-end beating at the back works against free-end beating in the HT designs, in the Tr case, back-end beating is significantly more damped with flex disproportionately evolving from its largest lead triangle and extending almost to the body length of the swimmer. This greater amount of beating at one end should generate more net thrust and therefore higher swimming velocities. By correlating the lead angles (with respect to swimming direction) of the Tr and BH designs with progressive angles along their lengths, we find that the former exhibits more decorrelation over a larger proportion of its length during a stroke at 19 Hz—in support of the above observations (Section S8, Supporting Information). We suggest that the predominant front-end beating of the Tr-swimmer is a function of its graded modular size; larger triangles are able to impart greater torque and beating amplitudes that extend over greater lengths than smaller ones. In addition, the Tr-swimmer should be more hydrodynamic than its HT counterparts. Its triangular shape (on a modular level) and its tapered width (on the swimmer body level) will decrease drag, both tangentially and parallel. Such features are a direct result of the shape, size, and arrangements of its modules, control of which is granted through our assembly method.

Despite their design differences, the swimmers display a similar range of stroke patterns. In fact, the S, BH, and Tr designs share the same frequency-dependent nature of swimming (Figure 2c; Movie S1, Supporting Information). At 2 Hz these architectures fully rotate with the field, beating with a large rigid-rod element (rigid-rod-like swimming). Between 5–30 Hz, for the S and Tr designs and 10–35 Hz for the BH architecture, the whole body of the swimmers remain actuated but their mid sections now lag the movement of their ends (full-flex swimming). Within this frequency juncture, though the swimmers rotate fully the amplitude of their beating reduces with frequency. Finally, from

45 Hz onward, only the end parts of the swimmers actuate (end-wagging swimming) with the length of these propulsive regions decreasing with frequency. In contrast, the LT design does not exhibit a rigid-rod-like stroke. Rather, at the lowest frequency (2 Hz), it swims with full flex (Figure 2c) before transforming into an end-wagging stroke from 10 Hz upward. In other words, the S, BT, and Tr swimmers move from a regime where the magnetic force dominates the viscous force at the lowest frequency to a regime where the viscous forces dominate the magnetic forces at the highest. In the case of the LT swimmer, the magnetic and viscous force are already at equivalent magnitude at the lowest sampled frequency.

These different force regimes are fully distinguished by replotting Figure 2d in terms of reduced velocity, $V_r = V_y/L_s\omega$, an indicator of swimmer efficiency, where we take L_s to be swimmer length, against an estimate of $M_a^{1/2}$ (Figure 2d; Section S9, Supporting Information). The use of M_a is appropriate as we can neglect elastic forces due to the absence of polymer bonds between our modules. Now, the S, BH, and Tr designs range $M_a^{1/2} \approx 1$ to ≈ 6.5 with a peak in V_r at $M_a^{1/2} \approx 2$ whereas the LT design extends from $M_a^{1/2} \approx 2$ to ≈ 10 with V_r reducing monotonically from $M_a^{1/2} \approx 2$. The peak in all $M_a^{1/2}-V_r$ curves corresponds to full-flex swimming, the drop at higher frequencies to the end-wagging stroke and its reduction at low frequencies—present for the S, BH, and Tr swimmers but absent in the LT design—to the rigid-rod-like stroke. This relationship between stroke character and V_r is consistent with numerical and theoretical studies on similar magnetic swimmers.^[25,27] Full-flex swimming gives high values of V_r as thrust is produced along the full length of the swimmer whereas end-wagging and rigid-rod-like swimming produces lower values because of a reduction in thrust caused by only partial actuation and the greater reciprocal nature of the stroke, respectively.^[25,27] The absence of its capacity to accommodate larger values of l_m before transitioning to full rotational swimming. Accordingly, for this design, full-flex swimming is shifted from intermediate frequencies to the lowest frequencies of our experiments and end-wagging manifests from intermediate frequencies onward—as reflected in its $M_a^{1/2}-V_r$ signature.

The above results and analysis offer clues to elevate swimming speed; designs that better break their beating symmetry and that have a full-flex stroke at higher frequencies will swim faster. To meet these requirements, we design a fast swimmer (F swimmer) that consists of an elongated oval head module (24 μm by 6 μm) attached to a short tail composed of 4 circle modules (diameter 6 μm) (Figure 2e). Note, the small number of tail modules allows their circular shape because rotation is no longer required for robust assembly. Because the length of the F swimmer is considerably smaller than the other architectures (approximately twice as short as the S swimmer) it can now be fully actuated at the highest frequencies. Further, the back and forth rotation of the high aspect ratio head produces a greater beating amplitude at the head end than at the free end (Figure 2e, bottom panel; Movie S2, Supporting Information), to produce a stroke that appears to better break its beating symmetry than the preceding 4 architectures examined.

A plot of V_y with frequency (Figure 2b, yellow diamonds) shows a velocity approaching 50 $\mu\text{m s}^{-1}$ at 46 Hz, that is,

significantly higher than previously realized, which progressively reduces at lower frequencies. This velocity is toward the top end of micromotor performance (Section S10, Supporting Information, for performance comparison of our swimmers to other leading micromotors). Plotting velocity results in terms of $M_a^{1/2}$ and V_r (Figure 2d, yellow diamonds) indicates our success in accessing full-flex swimming at higher frequencies: the peak value of V_r corresponds to an $M_a^{1/2}$ at 36 Hz whereas for the initial set of designs the peak corresponded to 2 or 5 Hz. The rapid decline in V_r at smaller values reflects the earlier transformation to a rigid-rod stroke due to the swimmer's shorter tail.

Beyond design flexibility, our assembly approach allows examination of the flock behavior of magnetoelastic swimmers. Understanding the interaction of co-moving swimmers is of practical importance—a population of swimmers can deliver more therapeutic material than a single one alone, for instance, and for the majority of in vivo applications will have to act in unison.^[12] It is also of fundamental interest; out of equilibrium collective motion is a rapidly emerging field of Physics.^[12,29,44] However, so far, experimental and numerical works on cooperative effects of synthetic locomotors have largely focused on minimal designs with no degrees of motional freedom.^[12] These studies are important for extracting baseline physics of interest to both theorists and experimentalist but for obvious reasons can never probe the importance of specific features such as flagella length, beating frequency, stiffness, etc. that are suspected to influence large scale collective behavior in living systems.^[45–48] Indeed, flexible biomimetic microswimmers are conspicuous through their absence, stymieing a decoupling of universal and case-specific cooperative behavior as well as an understanding of systems that have potentially more benefit for application. This is not by choice; the preparation of precisely engineered biomimetic microswimmers is challenging, even more so when many are required to swim in unison.^[29] By employing self-assembly to engineer joints between our swimmers we circumvent much of the taxing engineering typically required to make flexible synthetic microswimmers, thereby enabling their formation and locomotion in unison and with it a study of the collective interactions of flexible biomimetic microswimmers.

Starting from a rectangular array of Tr swimmers (≈ 50 swimmers) we witness their loose pattern formation in the early stages of locomotion; the rectangular lattice develops into a diamond-shaped one (Figure 3; Movie S3, Supporting Information). The evolution of this pattern is reminiscent of a spatial configuration generated from square arrays of magnetic discs in response to a homogenous magnetic field, to suggest the prominent role of magnetism rather than hydrodynamics.^[40]

After this initial patterning, the swimmers come together and interact predominately in pairs in four limiting cases: head-to-tail aggregation, side-by-side swimming, overtaking, and snap aggregation (Figure 4; Movie S4, Supporting Information). The first example, head-to-tail aggregation, takes place when a rear swimmer catches up and connects with a slower one directly in front. During this process (Figure 4a, region 1), we record acceleration of the chasing swimmer and deceleration of the front swimmer as they approach within a distance of $\approx 15 \mu\text{m}$. Attributed to both hydrodynamic and magnetic interactions, such acceleration effects have been anticipated in simulation work.^[49] On catchup (Figure 4a, region 2), connection does not take place

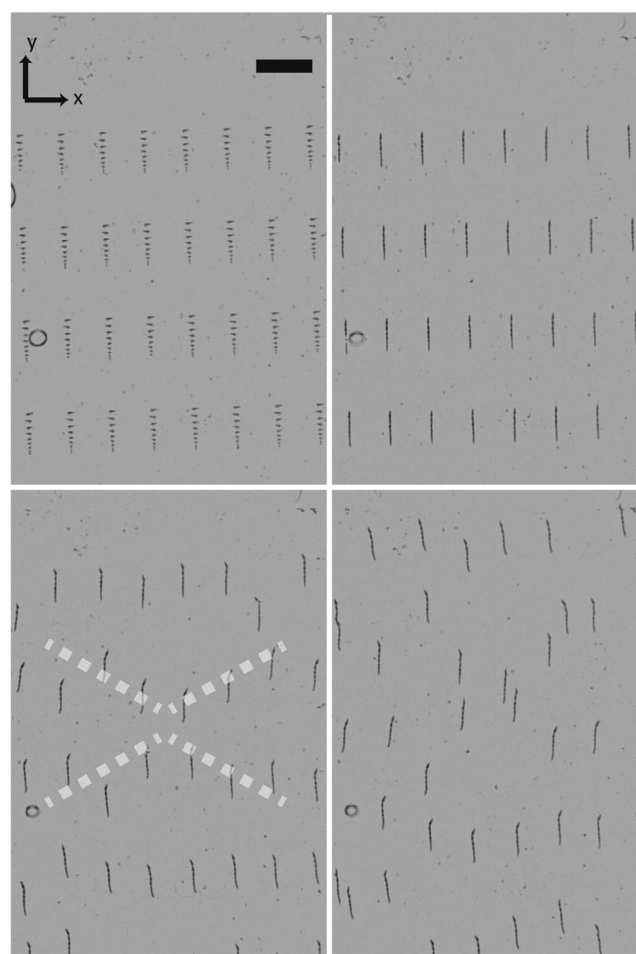


Figure 3. The assembly of a flock Tr swimmers and its evolution into a diamond-shaped arrangement. The oscillating frequency is 39 Hz and the timings after assembly at $t = 0$ s are 18.1, 33, and 41.2 s. Scale bar is $200 \mu\text{m}$.

immediately. First, a “metastable” situation is set up where the lead tip of the chaser and the back tip of the front swimmer are out of phase, causing repulsions as they move past each other close to contact. Eventually, the pair of swimmers permanently connect. In doing so, the back tip of the front swimmer is forced to beat in phase with the head of the chaser, to produce an arched beating stroke along the front half of the formed doublet. The shared velocity of the interacting, yet unconnected, pair of swimmers is $\approx 10\%$ higher than that of the permanently connected doublet. The overtaking pairing (Figure 4b.) is self-explanatory, a faster trailing swimmer moves past one in front. This process happens when the initially chasing swimmer approaches the one ahead with an x -displacement. Now, rather than connecting with the front swimmer, the chaser overshoots to the side with both swimmers moving apart further along the x -axis during the process. This x -directed repulsion is consistent with unfavorable orthogonal/near orthogonal magnetic dipole–dipole interactions. Side-by-side swimming (Figure 4c) initiates from a similar starting condition than the overtaking coupling, but now the trailing swimmer does not pass the one in front. This coupling appears stable; the swimmers beat synchronously, do not

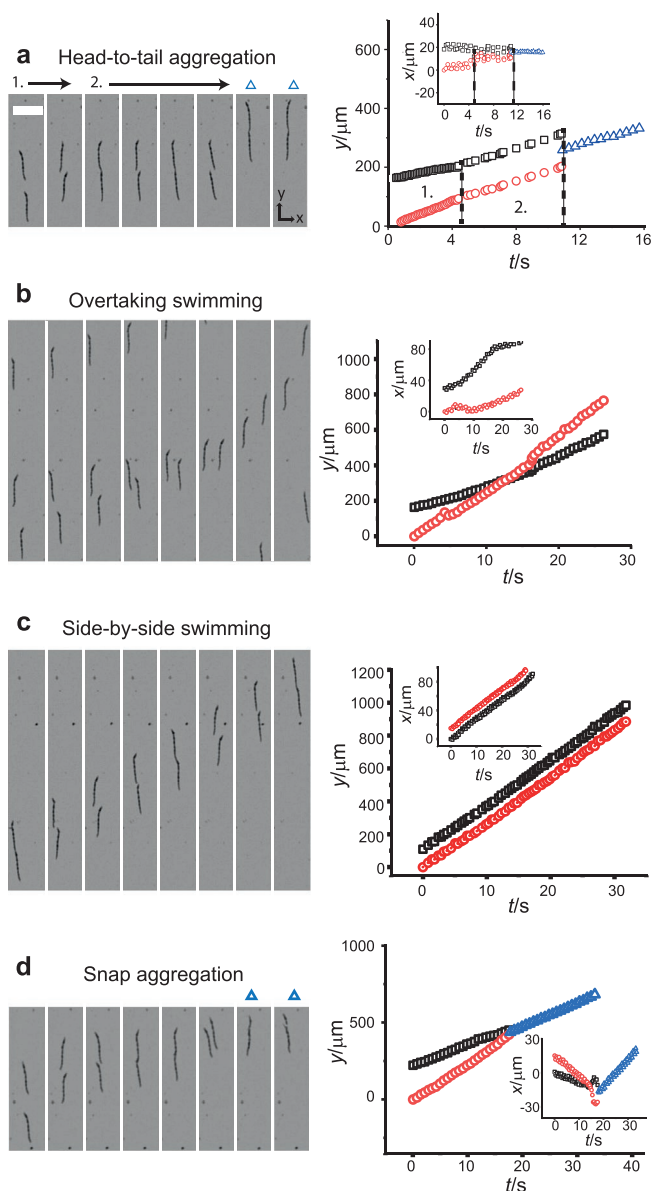


Figure 4. Swimming couplings. a–d) Image montages and trajectories of Tr swimmers during head-to-tail aggregation (a), overtaking (b), side-by-side (c), and snap aggregation (d) couplings. The montages are snapshots of the coupling interactions of the following timings (left to right): 1.00, 4.20, 4.25, 4.30, 4.35, 4.40, 12.90, and 13.30 s (head-to-tail aggregation); 10.45, 12.70, 15.15, 17.25, 19.90, 22.60, 28.25, and 36.55 s (overtaking); 3.00, 6.75, 10.50, 14.25, 18.00, 21.75, 25.50, and 29.25 s (side-by-side); 4.55, 10.80, 12.30, 13.05, 13.90, 16.95, 17.20, and 17.85 s (snap). Scale bar is 100 μm . The main graph panels show the y -positions of lead swimmers (\square), following swimmers (\circ), and aggregated states (Δ). The insets show swimmer x -position. The partitions in graph (a) show the borders between the catchup process and when swimmers touch but do not aggregate.

assemble during the length of the experiments and maintain their relative positions and shared velocity. This interaction also yields an x -component to swimming that is directed toward the x -offset of the rear swimmer with respect to the one in front. Finally, snap aggregation (Figure 4d) initiates when a chasing swimmer is able to partially swim under/over one in front. On y -overlap (due to z -displacement), both swimmers separate along

the x -direction before rapidly snapping together and connecting over a portion of their lengths. As in the head-to-tail aggregation situation, acceleration and deceleration of the back and front swimmer is evident on the former's approach, but in the case of cataclysmic aggregation a "metastable" state is not observed. Instead, aggregation takes place rapidly after some critical separation is reached. We present these flock interactions and swimmer couplings as first-case scenarios enabled by our unique assembly protocol. Subsequent work, both experimental and theoretical, will provide further insight into the specific hydrodynamic and magnetic interactions that underlay them.

In summary, we present a method to assemble flexible magnetic microswimmers that operate at the low Reynolds number limit. Assembly is programmed by the shape and relative position of the swimmers' precursor magnetic modules. While maintaining tight control over design, this methodology frees us from time-consuming approaches to engineer connections on the microscale and sidesteps the need for soft, flexible components that dependent on sophisticated processes for their development.^[2,8,9] Hence our non-invasive approach to assembly marries adaptability of design with procedural ease to allow for the rapid design optimization of complex jointed engineered architectures, an asset that will facilitate designing for application in future iterations. We demonstrate this capacity by first engineering four bespoke swimming architectures and assessing their locomotion characteristics in the context of design. Using clues obtained from these experiments we design a further swimmer optimized for speed that contains a short tail enabling it to rotate with flex at high frequencies. Beyond design control of single swimmers, our assembly technique allows parallelization: many can be made in unison in preordained positions. Such parallelization reveals four distinct couplings of swimmers, offering new avenues for swimming optimization for application and study of the collective interactions of synthetic flexible biomimetic microswimmers for the first time. Looking ahead, we are confident that our assembly protocol can be extended to engineer a zoo of functional micro-robotic devices: it remains a grand and interesting challenge to extract design rules that relate the vast combinations of starting arrangements and shapes of our modules to assembled design. Meeting this challenge will allow the production of microstructures of more complexity and functionality thereby extending application and understanding of locomotion on the microscale.

Experimental Section

Fabrication and Assembly of Magnetic Microswimmers: PDMS mold production: PDMS molds holding microwells of programmed arrangement and cross section were fabricated using standard soft-lithographical techniques and templated by an SU8 resin as detailed in ref. [39].

Preparation of magnetic colloid precursor dispersion: A dispersion of magnetic colloidal particles with a silica shell (GE Healthcare, Serasil-Mag, diameter = 400 nm) in the liquid monomer ethoxylated trimethylolpropane triacrylate (ETPTA, Sigma, $M_n \approx 428$) was used as a precursor formulation to make the magnetic modules. To enhance the stability of the magnetic particles within ETPTA, the magnetic particles were first treated at room temperature at a concentration of 0.1 v/v% within a 5:1 methanol:ammonia_(aq) (10 wt%) solution with 0.5 v/v% 3-(tremethoxysilyl)propyl methacrylate for two days. The now treated

magnetic particles were then cleaned by five cycles of centrifugation and supernatant removal with methanol before finally transferring to ETPTA at 33 v/v% with 4 v/v% of the photoinitiator 2-hydroxy-2-methyl-1-phenylpropan-1-one (Sigma) added to the final mixture.

Magnetic Micromodule Fabrication and Extraction: PDMS microwells were filled with the magnetic colloidal dispersion in ETPTA by sliding a 20 μ L droplet of it over the PDMS surface through gentle tilting of the mold. After filling, the dispersion was reticulated in the wells overnight under a 254 nm hand-held UV lamp (NU4 KL, Benda Laborgeraete). To extract the now formed modular arrays, a 4 \times 4 mm cross section of the mold was placed facedown onto a 25 μ L drop of poly(1-vinylpyrrolidone-co-vinylacetate) (PVP-VA), 70 wt% in isopropyl alcohol (Sigma), centered on a glass slide. The drop was bordered by \approx 1 mm deep frame of PDMS of inner cross section proportions of 5 \times 5 mm that forms a permanent seal with the glass slide. The slide was then left on hotplate at 200 $^{\circ}$ C for 20 s to rapidly evaporate off the isopropyl alcohol and melt the polymer. The mold was pressed into the polymer melt to ensure good contact and remove trapped bubbles and left to cool to room temperature. It was then gently peeled away to leave superparamagnetic arrays embedded in a flat layer of PVP-VA.

Assembly and Swimming of Microswimmers: For visualization of modular assembly and swimming, the glass slide holding the extracted modules was centered on a Zeiss Axiovert, 100M hal 100 microscope between a pair of NdFeB disc magnets (5 mm diameter, height 3 mm, superparamagnete) and magnetic coils (inner diameter 35mm, outer diameter 57 mm, height 15 mm 120 turns 0.85 mm Cu wire, Express Transformers) arranged orthogonally with a surface-to-surface separation of 75 mm and 30 mm, respectively. To ensure assembly of the swimmers, the long axis of their precursor modular pattern was aligned with the disc magnet pair. 50 μ L ethanediol was then used to dissolve the PVP-VA polymer and to release the magnetic modules. After assembly, a sinusoidal homogenous magnetic field was applied by the coil pair via a function generator (Agilent, 33220A) routed through an amplifier (P3000 Hafler Trans Nova) and a resistor (150 W, 3 Ω , ATE Electronics). Swimming as a function of frequency and assembly of the modules was captured using a microscope camera (USB 2.0 CMOS, Thorlabs) at 20 frames per second. The magnetic field strength produced at the center of the pair of disc magnets was 25 mT and the coils produced a maximum field strength modulus of 20 mT at their center.

Supporting Information

Supporting Information is available from the Wiley Online Library or from the author.

Acknowledgements

The authors would like to thank the German Research foundation (DFG) for funding under Project No.: TA 1375/1-1 and through the SFB1032 "Nanoagents," Project A6 and Aron Venczel for proofreading.

Open access funding enabled and organized by Projekt DEAL.

Conflict of Interest

The authors declare no conflict of interest.

Data Availability Statement

The data that support the findings of this study are available from the corresponding author upon reasonable request.

Keywords

collective behavior, microactuators, microswimmers, self-assembly

Received: September 12, 2020

Revised: January 30, 2021

Published online: March 14, 2021

- [1] E. M. Purcell, *Am. J. Phys.* **1977**, *45*, 3.
- [2] P. Liao, L. Xing, S. Zhang, D. Sun, *Small* **2019**, *15*, 1901197.
- [3] C. Calero, J. García-Torres, A. Ortiz-Ambriz, F. Sagués, I. Pagonabarraga, P. Tierno, *Nanoscale* **2019**, *11*, 18723.
- [4] K. Bente, A. Codutti, F. Bachmann, D. Faivre, *Small* **2018**, *14*, 1704374.
- [5] J. Pande, L. Merchant, T. Krüger, J. Harting, A. S. Smith, *New J. Phys.* **2017**, *19*, 053024.
- [6] D. Gong, J. Cai, N. Celi, C. Liu, W. Zhang, L. Feng, D. Zhang, *Appl. Phys. Lett.* **2019**, *114*, 12370.
- [7] A. M. Maier, C. Weig, P. Oswald, E. Frey, P. Fischer, T. Liedl, *Nano Lett.* **2016**, *16*, 906.
- [8] S. Palagi, A. G. Mark, S. Y. Reigh, K. Melde, T. Qiu, H. Zeng, C. Parmeggiani, D. Martella, A. Sanchez-Castillo, N. Kapernaum, F. Giesselmann, D. S. Wiersma, E. Lauga, P. Fischer, *Nat. Mater.* **2016**, *15*, 647.
- [9] B. Jang, E. Gutman, N. Stucki, B. F. Seitz, P. D. Wendel-García, T. Newton, J. Pokki, O. Ergeneman, S. Pané, Y. Or, B. J. Nelson, *Nano Lett.* **2015**, *15*, 4829.
- [10] I. S. M. Khalil, H. C. Dijkslag, L. Abelmann, S. Misra, *Appl. Phys. Lett.* **2014**, *104*, 223701.
- [11] E. Lauga, T. R. Powers, *Rep. Prog. Phys.* **2009**, *72*, 096601.
- [12] J. Elgeti, R. G. Winkler, G. Gompper, *Rep. Prog. Phys.* **2015**, *78*, 056601.
- [13] S. Metri, C. Hakan, H. Wenqi, J. Giltinan, T. M. S. Yim, D. Eric, *Physiol. Behav.* **2017**, *176*, 139.
- [14] A. Zöttl, H. Stark, *J. Phys.: Condens. Matter* **2016**, *28*, 253001.
- [15] E. Diller, *Found. Trends Rob.* **2011**, *2*, 143.
- [16] L. Schwarz, M. Medina-Sánchez, O. G. Schmidt, *Appl. Phys. Rev.* **2017**, *4*, 031301.
- [17] H. Xu, M. Medina-Sánchez, V. Magdanz, L. Schwarz, F. Hebenstreit, O. G. Schmidt, *ACS Nano* **2018**, *12*, 327.
- [18] M. Zhou, T. Hou, J. Li, S. Yu, Z. Xu, M. Yin, J. Wang, X. Wang, *ACS Nano* **2019**, *13*, 1324.
- [19] A. A. Solovev, S. Sanchez, M. Pumera, Y. F. Mei, O. G. Schmidt, *Adv. Funct. Mater.* **2010**, *20*, 2430.
- [20] A. P. Solon, J. Stenhammar, M. E. Cates, Y. Kafri, J. Tailleur, *Phys. Rev. E* **2018**, *97*, 020602.
- [21] B. J. Nelson, I. K. Kaliakatsos, J. J. Abbott, *Annu. Rev. Biomed. Eng.* **2010**, *12*, 55.
- [22] R. Dreyfus, J. Baudry, M. L. Roper, M. Fermigier, H. Stone, J. Bibette, *Nature* **2005**, *437*, 862.
- [23] W. Gao, X. Feng, A. Pei, C. R. Kane, R. Tam, C. Hennessy, J. Wang, *Nano Lett.* **2014**, *14*, 305.
- [24] M. Zoppello, A. D. E. Simone, F. Alouges, L. Giraldi, *AAPP Phys. Math. Nat. Sci.* **2018**, *96*, A12.
- [25] M. Roper, R. Dreyfus, J. Baudry, M. Fermigier, J. Bibette, H. A. Stone, *Proc. R. Soc. London, Ser. A* **2008**, *464*, 877.
- [26] A. Babataheri, M. Roper, M. Fermigier, O. Du Roure, *J. Fluid Mech.* **2011**, *678*, 5.
- [27] E. Gauger, H. Stark, *Phys. Rev. E: Stat., Nonlinear, Soft Matter Phys.* **2006**, *74*, 021907.
- [28] V. Magdanz, I. S. M. Khalil, J. Simmchen, G. P. Furtado, S. Mohanty, J. Gebauer, H. Xu, A. Klingner, A. Aziz, M. Medina-Sánchez, O. G. Schmidt, S. Misra, *Sci. Adv.* **2020**, *6*, eaba5855.

- [29] M. Driscoll, B. Delmotte, *Curr. Opin. Colloid Interface Sci.* **2019**, *40*, 42.
- [30] L. Kong, N. F. Rosli, H. L. Chi, J. Guan, M. Pumera, *Bull. Chem. Soc. Jpn.* **2019**, *92*, 1754.
- [31] B. E.-F. de Ávila, M. A. Lopez-Ramirez, R. Mundaca-Urbe, X. Wei, D. E. Ramírez-Herrera, E. Karshalev, B. Nguyen, R. H. Fang, L. Zhang, J. Wang, *Adv. Mater.* **2020**, *32*, 2000091.
- [32] X. Ma, K. Hahn, S. Sanchez, *J. Am. Chem. Soc.* **2015**, *137*, 4976.
- [33] V. Magdanz, S. Sanchez, O. G. Schmidt, *Adv. Mater.* **2013**, *25*, 6581.
- [34] Z. Wu, J. Troll, H.-H. Jeong, Q. Wei, M. Stang, F. Ziemssen, Z. Wang, M. Dong, S. Schnichels, T. Qiu, P. Fischer, *Sci. Adv.* **2018**, *4*, eaat4388.
- [35] J. Yu, D. Jin, K.-F. Chan, Q. Wang, K. Yuan, L. Zhang, *Nat. Commun.* **2019**, *10*, 5631.
- [36] T. Li, J. Li, K. I. Morozov, Z. Wu, T. Xu, I. Rozen, A. M. Leshansky, L. Li, J. Wang, *Nano Lett.* **2017**, *17*, 5092.
- [37] S. Tasoglu, E. Diller, S. Guven, M. Sitti, U. Demirci, *Nat. Commun.* **2014**, *5*, 3124.
- [38] J. Tavacoli, J. Heuvingh, O. Du Roure, *Materials* **2017**, *10*, 1291.
- [39] J. Tavacoli, A. Brown, P. Bauër, O. du Roure, J. Heuvingh, *RSC Adv.* **2016**, *6*, 62624.
- [40] J. Tavacoli, P. Bauër, M. Fermigier, D. Bartolo, J. Heuvingh, O. Du Roure, *Soft Matter* **2013**, *9*, 9103.
- [41] P. Bauër, J. Tavacoli, T. Pujol, J. Planade, J. Heuvingh, O. du Roure, *Sci. Rep.* **2017**, *7*, 15688.
- [42] C. Goubault, P. Jop, M. Fermigier, J. Baudry, E. Bertrand, J. Bibette, *Phys. Rev. Lett.* **2003**, *91*, 260802.
- [43] B. Kiani, D. Faivre, S. Klumpp, *New J. Phys.* **2015**, *17*, 043007.
- [44] M. Theers, E. Westphal, K. Qi, R. G. Winkler, **2018**, *14*, 8590.
- [45] M. F. Copeland, D. B. Weibel, *Soft Matter* **2009**, *5*, 1174.
- [46] W. Gilpin, M. S. Bull, M. Prakash, *Nat. Rev. Phys.* **2020**, *2*, 74.
- [47] H. H. Wensink, J. Dunkel, S. Heidenreich, K. Drescher, R. E. Goldstein, H. Lowen, J. M. Yeomans, *Proc. Natl. Acad. Sci. USA* **2012**, *109*, 14308.
- [48] C. W. Wolgemuth, *Biophys. J.* **2008**, *95*, 1564.
- [49] E. E. Keaveny, M. R. Maxey, *Phys. Rev. E: Stat., Nonlinear, Soft Matter Phys.* **2008**, *77*, 041910.

5. P2: Propulsion of Magnetic Beads Asymmetrically Covered with DNA Origami Appendages

As shown in figure 2.6, swimmers on the scale of single digit microns are typically swimming Janus particles or solid magnetic corkscrew-like swimmers. Artificial swimmers with incorporated flexibility using joints or elastic materials tend to have sizes above $5\ \mu\text{m}$ (see appendix A.1, S10). The flexible oar swimmers shown in the following paper have a size of $2\text{-}3\ \mu\text{m}$. The swimmers are produced by combining magnetic microparticles with flexible DNA origami appendages. This work builds on and adapts the work of Maier et al. [82], by switching from a corkscrew swimmer design to a flexible oar design. Rather than using tile-tube DNA assemblies the more robust six helix bundle (6HB) DNA origami structures are employed.

Initially, the creation of smaller and more flexible microswimmers was envisioned by combining DNA origami appendages with the magnetic modules produced by the soft lithographic approach. To this end, biotin-functionalized magnetic modules were made by mixing PEG-acrylate-biotin into the superparamagnetic dispersion and thereafter bind a DNA origami via biotin-streptavidin interactions. Building on this concept, methods were developed to use high-aspect ration bundles to bind the magnetic modules together prior to release to render networks. However, due to low binding specificity and yields, the magnetic modules were ultimately exchanged for commercially available magnetic beads covered with streptavidin.

Specifically, DNA origami appendages (6HB monomers and 6HB dimers) were attached via biotin streptavidin interactions to streptavidin covered magnetic microbeads (Dynabeads). Depending on the coverage, the magnetic bead reacts different to an applied wagging magnetic field. Three different particle coverages were investigated. The fully covered (FC), the predominantly covered (PC) and the hemispherically covered (HC) bead (figure 5.1a).

Exposing the differently covered magnetic beads to a wagging magnetic field showed

that the FC beads behave like Brownian particles. PC and HC beads exhibit one directional locomotion, where the direction of motion depends on the orientation of the beads easy axis in relation the DNA origami coverage (figure 5.1**b**). The maximum velocity of the PC swimmer was around 170 nm/s, while the fastest measured HC swimmer had a speed of around 500 nm/s. It can be observed, that the swimming indeed origins in the magnetic actuation of the magnetic wagging field, as shown in a experiment where swimmers were tracked under the influence of switching magnetic wagging fields off and on several times (figure 5.1**c**).

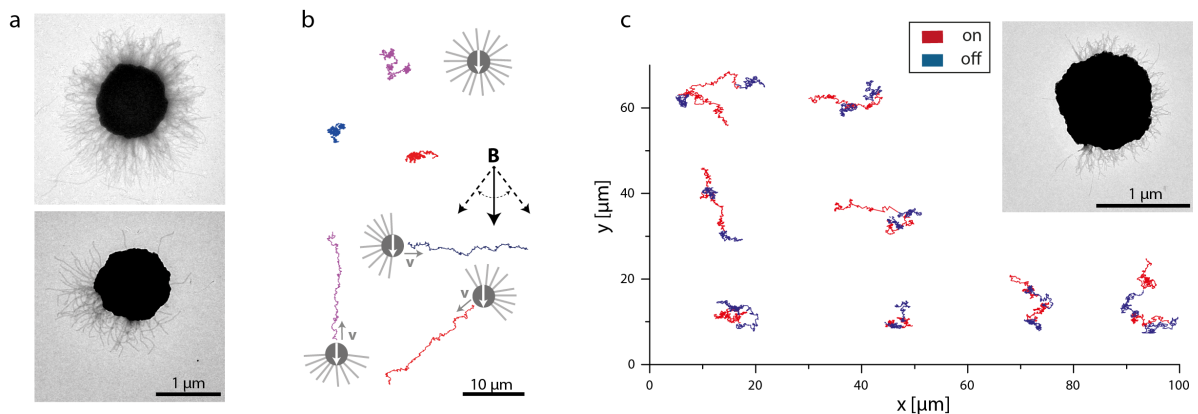


Figure 5.1.: **a** TEM micrographs of magnetic beads fully covered (FC) and hemispherically covered (HC) with 6HB dimers . **b** Tracks and added schematics (not true to scale) of full FC and HC beads in response to a wagging magnetic field. **c** Tracks with wagging magnetic field on/off of magnetic beads predominantly covered with 6HB monomers, displayed in as a TEM image. Images adapted from [2].

A directionality can be induced into the swimmers by applying a magnetic field during the grafting process, aligning the magnetic beads easy axis with the external field before the attachment of DNA origami appendages. The resulting measurements suggest an average directional control can be imposed on the magnetically aligned swimmers

There is still a lot that can be investigated in this system. For example, it is still unclear whether the DNA origami appendages contribute individually to the swimming motion or act collectively as a large paddle. Additionally, different DNA origami architectures and surface coverages could be probed. Lastly, since DNA origami is highly addressable, it would be interesting to experiment with the swimmers' capability to transport some cargo from one destination to another, controlled by magnetic fields.

On writing this thesis, it was realized that equation 1 in the supplementary material is in the wrong form affecting figure S3. This issue was fixed in this version and can be found in the appendix. It is stressed that error does not change the order of magnitude

of scaling of the Sperm number and hence the global claims of the paper.

Propulsion of Magnetic Beads Asymmetrically Covered with DNA Origami Appendages

Christoph Pauer, Aron Venczel, Mihir Dass, Tim Liedl, and Joe Tavacoli*

Eukaryotic cells that swim by the beating of nanoscale elastic filaments (flagella) present a promising locomotion paradigm for man-made analogues essential for next-generation in-vivo treatments and for the study of collective phenomena at the low Reynolds number limit. However, artificial analogues have been limited to many microns in size due to the engineering challenges of fabricating actable flexible filaments at the nanoscale—thereby narrowing the application scope. Here, made-to-order nanoscale filaments designed on the molecular level are fabricated using the DNA-origami technique. It is found that magnetic beads anisotropically covered with such bundles move in a ballistic fashion when wagged back and forth under an external magnetic field. Furthermore, by comparing bead dynamics at a range of bundle coverages and driving frequencies, compelling evidence is amassed to suggest that this ballistic motion is imparted by the beating of the DNA origami filaments as synthetic flagella. This proof-of-concept work opens up avenues for further made-for-purpose appendages designed using DNA self-assembly and with it ever more complex locomotion on the nano and microscale.


1. Introduction

The research on synthetic self-propelled microscale locomotors, or synthetic micromotors, is fast-expanding due to the potential of these devices for in/ex vivo drug and gene delivery, diagnostics, mechanical action and as platforms to research the physics of collective motion in the absence of biological complications.^[1–11] Synthetic micromotors can be divided into two subsets: those driven by external fields (magnetic, electrical, light, ultrasound etc.) and those using fuel for propulsion.^[2,5,12–16] Magnetically driven micromotors are especially attractive because of their price, biocompatibility, capacity for adaptive propulsion and for long-range autonomy suitable for deep function within the body.^[16–24] Indeed, magnetic fields are

particularly useful for imparting beating and/or rotating actuation to micromotors that mimic biological microswimmers. The seminal example is a swimmer built by Dreyfus et al. consisting of a string of magnetic beads tethered to a red blood cell.^[25] Here, swimming is induced in a derivative manner to sperm, that is, by beating a flexible appendage that supports the propagation of a bending wave. Since this breakthrough, several other bioinspired magnetic microswimmers have been fabricated, including those made from custom-made micromagnets, soft-magnetic composites and numerous architectures in which a magnetic region actuates non-magnetic flagella/appendages.^[13,15,16,20,26–29] Increasingly, the role of appendage architecture on swimming performance is being investigated, demonstrating that swimming speed varies with its length, elasticity, and stroke frequency for both biological

and synthetic systems.^[15,26,28,30] Furthermore, it has been established that collective interactions of biological microswimmers are delicately dependent on coupled flagellar (appendage) dynamics and flows generated at sub-flagellum length scales.^[30] These interactions are exploited in nature to facilitate performance: mice sperm, for instance, form long trains that enhance their velocity.^[7,10,30–33] Nevertheless, rigorous control of appendage design for synthetic systems remains taxing, even more so when nanoscale features are required. A particularly promising approach to achieving such control on the nanoscale is DNA self-assembly, as employed by Maier et al. to generate synthetic flagella based on DNA tile-tube bundles.^[26] When attached to rotating magnetic beads, these bundles hydrodynamically assembled into a corkscrew-like confirmation of several micrometers to drive translational motion in a manner analogous to bacteria. Though the assembly technique permitted exquisite control of twist and stiffness of the synthetic flagella, their length was subject to oligomerization and uncontrolled. In this communication we build on the work of Maier et al. by using an alternative DNA self-assembly strategy, DNA origami. Here a single-stranded DNA loop of 8634 nucleotides is folded in a pre-determined manner by the specific binding of single-stranded DNA oligomers to build bespoke, nanoscale appendages of controlled dimension.^[34–37] We present a method to modulate the coverage of our appendages onto magnetic beads uniformly or with broken symmetry. On rocking these constructs via a time-dependent magnetic field, we find that while architectures fully covered with the DNA origami exhibit largely Brownian kinetics,

C. Pauer, A. Venczel, M. Dass, T. Liedl, J. Tavacoli
Faculty of Physics and Center for NanoScience
Ludwig-Maximilians-Universität
Geschwister-Scholl-Platz 1 80539, München, Germany
E-mail: j.tavacoli@lmu.de

 The ORCID identification number(s) for the author(s) of this article can be found under <https://doi.org/10.1002/admt.202200450>.

© 2022 The Authors. Advanced Materials Technologies published by Wiley-VCH GmbH. This is an open access article under the terms of the Creative Commons Attribution License, which permits use, distribution and reproduction in any medium, provided the original work is properly cited.

DOI: 10.1002/admt.202200450

symmetry broken architectures i.e. beads partially covered with DNA origami, move in a ballistic manner consistent with a swimming mechanism. Finally, we realize directionality into our swimmers upon assembly by introducing a constant magnetic field during the grafting procedure, thereby advancing these constructs toward controlled delivery application on the microscale.

2. Results and Discussion

The foundation of our synthetic appendages is a six helix-bundle (6HB) DNA origami.^[38–40] These bundles have a defined length (≈ 490 nm), thickness (6–8 nm) and persistence length (1.88–2.7 μm).^[39] Moreover, we note that in comparison to DNA tile-tubes, and more generally, the bundles are a well-established design that may be robustly assembled at high yields, controllably oligomerized end-to-end and functionalized at predetermined sites to direct their binding to external functional groups of choice and are a platform with significant design space for future performance optimization.^[38,39] These factors make them ideal proof-of-concept DNA origami geometries

to act as slender bodies for low Reynolds number propulsion. Indeed, such types of bundles have already shown suitability for controlled micron-scale actuation on application of electric fields and when tethered to magnetic particles and have also been carried by gold nanoparticles in thermophoretic flows.^[41–45] As actuating units, we use streptavidin-covered magnetic Beads (MyOne, streptavidin T1, diameter = 1 μm) that experience torque if their magnetic easy axis is misaligned to an external magnetic field.^[46,47] By functionalizing one end of our 6HBs with biotin we exploit the streptavidin-biotin interaction to attach them to the surface of the magnetic beads, with the long axis of the bundles on average directed outward from the surface of the bead. We undertake grafting with the beads positioned in three distinct settings: 1) in bulk, that is, the beads fully dispersed, 2) the beads resting on a flat interface and 3) with the beads partially sitting within PDMS microwells. Using these distinct grafting environments, we can adjust the grafting coverage to fabricate beads fully covered with 6HBs (FC beads, setting 1), beads predominately covered with bundles (PC beads, setting 2) and beads hemispherically covered with bundles (HC beads, setting 3) (Figure 1a). For clarity, whereas the FC

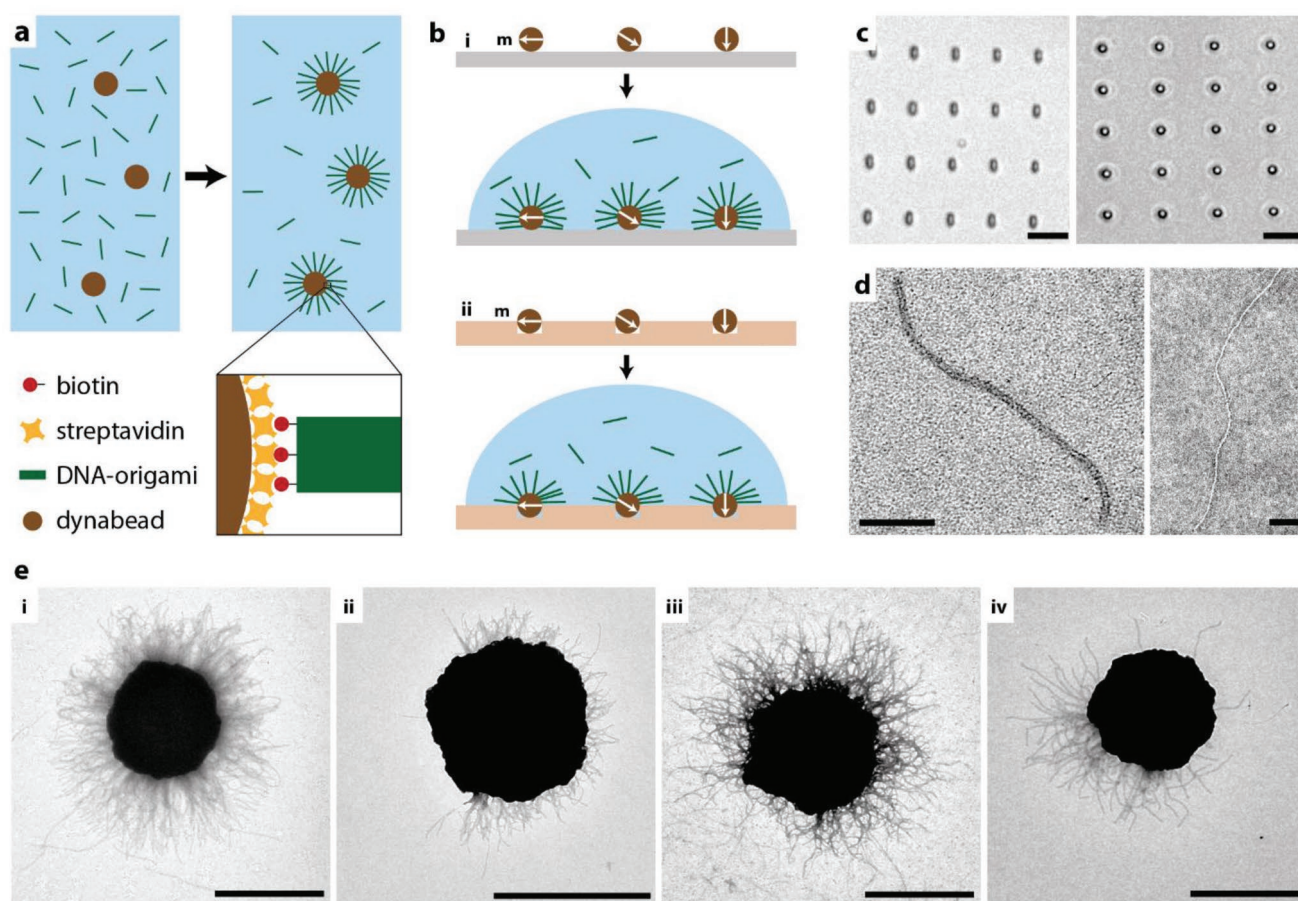


Figure 1. The grafting of biotin-capped DNA origami 6HBs onto streptavidin-functionalized magnetic beads. a) Grafting took place in bulk, b.i) on a flat glass substrate, and ii) trapped in PDMS microwells to produce fully covered (FC) beads, predominately covered beads (PC) beads and hemispherically covered (HC) beads, respectively. In addition, PC beads grafted with 6HB monomers were prepared (PCM). c) Bright-field microscopic images of a PDMS mold used for the preparation of HC beads, empty (left) and populated with native beads (right). Scale bars: 5 μm . d) TEM micrographs of a 6HB monomer (left) and dimer (right). Scale bars are 100 nm. e) TEM micrographs of i) FC beads, ii) PCM beads, iii) PC beads, and iv) HC beads (6HB dimers). Scale bars: 1 μm .

beads have an isotropic architecture, the PC and HC beads sets are inherently symmetry-broken designs, with the HC design being the most sparsely covered. We make 6HB dimers (end-to-end length $\approx 1 \mu\text{m}$) by coupling 6HB monomers tip-to-tip using complementary base pair interactions (so-called 'sticky ends') and bind them to the beads in all of the grafting scenarios. In contrast to the dimer configuration, we also prepare PC beads populated with monomers of 6HB (PCM). We employ a time-varied transverse magnetic field in the x - y plane to rock our beads back and forth around a fixed axis in the z -plane. We adjust the frequency, f , of the field and track the motion of individual beads sedimented to the base of an enclosed cell. For a population of beads, we extract the magnitude of a mean velocity, v , by fitting a mean square displacement to a function incorporating both Brownian and ballistic dynamics (Figure 2, refer to Section S1, Supporting Information).^[48] In doing so, we find that the PC and HC bead populations move ballistically in random orientations, characterized by f - v curves with a mean velocity maximum at intermediate frequencies on the order of 100 nm s^{-1} (Figure 2a-i,iii,iv,b). In contrast, the FC beads (and native Dyna beads and FCM system (Section S2, Supporting Information)) show only Brownian dynamics when subject to the imposed time-varied magnetic field, resulting in a flat f - v curve (Figure 2a-ii,c). This distinction between symmetry-broken bead architectures and isotropic ones is revealing. It strongly infers that the ballistic motion of the former is not a consequence of flow, magnetic field gradients, biased rolling, or any intrinsic property of the DNA origami bundles. Instead, the motion is most consistent with the bundles acting as flexible appendages that create thrust by supporting a bending wave generated by the oscillation of the magnetic beads, that is, swimming. Such a swimming mechanism parallels the sinusoidal whip-like motion of sperm flagella. Indeed, this method of propulsion is compatible with the baseline physics of our system; for the 6HBs to induce effective locomotion via a bending wave, the elastic and drag forces acting on them must be well matched. We estimate a viscous-elastic force ratio from 1–10 for the frequency range of our experiments (Section S3, Supporting Information), values associated with efficient swimming at low Reynolds number.^[25,49,50] To further certify this mode of transport, we adjust the amplitude of the oscillating field at 50 Hz, and with it the amplitude of bead rocking, to extract PC bead velocity for a single micromotor. We find that the bead's velocity increases monotonically with amplitude, consistent with the velocity scaling of a bending wave at a fixed wavelength (Section S3, Supporting Information).^[51]

Swimming via appendage beating also offers a rationale for the key features of our experiments. For instance, we can understand the non-ballistic activity of the FC beads in terms of zero net-thrust creation as any propulsive forces generated would isotropically emanate outward via the corona of bundles. In contrast, the symmetry broken architectures would produce net thrust aligned and opposite with the 6HB orientation and consequently move ballistically, as observed. The random direction of their paths then results from the arbitrary orientation of the bundles with respect to the beads' magnetic easy axis; though the latter orientate with the direction of the fluctuating magnetic field, the bundles do not. Propulsion will therefore be generated in a range of directions. Derivatives of these

arguments, albeit qualitatively, also explain the top velocities reached by HC beads, PCM beads and PC beads: $\approx 300 \text{ nm s}^{-1}$, $\approx 200 \text{ nm s}^{-1}$ and $\approx 120 \text{ nm s}^{-1}$ respectively (Figure 2a). The highest velocity of the HC beads can be rationalized by noting a greater portion of its 6HBs can create thrust in the same direction in comparison to the PC beads, where many of the bundles will work opposingly to lower the net-thrust-to-drag ratio. The intermediate velocity of the PC monomer system is then consistent with a reduced drag acting on the bead (due to its shorter bundles) than the PC dimer design.

In addition, we mention that the maxima form of the f - v curves is consistent with data reported on other synthetic microswimmers employing a beating stroke. In these cases, the peak velocities at intermediate frequencies reflect the optimal balance of efficient stroke form and beating frequency.^[15,25,49,50] However, a full analysis of our curves must not only account for the length, coverage and density of the bundles on the beads, but also their frequency sensitive stroke patterns and the nature of bead actuation with frequency.^[47] Such an analysis is beyond the scope of this communication, being the subject of ongoing theoretical work. Nevertheless, from a practical perspective, the curves demonstrate that one can use field frequency to select for an average velocity of choice. For the HC beads, we can choose between limits of 80 – 250 nm s^{-1} within the frequency range of our experiments. Beyond mechanistic understanding, it is also evident that we have realized the first DNA origami-based micromotors. Purely ballistic micromotors have demonstrated effective active-agent delivery on the microscale.^[52]

Because external fields drive our micromotors, we can trigger their activity on and off. Figure 3a displays this situation for the HC beads, where their reversible transfer from Brownian to ballistic dynamics is evident. The same figure also highlights some nuances in the motion of our microdevices. For instance, we observe an occasional $|\pi|$ switch in their trajectory on removing and reapplying the external field. This directional switch most likely arises from the magnetic beads' known π periodicity of magnetic symmetry and its coupling to a Brownian rotation $> |\frac{1}{2} \pi|$ during the beads' field-off periods.^[46] We also notice a prevalence of short-lived $|\frac{1}{2} \pi|$ changes in directions. This behavior is harder to account for. We cautiously suggest its relation to a theorized $|\frac{1}{2} \pi|$ flip in the magnetization vector when the phase lag between the time-varied field and the easy axis of magnetization approaches $|\frac{1}{4} \pi|$ —but further investigation is required to understand this phenomenon.

Figure 3a additionally demonstrates (along with the error bars for f - v plots) that whilst, on average, the PC and HC beads have a clear signature of ballistic motion, significant variability in their displacements, i.e. swimming velocities, exist for given frequencies. Most dramatically, in the case of the HC population driven at 80 Hz, the fastest individual swimmer attains a velocity close to $1 \mu\text{m s}^{-1}$, whereas the motion of the slowest of the same population can be attributed to thermal noise alone (Section S4, Supporting Information). A portion of this heterogeneity of performance undoubtedly stems from our magnetic beads: magnetic torsional stiffness differences of as much as 30% have been reported for those employed here, attributed to subtle variations in the distribution, shape and size of their iron oxide content.^[46] Consequently, seemingly equivalent beads may be optimally driven at distinct frequencies.^[47]

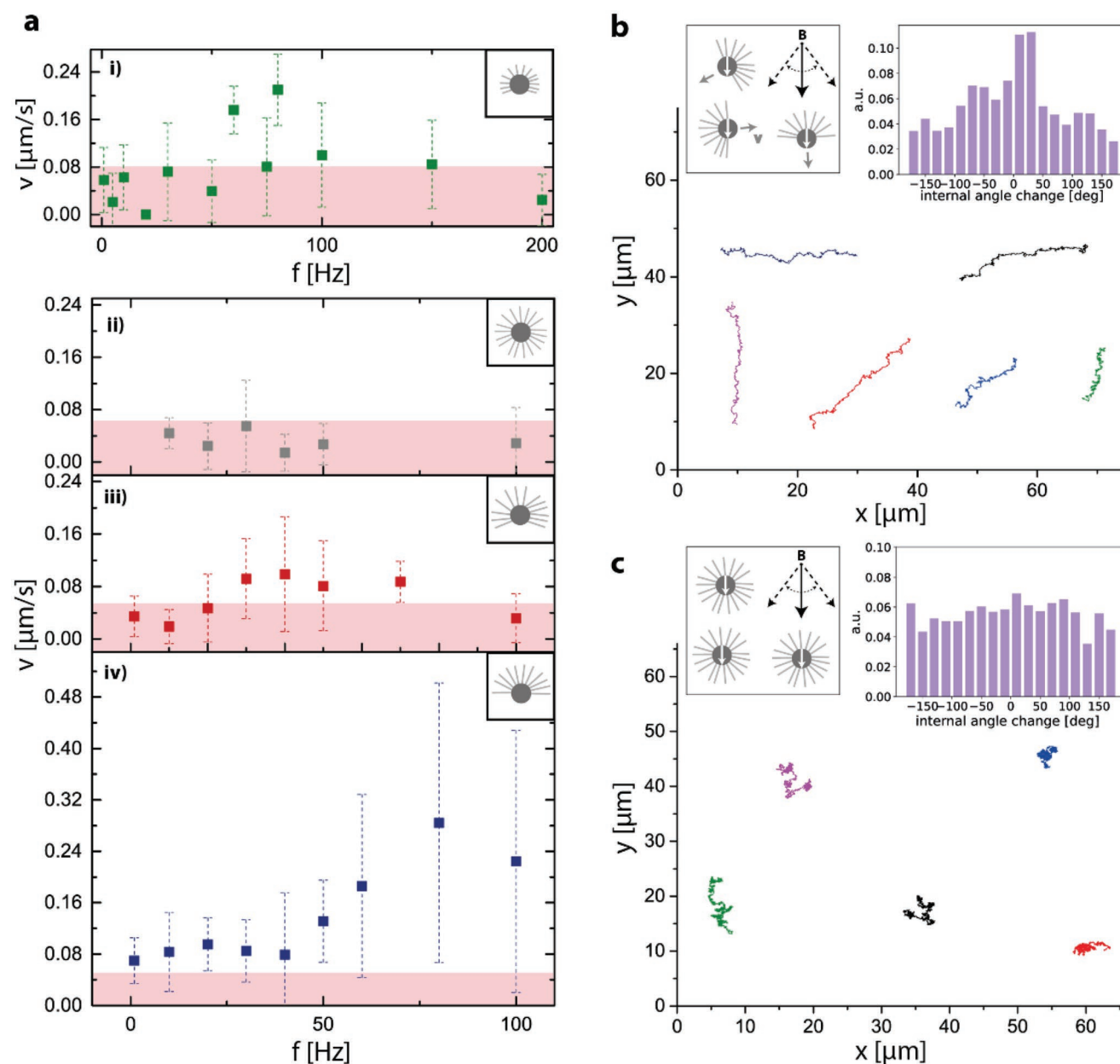


Figure 2. a) Magnetic field frequency, f , and average bead velocity, v , curves for i) PCM beads, ii) FC beads, iii) PC beads, and iv) HC beads. Each measurement is averaged over 3 to 15 swimmers, and error bars are standard deviation. Red regions on curves indicate maximum drift recorded using MSD analysis in field-off periods before and after experiments in the presence and the absence of the constant portion of the applied magnetic field (see Experimental Section, “Swimming experiments and analysis”). The size of the error bars is due to the polydispersity of the swimmer, stemming from the degree of origami coverage and its magnetic anisotropy b) Tracks of HC beads showing ballistic motion when subjected to an oscillating magnetic field at 70 Hz. c) Tracks of FC beads showing motion consistent with Brownian dynamics when oscillated at 50 Hz. Both track sets span 60 s. The inset panels in (b) and (c) depict the idealized bead architecture and the distribution of the internal angle of the tracks. A peak centered on 0° suggests ballistic motion and a flat distribution Brownian motion. All tracks originate from the same field of view but have been reorganized in the x - y frame for image clarity.

TEM micrographs also reveal that grafted batches have a distribution in 6HB bundle coverage (Section S5, Supporting Information). This distribution will lead to bead-to-bead variation in viscous drag, propulsion generation and ultimately performance. Further divergence of action could arise from the random position of the bundles with respect to the beads’ easy magnetic axis: thrust, as generated by a bending

wave, would transverse zero to a maximum in the x - y plane as bundle position changes from orthogonal to parallel to said plane, respectively.

In addition to switchable kinetics, we can impart directionality to our 6HB decorated beads through facile adaptation to our grafting procedure. Specifically, we better align the magnetic easy axis with that of the bundles by repeating

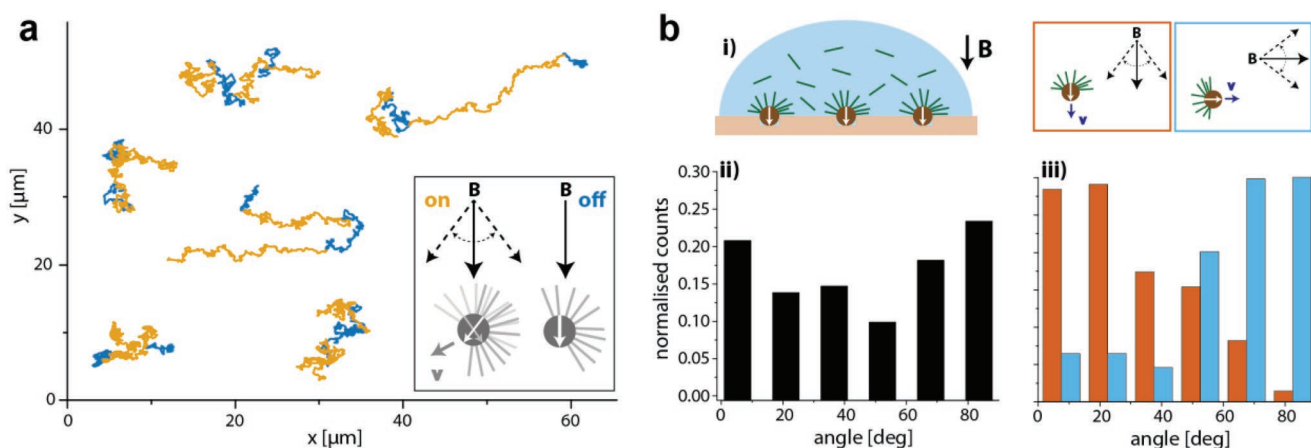


Figure 3. a) Tracks of HC beads on application and removal of an oscillating magnetic field at 60 Hz. Timings are 20 s (off), 60 s (on), 40 s (off), and 60 s (on). The tracks originate from the same field of view but have been reorganized in the x–y frame for image clarity. b) Magnetically aligned hemispherically covered beads (MAHC). i) Schematic of the preparation of MAHC beads. ii) The angle distribution of vectors spanning the starting and end positions of HC beads with the magnetic field fluctuating around 90° (orange box in (i)) and iii) the vector angle distribution for MAHC beads with a magnetic field fluctuating around 90° and 0°. The histograms were averaged over 68 and 34 beads for the HC and MAHC beads, respectively. Angular symmetries are collapsed to populate a 0–90° range.

the grafting methodology utilized for the HC beads under a 30 mT magnetic field, applied orthogonal to the grafting plane (Figure 3b). The thus formed magnetically aligned HC beads (MAHC beads) locomote predominately along the time-average direction of the fluctuating magnetic field. Furthermore, by rotating said field by $|\frac{1}{2}\pi|$ we induce a $\pm\frac{1}{2}\pi$ directional change to their path (Figure 3b-iii). Such directionality broadens the application potential of our devices, particularly in the realm of in/ex vivo targeted treatment. Despite their relatively modest top velocities, the devices seem well suited to such a task not only due to their biocompatible nature but because their actuation with homogenous fields permits their long-distance operation as required for in vivo functionality. Moreover, besides providing thrust, the DNA origami bundles can automatically capture and release cyclic drugs and act as vectors for cellular uptake. The addressable nature of DNA origami also provides scope for customized treatments in the future which as far as we are aware is absent in other micromotors.^[53–55]

3. Conclusion

To conclude, in this communication, we have outlined a procedure to fabricate magnetic beads decorated with custom-made DNA origami bundles. Employing an adaptive grafting procedure, we can modulate the surface coverage of the beads from full to anisotropically covered. On their magnetic actuation, the dynamics of fully covered beads can be understood by thermal motion alone, whereas the anisotropically covered sets display ballistic dynamics. This ballistic behavior can be explained by the action of the DNA origami bundles as beating appendages to induce swimming on the microscale. There is still much to be understood about our system: primarily, in the picture we have set out, it is still to be elucidated whether the origami bundles beat as individual units

or whether they operate collectively as a single large paddle formed by inter bundle entanglements. Nevertheless, looking forward, we note the potential of our micromotors for bio-compatible active-agent delivery on the microscale; DNA origami bundles are excellent capture and release reservoirs for a variety of cyclic drugs.^[55] Moreover, whilst we have employed the robust and well understood 6HB DNA origami as appendages in this POC work, there is considerable scope for alternative DNA origami designs from which to generate further adaption to and understanding of nano/microscale motion.

4. Experimental Section

Monomers and Dimers Preparation: Briefly, two sets of six helix bundles (6HB) were designed using the Cadnano2 software (<https://github.com/douglaslab/cadnano2>).^[37] The first set was functionalized at one end with biotin, via complementary base pair staples. For end-to-end oligomerization of the bundle sets, a system of empty scaffold regions and complementary single-stranded intrusion staples were employed, and C4-end staples were used to prevent unwanted polymerization (S6). Two C bases were present on the biotin tagged end for the same purpose. Both structures were first folded separately on a linear temperature ramp from 65 to 20 °C for 19 h without the intrusion-end staples and then purified using PEG precipitation.^[56] The individual sets of 6HBs were folded at 10 nM concentration of the 8634 scaffold, 10× excess of core staples, and 30× excess of end staples in a buffer containing 1× TE and 18 mM MgCl₂. The scaffold was produced in-house, the staples were purchased from Integrated DNA Technologies. The two purified sets of 6HBs were added together 1:1 to dimerize overnight at 37 °C. The dimer product was separated from remnant monomers using a standard gel electrophoresis protocol.

Grafting of DNA Origami Decorated Magnetic Beads: The biotin-functionalized DNA origami structures were grafted onto streptavidin-covered magnetic beads (Invitrogen, Dynabeads MyOne Streptavidin T1, diameter 1 μm) in three distinct ways to make fully covered beads, partially covered beads, and hemispherically covered beads as follows.

Fully Covered Beads: Magnetic beads were mixed in bulk with the 6HBs (bead:6HBs, 1:100) in TAE gel buffer (40 mM Tris, 20 mM acetic acid, 1 mM EDTA, 11 mM MgCl₂) and incubated at room temperature

overnight. The beads were cleaned in TAE gel buffer via 5 cycles of magnetic collection and supernatant removal.

Partially Covered Beads: A 100 μL droplet of diluted Dynabeads (0.005 nM) in 1 \times TE buffer (10 mM Tris 1 mM EDTA) with 11 mM MgCl_2 was deposited on a glass slide and left for one hour to ensure sedimentation of the beads to the glass surface where they remained stuck. After washing 5 times in TAE gel buffer, a further 100 μL droplet of gel buffer with 6HBs (1 nM) was added and incubated at 4°C overnight in a sealed container to avoid evaporation. After grafting, the beads were collected by pipetting TAE gel buffer with 0.1 wt% sodium dodecyl sulfate (Sigma), which promoted their detachment from the glass substrate. The beads were cleaned as before.

Hemispherically Covered Beads: Here, Dynabeads were prepared at 40 vol% in a solution of SDS-saturated glycerol (distilled water (15 vol%) and glycerol (30 vol%)). The as-produced viscous dispersion was gently wiped over a PDMS mold holding oval microwells with a long (short) axis of 3 μm (2 μm) and well depth of ≈ 2 μm to leave each well populated with a single bead. The mold was fabricated following standard soft lithographical procedures. The grafting and cleaning protocol of the partially covered beads' system was then repeated.

To align the magnetic easy axis of the beads with the bundles the grafting procedure was repeated in the presence of a 30 mT field aligned with the vertical axis of the mold.

A full description of the above methods employed can be found in Section S6, Supporting Information.

Swimming Experiments and Analysis: After loading the beads in a sealed optical cell, measurements were performed on a Zeiss Axiovert, 100M hal microscope mounted with a pair of oppositely positioned NdFeB disc magnets (35 mm diameter, height 3 mm, superparamagnete) orthogonal to an oppositely positioned pair of magnetic coils (inner diameter 35 mm, outer diameter 57 mm, height 15 mm, 120 turns with 0.85 mm Cu wire, Express Transformers) with a surface-to-surface separation of 75 mm and 30 mm, respectively. To induce motion, a sinusoidal homogenous magnetic field was applied by the coil pair via a function generator (Agilent, 372 33220A) routed through a 200 W power supply (Kepco BOP20-10DL-802E). The following time-varied field was used: $B(t) = B_y + B_x(t)$ where $B_y = 15$ mT was a constant field in the y-direction and $B_x = B_m \sin((f/2\pi)t)$ with $B_m = 7$ mT.

Bead kinetics were recorded with a Thorlabs CMOS Camera (Thorlabs Kiralux CS895CU) using 20 \times objective at either 5 fps or 32.6 fps. ImageJ's tracking add-on, TrackMate, was employed to extract the tracks from which the mean square displacement, velocity, and internal angle for each particle was calculated with a custom Python script.^[57]

Supporting Information

Supporting Information is available from the Wiley Online Library or from the author.

Acknowledgements

The authors would like to thank the German Research Foundation (DFG) for funding under projects TA 1375/1-1 and SFB1032 "Nanoagents," Project A6. MD has received funding from the European Union's Horizon 2020 research and innovation program under the Marie Skłodowska-Curie Grant Agreement No. 765703. The authors would also like to thank Helena Massana-Cid and Carlos Calero Borrallo for advice and stimulating discussion.

Open access funding enabled and organized by Projekt DEAL.

Conflict of Interest

The authors declare no conflict of interest.

Authors Contribution

A.V. and C.P. contributed equally to this work. A.V., C.P., and J.T. performed experiments, analyzed results, and contributed to manuscript production. M.D. advised with DNA Origami design. J.T. and T.L. supervised work and conceptualized experiments.

Data Availability Statement

The data that support the findings of this study are available from the corresponding author upon reasonable request.

Keywords

biofabrication, DNA origami, drug delivery, Janus particles, microrobotics, microswimmers, self-assembly

Received: March 19, 2022

Revised: May 13, 2022

Published online: July 24, 2022

- [1] G. Gompper, R. G. Winkler, T. Speck, A. Solon, C. Nardini, F. Peruani, H. Löwen, R. Golestanian, U. B. Kaupp, L. Alvarez, T. Kiørboe, E. Lauga, W. C. K. Poon, A. DeSimone, S. Muiños-Landin, A. Fischer, N. A. Söker, F. Cichos, R. Kapral, P. Gaspard, M. Ripoll, F. Sagues, A. Doostmohammadi, J. M. Yeomans, I. S. Aranson, C. Bechinger, H. Stark, C. K. Hemelrijk, F. J. Nedelec, T. Sarkar, et al., *J. Phys.: Condens. Matter* **2020**, *32*, 193001.
- [2] M. Fernández-Medina, M. A. Ramos-Docampo, O. Hovorka, V. Salgueiriño, B. Städler, *Adv. Funct. Mater.* **2020**, *30*, 1908283.
- [3] Z. Wu, J. Troll, H.-H. Jeong, Q. Wei, M. Stang, F. Ziemssen, Z. Wang, M. Dong, S. Schnichels, T. Qiu, P. Fischer, *Sci. Adv.* **2018**, *4*, eaat4388.
- [4] U. Bozuyuk, O. Yasa, I. C. Yasa, H. Ceylan, S. Kizilel, M. Sitti, *ACS Nano* **2018**, *12*, 9617.
- [5] P. Illien, R. Golestanian, A. Sen, *Chem. Soc. Rev.* **2017**, *46*, 5508.
- [6] L. Schwarz, M. Medina-Sánchez, O. G. Schmidt, *Appl. Phys. Rev.* **2017**, *4*, 031301.
- [7] J. Elgeti, R. G. Winkler, G. Gompper, *Rep. Prog. Phys.* **2015**, *78*, 056601.
- [8] S. Metri, C. Hakan, H. Wenqi, J. Giltinan, M. Turan, S. Yim, D. Eric, *Physiol. Behav.* **2017**, *176*, 139.
- [9] B. J. Nelson, I. K. Kaliakatsos, J. J. Abbott, *Annu. Rev. Biomed. Eng.* **2010**, *12*, 55.
- [10] M. F. Copeland, D. B. Weibel, *Soft Matter* **2009**, *5*, 1174.
- [11] E. Lauga, T. R. Powers, *Rep. Prog. Phys.* **2009**, *72*, 096601.
- [12] V. M. Kadiri, J.-P. Günther, S. N. Kottapalli, R. Goyal, F. Peter, M. Alarcón-Correa, K. Son, H.-N. Barad, M. Börsch, P. Fischer, *Eur. Phys. J. E* **2021**, *44*, 74.
- [13] V. Magdanz, I. S. M. Khalil, J. Simmchen, G. P. Furtado, S. Mohanty, J. Gebauer, H. Xu, A. Klingner, A. Aziz, M. Medina-Sánchez, O. G. Schmidt, S. Misra, *Sci. Adv.* **2020**, *6*, eaba5855.
- [14] M. R. Bailey, F. Grillo, N. D. Spencer, L. Isa, *Adv. Funct. Mater.* **2022**, *32*, 2109175.
- [15] C. Pauer, O. du Roure, J. Heuvingh, T. Liedl, J. Tavecchi, *Adv. Mater.* **2021**, *33*, 2006237.
- [16] D. Ahmed, C. Dillinger, A. Hong, B. J. Nelson, *Adv. Mater. Technol.* **2017**, *2*, 1700050.
- [17] F. Martinez-Pedrero, H. Massana-Cid, P. Tierno, *Small* **2017**, *13*, 1603449.

- [18] A. Kaiser, A. Snezhko, I. S. Aranson, *Sci. Adv.* **2017**, *3*, e1601469.
- [19] M. Driscoll, B. Delmotte, *Curr. Opin. Colloid Interface Sci.* **2019**, *40*, 42.
- [20] F. Qiu, B. J. Nelson, *Engineering* **2015**, *1*, 21.
- [21] H. Massana-Cid, F. Meng, D. Matsunaga, R. Golestanian, P. Tierno, *Nat. Commun.* **2019**, *10*, 2444.
- [22] V. Magdanz, S. Sanchez, O. G. Schmidt, *Adv. Mater.* **2013**, *25*, 6581.
- [23] D. Gong, J. Cai, N. Celi, C. Liu, W. Zhang, L. Feng, D. Zhang, *Appl. Phys. Lett.* **2019**, *114*, 123701.
- [24] H.-W. Huang, F. E. Uslu, P. Katsamba, E. Lauga, M. S. Sakar, B. J. Nelson, *Sci. Adv.* **2019**, *5*, eaau1532.
- [25] R. Dreyfus, J. Baudry, M. L. Roper, M. Fermigier, H. A. Stone, J. Bibette, *Nature* **2005**, *437*, 862.
- [26] A. M. Maier, C. Weig, P. Oswald, E. Frey, P. Fischer, T. Liedl, *Nano Lett.* **2016**, *16*, 906.
- [27] P. Liao, L. Xing, S. Zhang, D. Sun, *Small* **2019**, *15*, 1901197.
- [28] B. Jang, E. Gutman, N. Stucki, B. F. Seitz, P. D. Wendel-García, T. Newton, J. Pokki, O. Ergeneman, S. Pané, Y. Or, B. J. Nelson, *Nano Lett.* **2015**, *15*, 4829.
- [29] J. Ali, U. K. Cheang, J. D. Martindale, M. Jabbarzadeh, H. C. Fu, M. Jun Kim, *Sci. Rep.* **2017**, *7*, 14098.
- [30] S. F. Schoeller, E. E. Keaveny, *J. R. Soc. Interface* **2018**, *15*, 20170834.
- [31] J. Yan, H. Monaco, J. B. Xavier, *Annu. Rev. Microbiol.* **2019**, *73*, 293.
- [32] S. F. Schoeller, W. V. Holt, E. E. Keaveny, *Phil. Trans. R. Soc. B* **2020**, *375*, 20190384.
- [33] H. S. Fisher, H. E. Hoekstra, *Nature* **2010**, *463*, 801.
- [34] C. E. Castro, F. Kilchherr, D.-N. Kim, E. L. Shiao, T. Wauer, P. Wortmann, M. Bathe, H. Dietz, *Nat. Methods* **2011**, *8*, 221.
- [35] H. Dietz, S. M. Douglas, W. M. Shih, *Science* **2009**, *325*, 725.
- [36] P. W. K. Rothmund, *Nature* **2006**, *440*, 297.
- [37] S. M. Douglas, A. H. Marblestone, S. Teerapittayanon, A. Vazquez, G. M. Church, W. M. Shih, *Nucleic Acids Res.* **2009**, *37*, 5001.
- [38] S. M. Douglas, J. J. Chou, W. M. Shih, *Proc. Natl. Acad. Sci. U. S. A.* **2007**, *104*, 6644.
- [39] D. J. Kauert, T. Kurth, T. Liedl, R. Seidel, *Nano Lett.* **2011**, *11*, 5558.
- [40] S. M. Douglas, H. Dietz, T. Liedl, B. Högberg, F. Graf, W. M. Shih, *Nature* **2009**, *459*, 414.
- [41] A. Herms, K. Günther, E. Sperling, A. Heerwig, A. Kick, F. Cichos, M. Mertig, *Phys. Status Solidi A* **2017**, *214*, 1600957.
- [42] S. Lauback, K. R. Mattioli, A. E. Marras, M. Armstrong, T. P. Rudibaugh, R. Sooryakumar, C. E. Castro, *Nat. Commun.* **2018**, *9*, 1446.
- [43] E. Kopperger, J. List, S. Madhira, F. Rothfischer, D. C. Lamb, F. C. Simmel, *Science* **2018**, *359*, 296.
- [44] B. Shen, V. Linko, H. Dietz, J. J. Toppari, *Electrophoresis* **2015**, *36*, 255.
- [45] F. Kroener, L. Traxler, A. Heerwig, U. Rant, M. Mertig, *ACS Appl. Mater. Interfaces* **2019**, *11*, 2295.
- [46] M. M. van Oene, L. E. Dickinson, F. Pedaci, M. Köber, D. Dulin, J. Lipfert, N. H. Dekker, *Phys. Rev. Lett.* **2015**, *114*, 218301.
- [47] X. J. A. Janssen, A. J. Schellekens, K. van Ommering, L. J. van IJzendoorn, M. W. J. Prins, *Biosens. Bioelectron.* **2009**, *24*, 1937.
- [48] M. J. Saxton, in *Methods in Membrane Lipids* (Ed: A. M. Dopico), Humana Press, Totowa, NJ **2007**, pp. 295–321.
- [49] E. Gauger, H. Stark, *Phys. Rev. E – Stat., Nonlinear, Soft Matter Phys.* **2006**, *74*, 021907.
- [50] M. Roper, J. Baudry, M. Fermigier, J. Bibette, H. A. Stone, *Proc. R. Soc. A* **2008**, *464*, 877.
- [51] G. Taylor, *Proc. R. Soc. London A* **1951**, *209*, 447.
- [52] L. Kong, N. F. Rosli, H. L. Chi, J. Guan, M. Pumera, *Bull. Chem. Soc. Jpn.* **2019**, *92*, 1754.
- [53] Q. Jiang, S. Liu, J. Liu, Z. Wang, B. Ding, *Adv. Mater.* **2019**, *31*, 1804785.
- [54] Q. Jiang, C. Song, J. Nangreave, X. Liu, L. Lin, D. Qiu, Z.-G. Wang, G. Zou, X. Liang, H. Yan, B. Ding, *J. Am. Chem. Soc.* **2012**, *134*, 13396.
- [55] H. Ijäs, B. Shen, A. Heuer-Jungemann, A. Keller, M. A. Kostianen, T. Liedl, J. A. Ihalainen, V. Linko, *Nucleic Acids Res.* **2021**, *49*, 3048.
- [56] E. Stahl, T. G. Martin, F. Praetorius, H. Dietz, *Angew. Chem., Int. Ed.* **2014**, *53*, 12735.
- [57] J.-Y. Tinevez, N. Perry, J. Schindelin, G. M. Hoopes, G. D. Reynolds, E. Laplantine, S. Y. Bednarek, S. L. Shorte, K. W. Eliceiri, *Methods* **2017**, *115*, 80.

6. Magnetic nanorotor

This project continues the effort of Götzfried (see section 2.4.3) to create a magnetically actuated nanorotor. Here, the magnetic nanoparticles are ferrimagnetic and are placed closer to each other to promote interaction. In the ideal case, all individual particles' magnetic moments point in the same direction, creating an easy axis along the DNA origami bundle. The functionalization of ferrimagnetic nanoparticles and their attachment to DNA origami was shown by Lak et al. in 2023 [3] (see section 3.3). The functionalized mNPs can be attached to DNA origami with nanoscale precision or in a numerous manner (figure 6.1) in the same way as functionalized noble nanoparticles.

The magnetic nanorotor consists of a six-helix-bundle (6HB) DNA origami structure folded from the p7249 scaffold, covered with 96 extensions for magnetic nanoparticles (mNPs) along the sides and 42 extensions to attach fluorescent dyes (Atto655) at one end of the structure (see appendix). The length of the structure is 413 nm. The other end of the bundle carries an extension holding a biotin making it possible to mount the 6HB to the surface via biotin-streptavidin interactions, while at the same time being able to freely rotate around the pivot point.

6HBs with attached fluorescent dyes and streptavidin is mounted to a SPB treated glass slide (see section 3.5) via biotin-streptavidin-biotin interactions. Afterwards, functionalized mNPs are attached to the DNA origami's complementary extensions. This grafting process is schematically shown in figure 6.2a. On application of a time-varied circular magnetic field ($\mathbf{B} = B_0 \sin(\omega t)\hat{\mathbf{x}} + B_0 \cos(\omega t)\hat{\mathbf{y}}$) and a static homogeneous one ($\mathbf{B} = B_0\hat{\mathbf{y}}$), the rotors are seen to circulate and clamp, respectively (figure 6.2b and c).

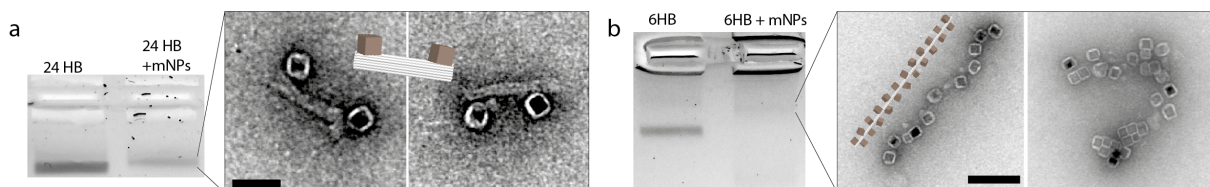


Figure 6.1.: Gels of DNA origami with and without mNPs attached and the corresponding TEM images of marked band. **a** Locally at designated binding sites on a 24HB and **b** numerous mNPs attach to a 6HB, scale bars are **a** 50 nm and **b** 100 nm.

6.1. Rotation

This is presumably as the attached mNPs want to align with the field vector. Specifics of these rotation and clamping experiments are presented directly below.

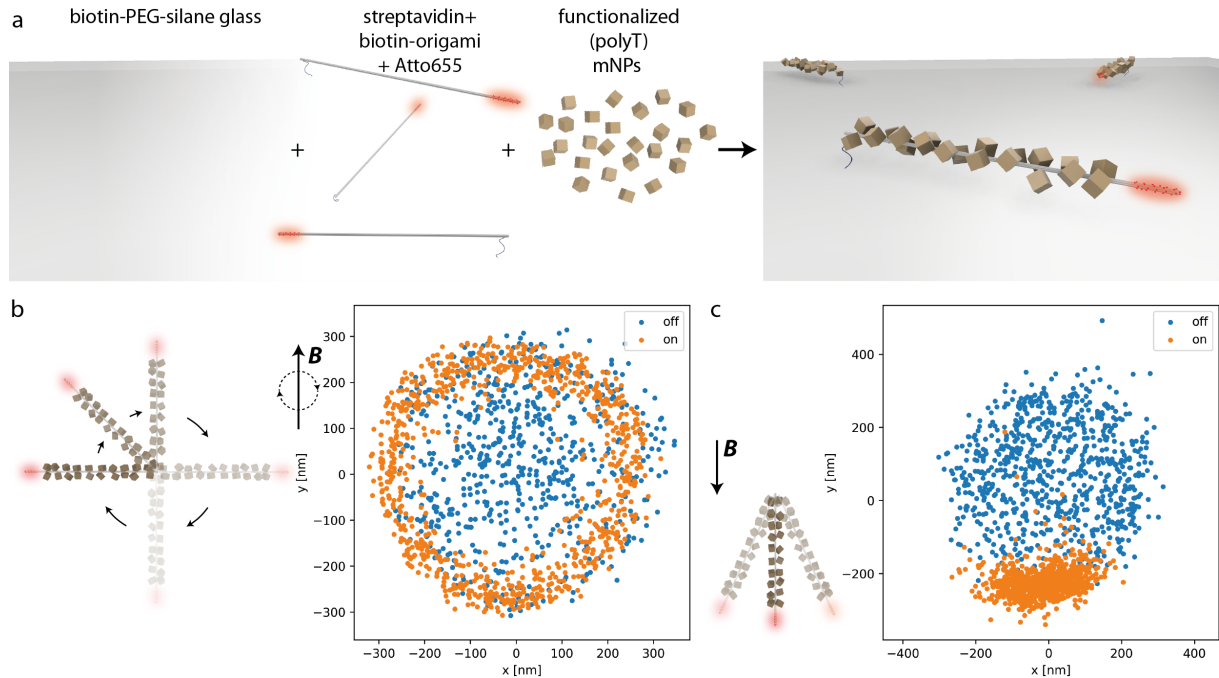


Figure 6.2.: **a** Fabrication of the magnetic nanorotors on the SPB treated glass surface. In a two step process the prefolded DNA origamis with attached Atto655 dyes are bound to the surface, then the magnetic particles get attached to the DNA origami. **b, c** Rotation and clamping of a magnetic nanorotor respectively: sketch next to plotted x-y-localizations with and without applied B-field.

6.1. Rotation

To extract the x-y-localizations of the fluorescent dyes at the end of the rotors, a software tool called Picasso was used. Picasso was originally written for the superresolution microscopy technique DNA-PAINT, developed by the Jungmann group [118] and is freely available on GitHub [119]. On a given input file, Picasso Localize identifies bright spots depending on the parameters set by the user. The important ones being the box size and the gradient. Then, point-spread-functions are used to find the centers of the spots fitting in the given box size and having a greater gradient than the given threshold. In Picasso Render, the found localizations can be plotted and drift corrected. The relevant parameters for this project are the x-y-coordinates and the frame number, to calculate the time dependency. Using these parameters, the radius, the angle and the cumulative angle of the rotor over time can be calculated.

The observed frequency f_o of the rotors, extracted from the rotors' datasheet (figure 6.3), can match the applied frequency f_a of magnetic field until it reaches a critical frequency. The critical frequency f_c can be used to approximate the torque acting on the rotor using equation 2.8. To find this critical frequency, increasingly higher frequencies f_a were applied to the rotors until f_o breaks down as in unable to keep up with f_a .

For these first initial experiments, the setup used could only provide reasonable data up to 100 fps: At higher frequencies the autofocus could not be used because a strong focus shift which could not be manual adjusted as a visual preview at this high frame rates is not supported by the software. Due to this technicality, there are not enough data points to convincingly fit sine functions at higher frequencies than 10 Hz. For future experiments, this issue will be fixed by using an aluminum stage instead of a 3D printed nylon stage, resulting in a much more robust setup.

To simulate drag conditions at higher frequencies, the viscosity of the medium can be increased (see equation 2.8 and 2.9). Here, a 48% sucrose-buffer mixture was used, which was reported to have 12.5 times higher viscosity than aqueous solutions [90].

The data shown in figure 6.4 shows the best performing rotors out of a highly heterogeneously sample. A large variety of rotor performance is evident. Understanding the exact root of this variation will be the focus of future work, but it is like to arise from the heterogeneity in the number and orientation of bound mNPs as well as the individual energy landscapes of each rotor due to the molecular variability of the substrate [92]. This variety can be observed in figure 6.4, where the number N of rotors in the dataset significantly decrease at $f_a > 2$ Hz in aqueous solutions. It is also reflected in the magnetic torque of rotors with $T_r = 0.58 - 36.1 \cdot 10^{-21}$ Nm. The torque was calculated using equations 2.9 and 2.8 with the lower limit measured in aqueous solutions and the upper limit in a 48% sucrose-buffer mixture. Using $f_c = 2$ Hz in aqueous solutions with viscosity η_w as a lower limit and $f_c = 10$ Hz in sucrose-buffer mixture η_{ws} for the upper limit torque calculations, with $\eta_{ws} = 12.5 \cdot \eta_w = 12.5 \cdot 0.89$ mPas = 11.125 mPas (at room temperature $T=25^\circ\text{C}$), $L = 400$ nm, $D = 50$ nm (10 nm for the origamis diameter and twice 20 nm for the mNPs).

The torque balance employed here does not take into account the interactions with the substrate, which increases drag [120]. Therefore, the produced range of torque represents a conservative estimation of the upper and the lower boundaries of the torque spread.

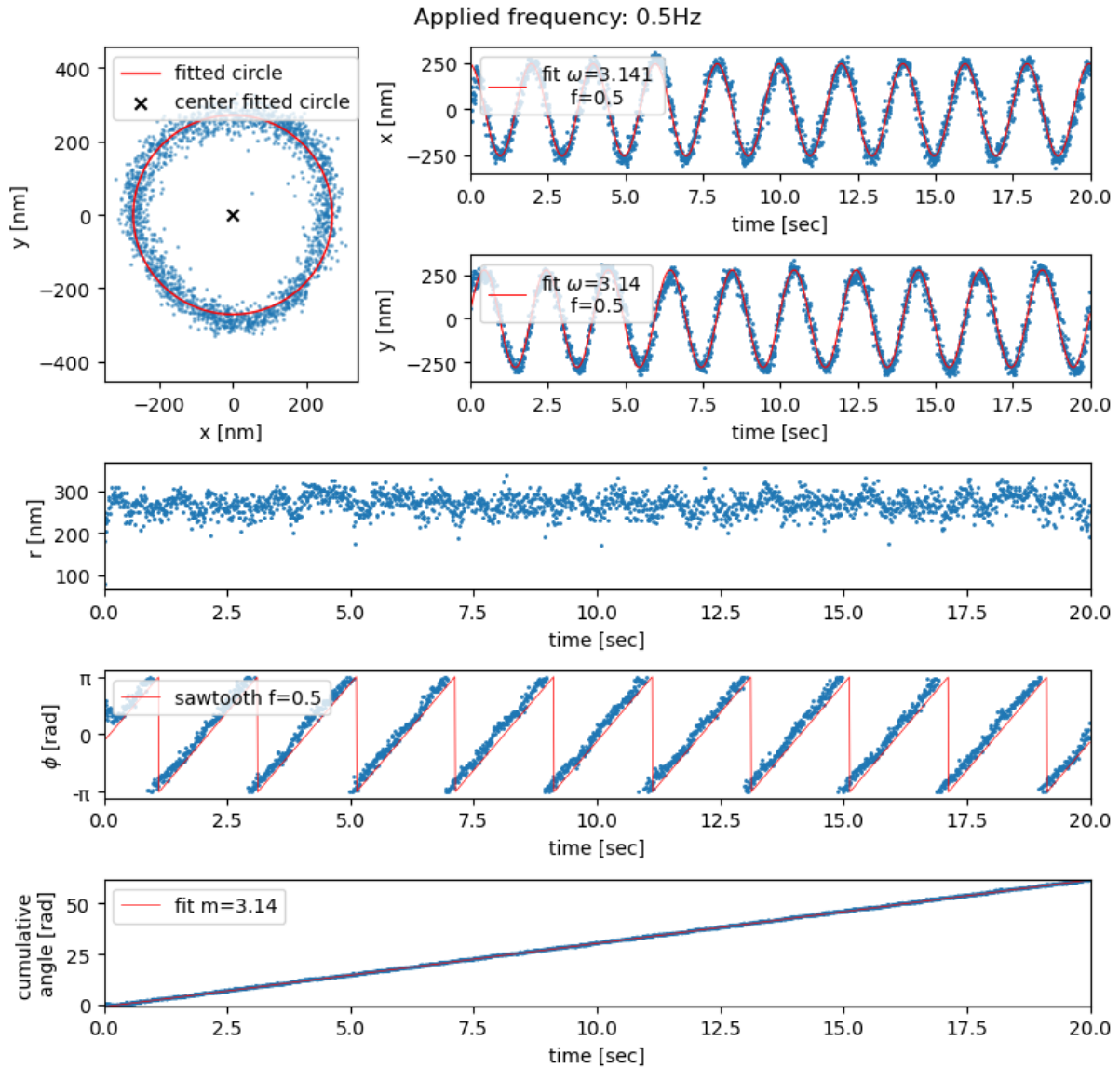


Figure 6.3.: Datasheet of an exemplary rotor with an applied rotating magnetic field with a frequency $f = 0.5$ Hz and a magnetic field strength of $B_0 = 2.7$ mT. **a** shows the relative x-y-coordinates and a circular fit to the data. **b**, **c** show relative x and y-coordinates over time respectively with a sinusoidal function fitted to determine the frequency f . **d** shows the radius over time, **e** shows the angle ϕ over time with a fitted sawtooth function with frequency f . **f** shows the cumulative angle over time.

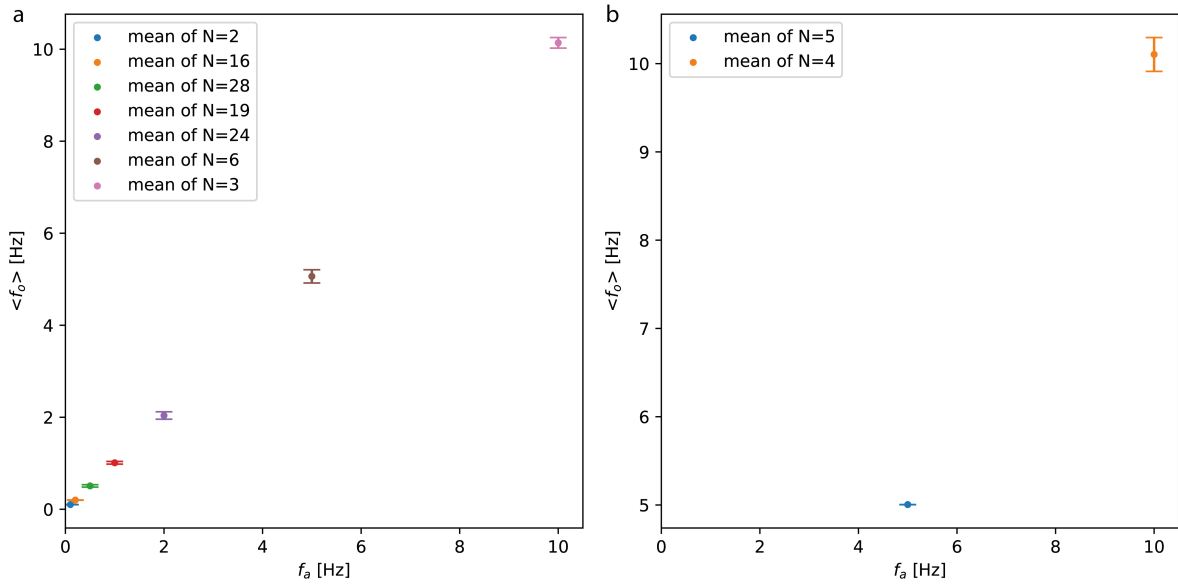


Figure 6.4.: Variety of frequencies f_a where applied to magnetic nanorotors in **a** buffer under aqueous conditions and **b** buffer containing 48% sucrose. The mean and the standard deviation of the observed frequency f_o are plotted in relation to f_a . The applied field strength was $B_0 = 2.7$ mT.

6.2. Clamping

The clamping experiments were performed on the same field of view by applying a homogeneous magnetic field with a field strength of $B_0 = 1.1$ mT to 7.4 mT. Figure 6.5 shows the plotted relative x-y-coordinates for different magnetic field strengths B_0 . It can be observed, that the higher B_0 , the smaller is the variety of positions, which also means that the torsional stiffness k of the rotor increases with increasing B_0 .

The distribution of the angle ϕ is plotted for rotor 0 in figure 6.6 **a**. It shows that the distribution gets narrower with an increasing B-field. From the variance of the angular distribution $\text{var}(\phi)$, the torsional stiffness k can be approximated by [121]:

$$k = \frac{k_B T}{\text{var}(\phi)} \quad (6.1)$$

with the Boltzmann constant $k_B = 1.3810 \cdot 10^{-23}$ J/K and the room temperature $T = 298$ K. Figure 6.6**b** shows the torsional stiffness k of the three rotors from figure 6.5 depending on the applied B-field.

6.2. Clamping

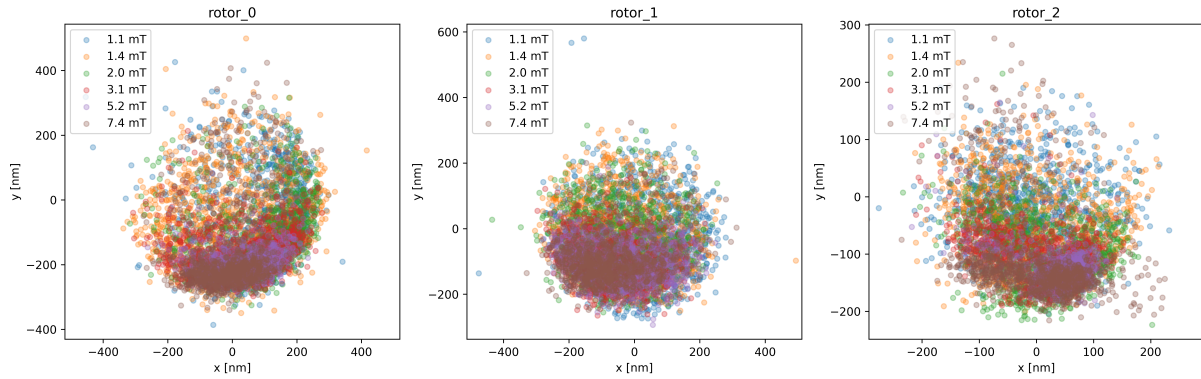


Figure 6.5.: x-y-coordinates of three rotors reacting to a homogeneous B-field applied in y-direction at different field strengths.

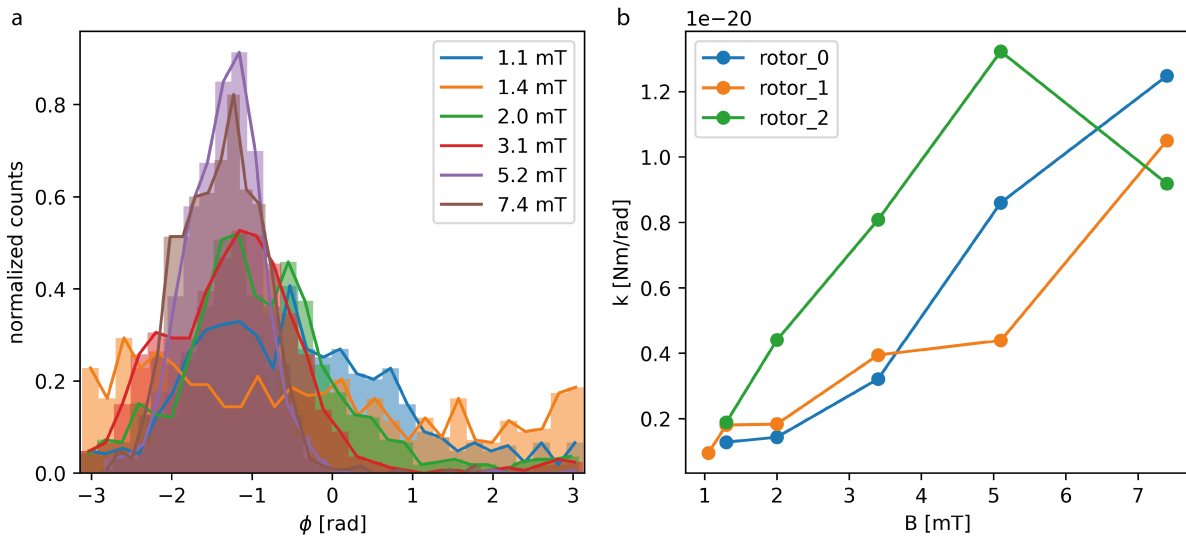


Figure 6.6.: a Angular distribution of ϕ and b torsional stiffness k for different rotors depending on the B-field.

7. Data analysis of darkfield images and videos

In addition to working on magnetic systems, I developed data processing pipelines for physical unclonable functions (PUFs). PUFs are structures fabricated in a way that their reproducibility with the same production procedure is essentially zero due to the randomness in the fabrication process. The PUF's physical uniqueness acts as a fingerprint and potentially can be used for identification and authentication. Here, optical PUFs were created (see section 7.1) appearing as randomly colored hexagonally arranged spots under the DFM.

My contribution to this project lays in the data analysis of the DFM images and videos. Extracting the colors of individual spots to create the mean color distribution of the PUFs or exhibiting the color change depending on the polarization. To achieve this goal, I wrote a python script, that takes advantage of image manipulation libraries like OpenCV and skimage to process the image data (see appendix).

7.1. PUF fabrication

The PUFs were produced by patterning glass slides via nanosphere lithography. This process uses single particle layer of polystyrene nanospheres closely packed on an oxygen plasma activated glass surface, priming it with HMDS (hexamethyldisilazane) under vacuum and removing the spheres using ultrasonication. This procedure creates a hydrophobic surface with hydrophilic spots where the spheres were sitting. DNA origami is placed on the hydrophilic spots via magnesium bridges with silanol groups. Afterwards, functionalized nanoparticles are attached to the DNA origami via hybridization of complementary DNA strands (figure 7.1a, b). Using plasmonic nanoparticles with different materials (silver, gold) and shape (spheres, rods) leads to a variety of actually bound particles to an origami, whereby each origami has bound different amounts of particles in a spatially different configuration (figure 7.1c). Under darkfield microscopy, the placed origami with attached particles appear as colorful spots (figure 7.1d), where the color depends on the

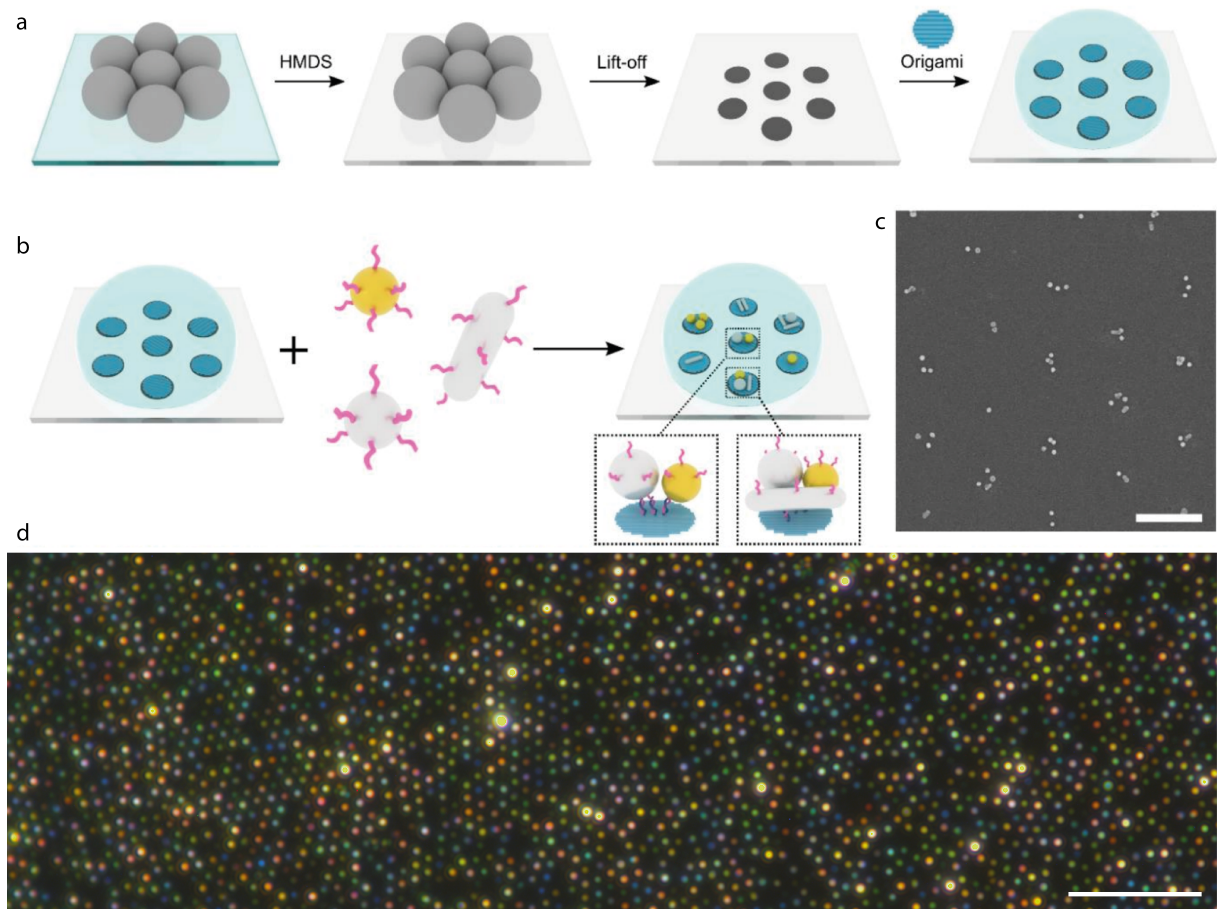


Figure 7.1.: **a** schematically shows nanospheres placed on O_2 -plasma treated glass, primed with HMDS making the exposed surface hydrophobic, removing the spheres and placing DNA origami on hydrophilic spots. **b** illustrates the attachment of plasmonic nanoparticles to DNA origami. **c**, **d** SEM (Scanning Electron Microscopy) and DFM image of the product. Scale bars are 500 nm and 10 μm respectively. Images adapted from [4].

particle properties (material, shape, size), the amount and the coupling of the plasmonic nanoparticles.

7.2. Image/video processing and analysis

7.2.1. Image processing and hue analysis of plasmonic PUFs

The optical PUFs are imaged using DFM, appearing as bright colorful spots arranged in hexagonal lattice with a dark (to ideally black) background (figure 7.1d). The color of a pixel is digitally stored by using the three colors red, green and blue with varying intensities, also known as the RGB model. HSV is another color model with three parameters

hue, saturation and value. Hue describes the type of the color and in physics it is referred to as the wavelength, saturation is the amount of color, where 0% saturation results in a gray scale pixel, and value describes the brightness, where 0% brightness results in a black pixel. Because the value is a measure of brightness, the model is also known as HSB (hue, saturation, brightness) model.

To extract the hues of an DFM image, the following image processing pipeline was created (figure 7.2): First, the region of interest (part of the full image like shown in figure 7.2 or the full image size (4096x2160 px)) is transformed to a grayscale image. A dummy particle is created by drawing a circle with a 7 px radius and applying a Gaussian blur to it. Matching the template with the grayscale image results in a correlation map. Extracting the peaks of the correlation map gives the x-y-coordinates of the particles center. For each particle, a 20x20 px area around the x-y-coordinate can be combined using a *logical-and* function with a binary mask of the dummy particle to extract the particles data. This operation can be done with the original RGB image, the grayscale image or an HSV image depending on the desired parameters. Thereby, the HSV image can easily be obtained by transforming the RGB image. The measured data is plotted in a histogram to visualize the color distribution of the PUF.

7.2.2. Polarization dependent color change

Anisotropic plasmonic particles emit polarized light. By using a polarization filter in a DFM, the measured signal differs depending on the angle of the filter. To visualize this effect, the optical response has been measured with varying angles of the polarization filter, from 0° to 360° in intervals of 10°. All the images were packed together in a video, where each frame corresponds to a 10 ° change in angle of the filter. Equivalent to the image processing, the x-y-coordinates of the desired particles are obtained by matching a dummy particle to a grayscale image of the first frame of the video. After drift-correction of the video, circles with a radius of 4 pixels are placed on the x-y-coordinates acting as a stencil to extract the data in the area of the circle for every frame. The harvested data, for example the mean hue, can be plotted for each particle either in a line plot when only a few particles are observed, or using a colormap to visualize multiple particles.

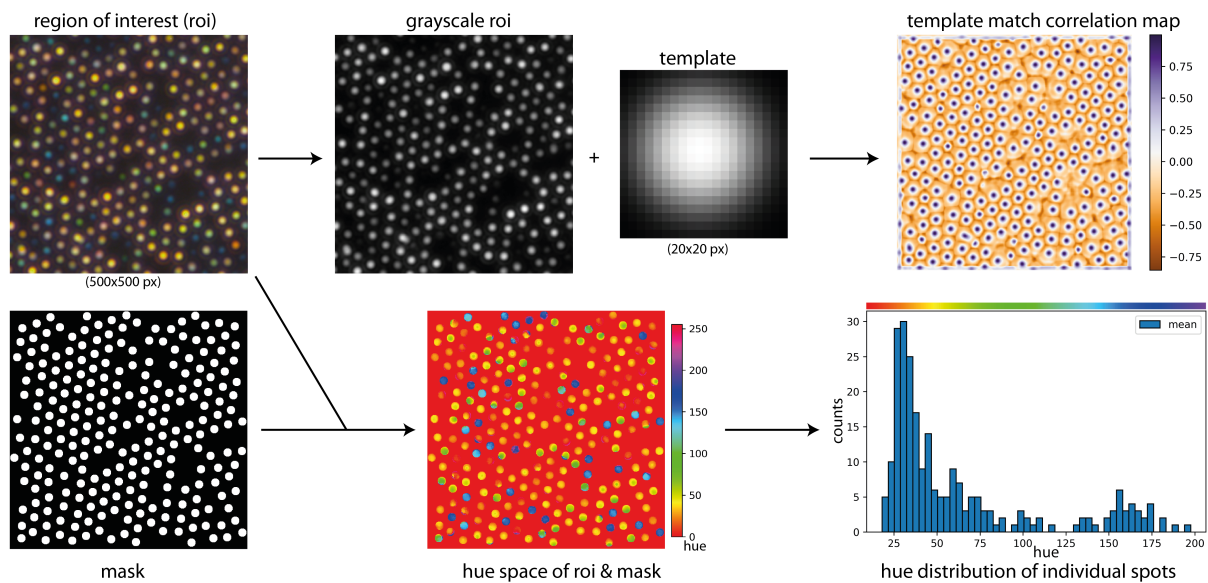


Figure 7.2.: This figure shows the image processing pipeline to get the distribution of colors (or hues) for each individual colorful spot. Starting with a region of interest (ROI) with a size of 500x500 px, the image gets converted to grayscale and matched with a template of a dummy particle consisting of a circle with radius 7 px effected by a Gaussian blur. From the resulting correlation map, the position of the peaks are extracted. To get the hue of an image, the original ROI gets transferred from RGB to HSV, then splitting the channels and taking the first one. For each particle in the hue channel, a 20x20 px area around the x-y-coordinates of a particle's center is combined with a binary mask of the template, taking the mean of the measured hue values to obtain the mean hue of a particle. The mean hue for each particle is plotted in a histogram.

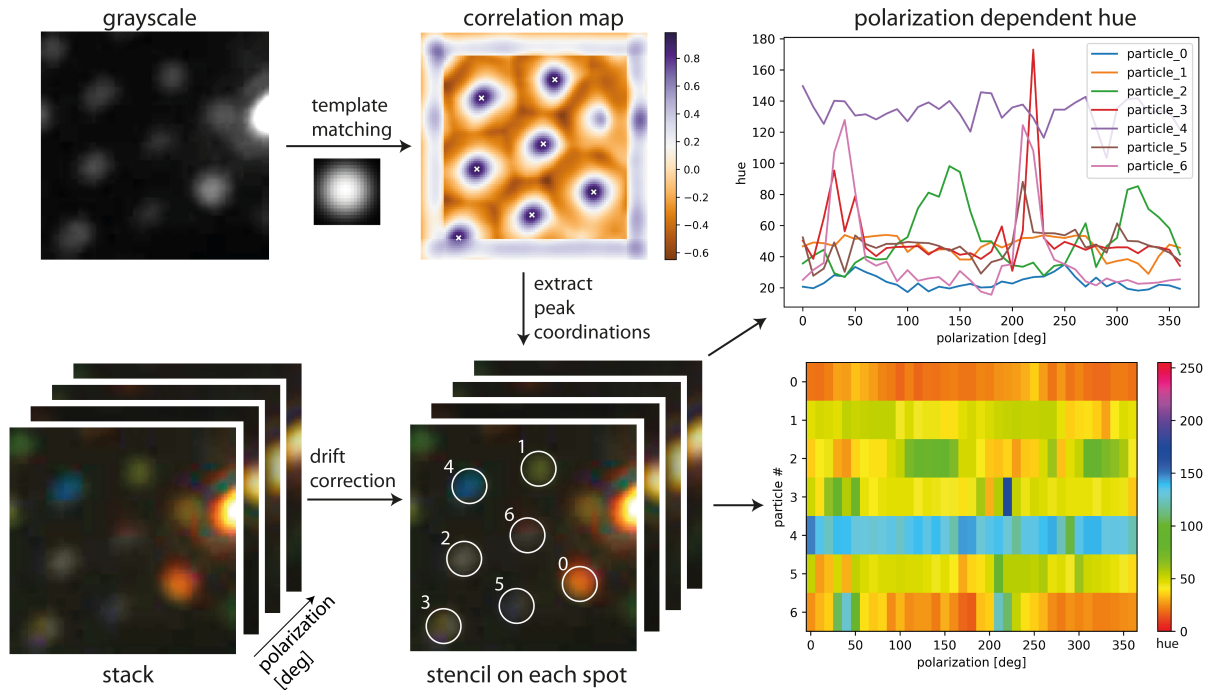


Figure 7.3.: This figure shows the video analysis pipeline exemplary on a video of DFM images displaying optical physical unclonable functions with varying angle of the polarization filter: A grayscale image of the first frame of the video is matched with a dummy particle to get a correlation map. The local peaks of this map give the location of the center of the particles. Applying a circular stencil at the localizations on a drift corrected video give the time dependent values for each particle. The mean hue of each particle is then plotted depending on the angle of the polarization filter as a line plot and as a heatmap, where 10° corresponds to 1 frame.

8. Conclusion and future directions

This thesis presented three projects, downsizing dynamic magnetic structures from the microscale to the nanoscale. The proof of concept study of magnetic nanorotors in chapter 6 magnetic nanorotor with the prospect of changing magnetic responses by varying the amounts of mNPs. The approach of combining highly magnetic nanoparticles with DNA origami opens endless possibilities in nanorobotics and fundamental research. In the following, some of the next possible steps are outlined.

The *magnetic nanorotors* can be used as a platform to investigate the interactions of the mNPs in more depth. Specifically, how many mNPs are needed to produce a torque strong enough to counter diffusion? This can be done by limiting the number of mNPs by controlling the number of bindings sites on the rotor, e.g. 5 binding sites (figure 8.1a). Changing the pivot point of the rotor to the middle of the structure and placing the particles in a row right above it should minimize potential deformations of the flexible DNA origami.

To fabricate *magnetic nanoswitches* [122], a cross-shape DNA origami, which was previously used for chiral plasmonic switches via strand displacement [75], was used as a template to hold mNPs and gold-silver nanorods. The polarized light emitted by the nanorods was monitored via DFM with incorporated polarizer and analyzed with the algorithm developed for the PUFs (section 7.2.2). A signal change occurring when applying a magnetic field was observed (figure 8.1b and appendix), but necessary quantification of

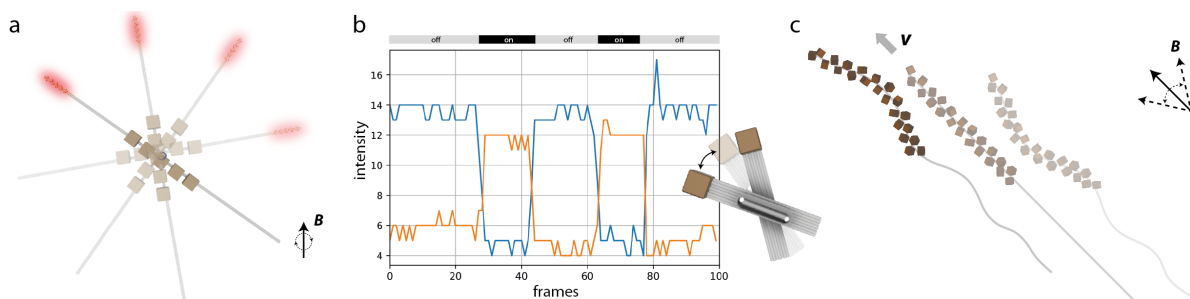


Figure 8.1.: **a** Schematic nanorotor with 5 mNPs and fluorescent dyes on one end. **b** Schematic of nanoswitch with data, on/off correspond to the application of an homogeneous magnetic field to the sample. **c** Schematic nanoswimmer design.

particle binding still has to be done.

Using a DNA origami appendages, e.g. 6HB dimers, covering only a portion of the bundles with mNPs could be an approach to realize the first *nanoswimmer* (figure 8.1c). In this architecture, the covered region would be actuated by a wagging magnetic field, whilst the naked region would act as a thrust generating flagella. By covering different portions of the bundles in different patterns and with different types of magnetic particles, actuation may be programmed for purpose. Moreover, by changing the bundle type (length and elasticity) the thrust generation of the device may be similarly adapted.

A. Appendix

A.1. Supporting Information for Publication P1

Programmable Design and Performance of Modular Magnetic
Microswimmers

Christoph Pauer, Olivia du Roure, Julien Heuvingh, Tim Liedl and Joe Tavaoli

published in

ADVANCED MATERIALS

Supporting Information

S1: Ex-vivo compatibility

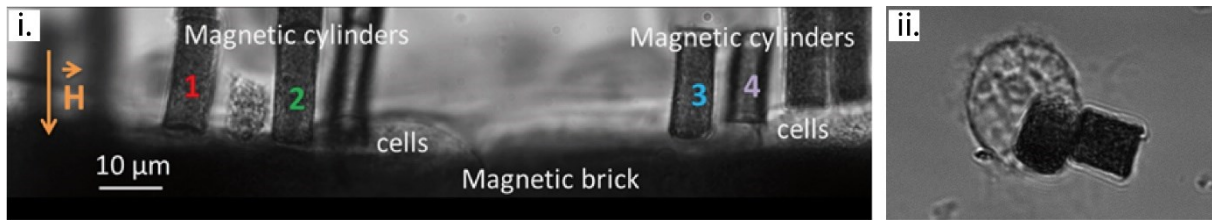


Figure S1: Micrographs demonstrating ex-vivo biocompatibility of our magnetic micromodules. i.) Magnetic modules being used to probe the mechanical properties of epithelial cells themselves deposited on a magnetic substrate of the same materials as the modules. ii.) The magnetic modules being ingested by a mouse dendritic cell. All biomaterials survived during the ~ 2 hour duration of experiments.

Refer to reference 40 in main text for stability of actin to the magnetic modules ([Sci Rep. 2017; 7: 15688](#). doi: [10.1038/s41598-017-15638-5](https://doi.org/10.1038/s41598-017-15638-5)).

S2: Estimation of magnetic susceptibility

To estimate the magnetic susceptibility of our modules, we compare the rotation dynamics of 2 cuboid modules of the same form but of different magnetic composition. One of these modules is packed full of superparamagnetic particles purchased from GE Healthcare ($d=400$ nm) and the other with particles purchased from Ademtech ($d=300$ nm). The former composition is used in this study and the volume susceptibility of modules consisting of the latter particles has been previously measured. ^(S2.1)

To initiate cuboid rotation a homogenous magnetic field, aligned perpendicular to the cuboids long axis, was applied. The resultant rotation dynamics was fitted to:

$$\tan \theta(t) = \tan \theta_0 \exp[-k(t - t_D)] \quad (1)$$

Where θ is the angle of the long axis of the cuboid with respect to the orientation of the applied magnetic field, θ_0 is the initial angle during the time interval before rotation, t_D , and k can be written as:

$$k = \frac{\chi^2}{(2+\chi)} \frac{\mu_0 g}{2\eta} D_{cub}^2 \left(\frac{H}{L_{cub}} \right)^2. \quad (2)$$

Here χ is the magnetic volume susceptibility, μ_0 is the vacuum permeability, g is a slowly varying function of aspect ratio, D_{cub} and L_{cub} are cuboid length and width, respectively and H the magnetic field strength. ^(S2.2) χ can then be extracted from fitting k after first obtaining g from the Ademtech cuboids with known magnetic susceptibility. All other constants are known and the fitting gives a susceptibility, $\chi \sim 0.8$, for the modules used in this study.

- S2.1 Tavacoli, J. *et al.*, The fabrication and directed self-assembly of micron-sized superparamagnetic non-spherical particles. *Soft Matter* **9**, 9103–9110 (2013).
- S2.2 Fresnais, J. *et al.*, Electrostatic Co-Assembly of Iron Oxide Nanoparticles and Polymers: Towards the Generation of Highly Persistent Superparamagnetic Nanorods. *Adv.Mater*, **20**, 3877 (2008)

S3: Robustness of assembly process

Histogram distributions show that in the worst-case scenario, pertaining to the S swimmer, ~65% of the devices form correctly to length. In the LT swimmer case, 100% of designs appear to form correctly. We note that such differences do not stem from errors in the assembly process but rather from random defects in the PDMS molds presumably carried over from the production of their SU8 resin templates. These defects lead to shallow or blocked microwells and therefore on occasion missing module pieces.

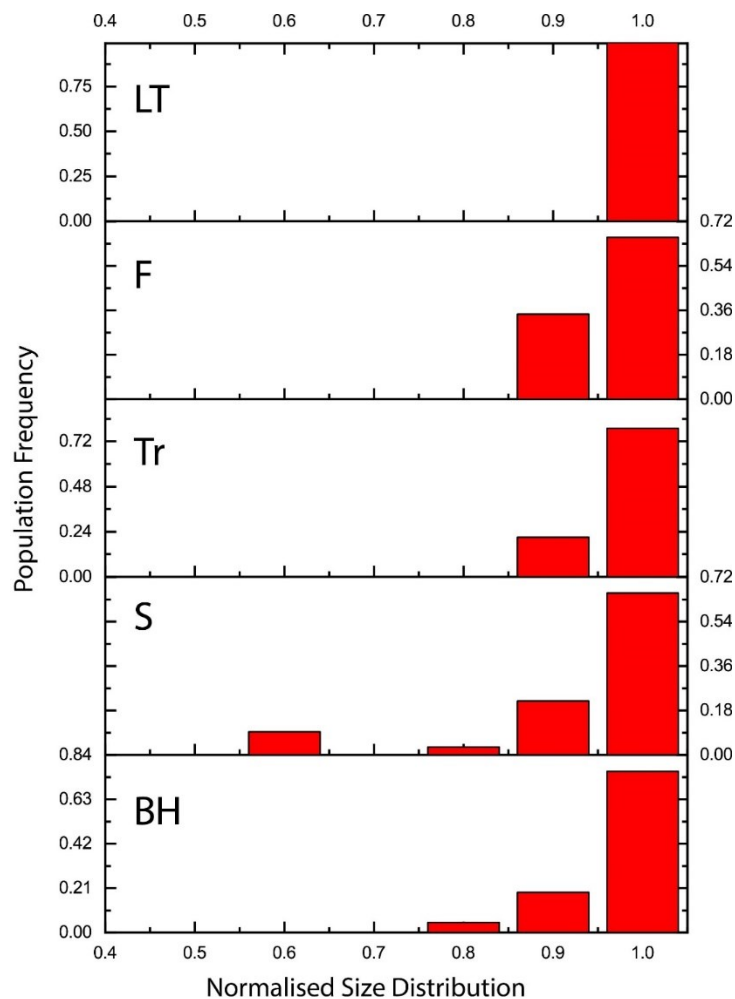


Figure S3: Histogram of the normalized size distribution of the swimmers. Normalization took place by dividing the length of formed swimmers with the longest swimmer measured containing all of its modules. The number of counts for the BH, S, Tr F and LT swimmers are 28, 19, 30, 45, and 38, respectively.

S4: Swimmer assembly with non-rotating modules

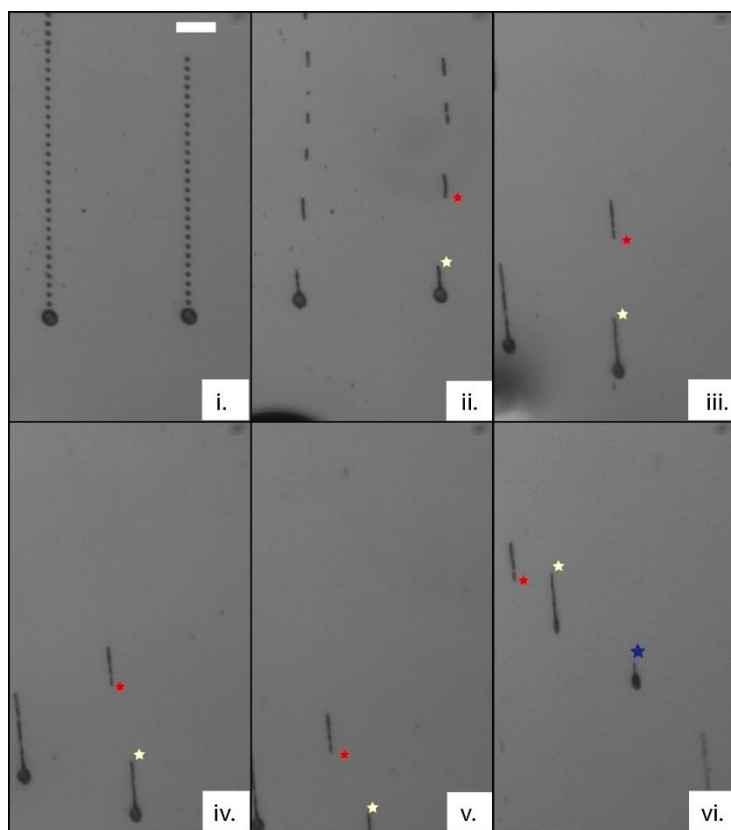


Figure S4: Modular arrangement and design initially intended for assembly into a HT swimmer. The design consists of circular tail modules that do not rotate. This leads to a rapid build of space between sections of the tail which reduces their magnetic interactions and assembly rate, resulting in a tendency for flow to disrupt their alignment and therefore full swimmer formation. For clarity, the endpoints of the non-connected tail sections are highlighted with stars. In frame vi. the field of view is shifted to capture the incomplete swimmer. The blue star highlights a further incomplete swimmer pushed into the field of view by flow.

The timings proceeding from i. to vi., after initiation of assembly, are 0 s, 33.2 s, 222.4 s, 307.8 s, 478.8 s and 517.2 s. A 25 mT homogenous magnetic field was applied and the scale bar is 20 microns.

S5: Swimmer connections

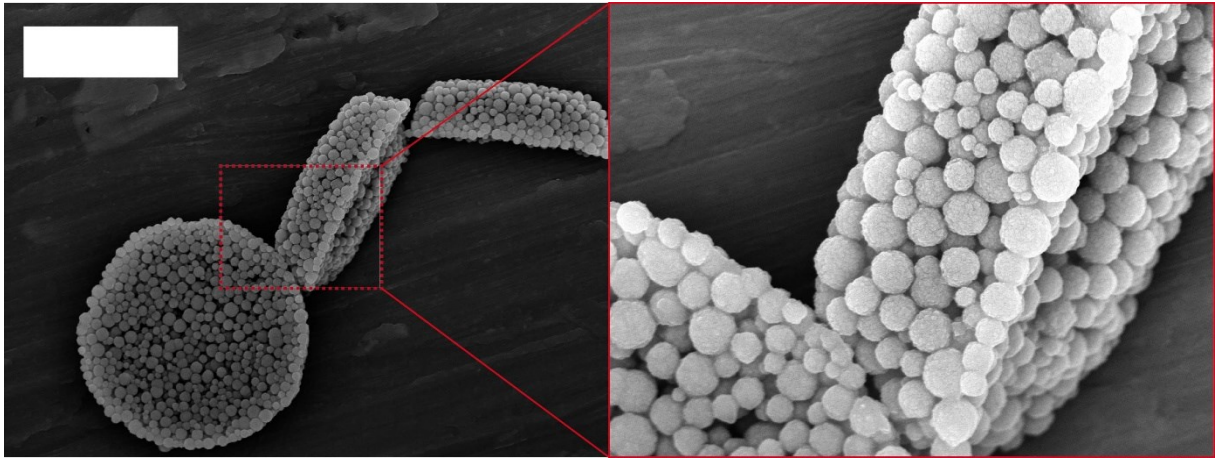


Figure S5: SEM micrographs showing direct connections between the magnetic modules. The scale bar is 5 microns.

S6: Swimmer breakdown

A proportion of the magnetic swimmers break down during swimming - especially at the lower end of frequencies where the beating amplitude is higher and flex significant. This is particularly true of the BH swimmer - possibly as this architecture (of the HT designs) imparts the most flex during a stroke and its tail modules are more attracted to the larger head module.

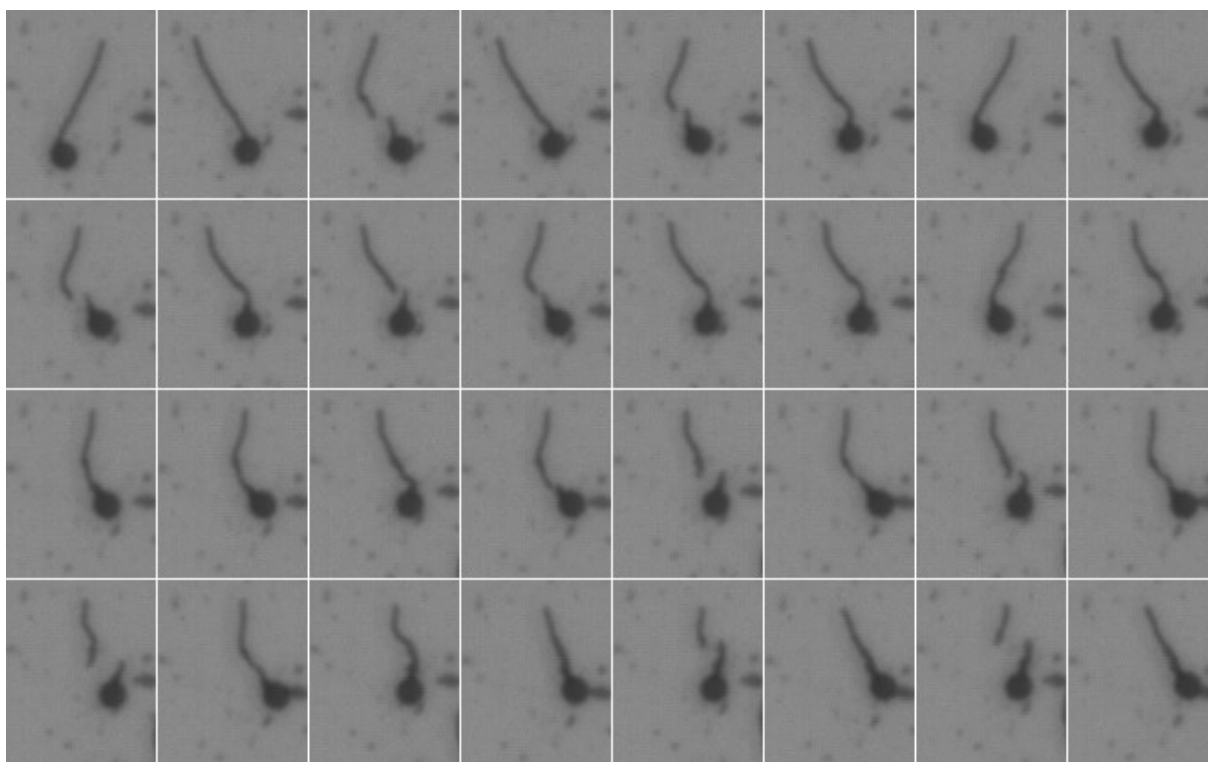


Figure S6. Break down of a HT swimmer at 10 Hz. The figure proceeds left to right then down and each frame is 0.15 seconds apart.

S7: Swimming at 19Hz

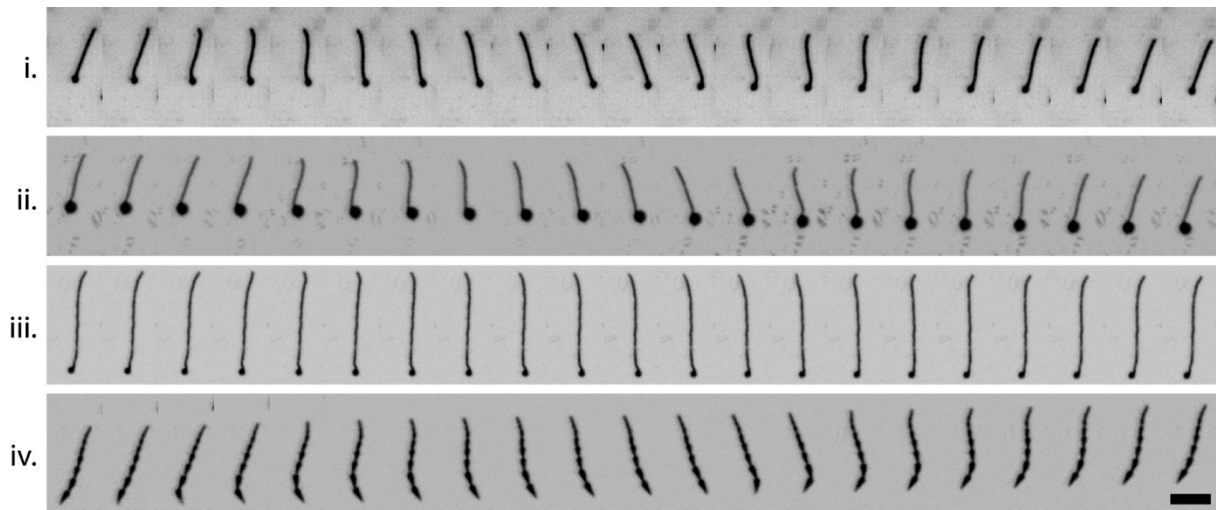


Figure S7. Full strokes of the S (i.), BH (ii.), LT (iii.) and Tr (iv.) swimmers at 19 Hz. Full actuation of the S, BH and Tr swimmers is evident while the LT swimmer performs only end wagging. The strokes were imaged by capturing a 19 Hz beating pattern at 20 fps stroke to produce aliasing. The aliasing produces the optical illusion of swimming in reverse in these captions. Scale bar is 50 microns.

S8: Angle correlations of Tr and BH swimmers during a half stroke

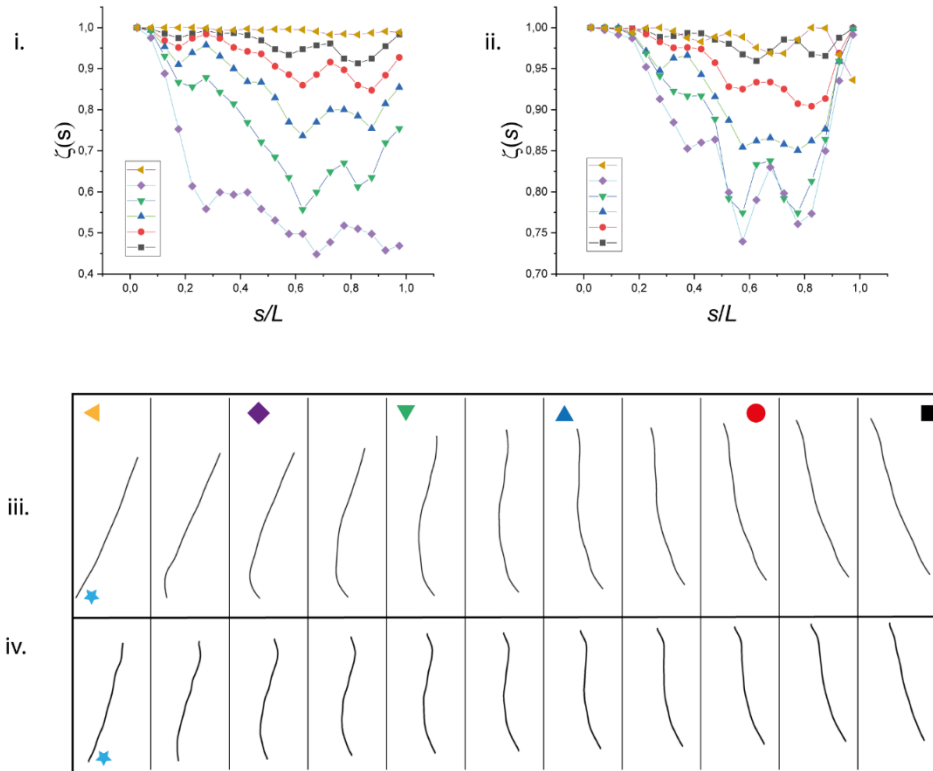


Figure S8. Angular-pair correlation function, $\zeta(s)$ of the Tr swimmer (i.) and the BH swimmer (ii.) over half a stroke. $\zeta = \cos(\theta_1 - \theta_s)$ where θ_1 is the angle at the front end of the swimmer during a stroke and θ_s is the corresponding angle a distance, s , along its tail length, L .

The plots in graphs i. and ii. correspond to skeletons of the swimmer configurations in montages iii. and iv., respectively, as highlighted with the colored symbols. The blue stars in the starting frame in iii. and iv. indicate the large-triangle end and the free end of the Tr swimmer and BH swimmer, respectively. The half stroke was imaged by capturing a 19 Hz beating pattern at 20 fps stroke to produce aliasing. The aliasing produces the optical illusion of swimming in reverse in these captions.

The lower values of $\zeta(s)$ reached by Tr swimmer indicate it has a larger beating amplitude at its front triangle than the HT swimmer obtains at its free end. In addition, the decorrelation of the Tr swimmer can extend across its length – especially evident at the start of the stroke (purple diamonds in figure) – showing beating is one sided and wave propagation one way. In contrast, the BH swimmer shows more two-sided beating across its stroke as reflected by a return to full correlation commencing from $s/L > 0.8$.

S9: Estimating $M_a^{1/2}$

To estimate $M_a^{1/2} = (\zeta_{\perp} \mu_0 \omega)^{1/2} L / a B \chi$ for the HT swimmers we use the known values of μ_0 , ω , L , B , χ , take a to be the half thickness of our module pieces and estimate ζ_{\perp} using $\zeta_{\perp} = \frac{2\pi\eta}{\log(L/a) - 1/2}$, the perpendicular drag coefficient for a prolate spheroid.^(S9.1) This has been shown to be close to the drag coefficient originating from a chain of spheres of the same aspect ratio.^(S9.2) Our case is still distinct due to the 2D nature of our modules but in the case of the HT swimmers: module depth \sim module width $\sim 2 \mu\text{m}$ and scaling with $V_r - M_a^{1/2}$ collapses their $V_y - f$ data points, suggesting a balance of viscous and magnetic forces dictates their stroke. The Tr and F swimmers incorporate different modular geometries than the HT designs which will, at the very least, change the form of their required perpendicular drag coefficient and also creates ambiguity of what value of a to use. In the absence of this information, and to aid discussion, we arbitrarily align their peak V_r values to the HT designs' peak at $M_a^{1/2} \sim 2$. This does not change the form of their $M_a - V_r$ signatures which is the key information used to understand the balance of elastic and magnetic forces acting on the swimmers, the information leveraged to optimize swimming velocity.

References

- S9.1 Cox, R. G., The motion of long slender bodies in a viscous fluid. Part I. General Theory. *Journal of Fluid Mechanics* **44**, 791-810 (1970)
- S9.2 Zahn, K., Lenke, R., and Maret, G., Friction coefficient of rod-like chains of spheres at very low Reynolds numbers. Part I. Experiment, *Journal de Physique II* **4**, 555-560 (1994) and Meunier, A., Friction coefficient of rod-like chains of spheres at very low Reynolds numbers. Part II. Numerical simulation, *Journal de Physique II* **4**, 561-564 (1994)

S10: Performance comparison of our swimmers to other leading micromotors

Ref.	$L_s/\mu\text{m}$	Micromotor Type	Locomotion Source	Directed locomotion (Yes/No)	$V/\mu\text{ms}^{-1}$	New fabrication concept?	Materials	POC application demonstrated?	Bio compatibility	Flocks (Y/N)
This work	~100	Synthetic Biomimetic. Self-assembled joints.	Magnetic field (actuation)	Y, magnetic field	~50	Y	Silica, Iron Oxide, ETPTA	N	Stable to cells and proteins (ex vivo)	Y
S10.1	~100	Synthetic Biomimetic Pre-engineered joints	Magnetic field (actuation)	Y, magnetic field	~30	N	Nickel photoresist	N	Not demonstrated	N
S10.2	~5	Synthetic Pre-engineered joints	magnetic field (actuation)	Y, magnetic field	~50	N	Gold Nickel Silver	N	Not demonstrated	N
S10.3	~100	Bio. Hybrid	Magnetic field (rotation)	Y, magnetic field	~50	N	Sperm Cell Iron Titanium Photoresis*	Y, in vitro directed drug delivery	Not demonstrated	N
S10.4	~100	Bio. Hybrid	Magnetic field (actuation)	Y, magnetic field	~50	Y	Sperm Cell Iron Oxide	Y, drug capture and release	Stable to cells (ex vivo)	N
S10.5	~20	Janus Particle	One sided Chemical reaction	N	-	N	Zinc Gelatin PEDOT Enteric polymer	Y, drug capture and triggered release (in vivo)	Y (in vivo)	Y
S10.6	~15.5	Synthetic Pre-engineered joints	magnetic field (actuation)	Y, magnetic field	Up to 15	Y	PPy Nickel PAH PSS	N	Not demonstrated	N
S10.7	~0.34	Nanobots	Enzymatic Catalysis	N	-	N	Silica MSNP APTES Urease	Y, drug capture and release (in vitro)	Y (in vitro)	Y
S10.8	~0.065	Janus Particle	One sided chemical reaction	N	-	N	MSNP Platinum	Y, cargo capture and release (in vitro)	Not demonstrated	Y
S10.9	1.4-2.6	Janus Particle	One sided chemical reaction	N	-	N	PLL Urease	Y, drug capture and release	Y (in vitro)	Y
S10.10	~50	Metallic Microtubes	Chemical reaction+ external magnetic field(for Fe)	Y	~275	N	Ti/Fe/Pt	Y, cargo transport	Not demonstrated	Y
S10.11	1.5-2.0	Microtubes	Acoustically driven	N	~50 (in water) ~10 (in blood)	N	Gold RBC PL	Y, detoxification	Y (in situ)	Y
S10.12	~11	Janus Nanotree	Phototaxis	Y, light controlled navigation	-	N	Silicon TiO2	N	Not demonstrated	N

L_s : Swimmer Length

V : Swimmer Velocity

MSNP: mesoporous silica nanoparticle

RBC: red blood cell membrane

PL: platelet membrane

References

- S10.1 *Magnetically Driven Undulatory Microswimmers, Integrating Multiple Rigid Segments*, *Small* 2019, 15, 1901197, <https://doi.org/10.1002/smll.201901197>
- S10.2 *Highly Efficient Freestyle Magnetic Nanoswimmer*, *Nano Lett.* 2017, 17, 8, 5092–5098, <https://doi.org/10.1021/acs.nanolett.7b02383>
- S10.3 *Sperm-Hybrid Micromotor for Targeted Drug Delivery*, *ACS Nano* 2018, 12, 327–337 <https://doi.org/10.1021/acsnano.7b06398>
- S10.4 *IRONsperm: Sperm-templated soft magnetic microrobots*, *Science Advances* 2020: 6, 28, eaba5855 <https://doi.org/10.1126/sciadv.aba5855>
- S10.5 *Multicompartment Tubular Micromotors Toward Enhanced Localized Active Delivery*, *Adv. Mater.* 2020, 32, 2000091 <https://doi.org/10.1002/adma.202000091>
- S10.6 *Undulatory Locomotion of Magnetic Multilink Nanoswimmers*, *Nano Lett.* 2015, 15, 7, 4829–4833, <https://doi.org/10.1021/acs.nanolett.5b01981>
- S10.7 *Enzyme-Powered Nanobots Enhance Anticancer Drug Delivery*, S., *Adv. Funct. Mater.* 2018, 28, 1705086. <https://doi.org/10.1002/adfm.201705086>
- S10.8 *J. Am. Chem. Soc.* 2015, 137, 15, 4976–4979, <https://doi.org/10.1021/jacs.5b02700>
- S10.9 *Enzyme-powered Janus platelet cell robots for active and targeted drug delivery*, Tang et al., *Sci. Robot.* 5, eaba6137 (2020)
- S10.10 *Magnetic Control of Tubular Catalytic Microbots for the Transport, Assembly, and Delivery of Micro-objects*, *Adv. Funct. Mater.* 2010, 20, 2430–2435, DOI: 10.1002/adfm.200902376
- S10.11 *Hybrid biomembrane-functionalized nanorobots for concurrent removal of pathogenic bacteria and toxins*, Esteban-Fernández de Ávila et al., *Sci. Robot.* 3, eaat0485 (2018)
- S10.12 *Programmable artificial phototactic microswimmer*, *Nature Nanotech* 11, 1087–1092 (2016). <https://doi.org/10.1038/nnano.2016.187>

Movies

Movie 1: S swimmer stroke with frequency. Scale bar is 50 μm .

Movie 2: F-Swimmers at 36 Hz. Scale bar is 50 μm .

Movie 3: Population swimming and pattern formation (scale bar 200 μm)

Movie 4: Pair Swimming (i.=head-to-tail aggregation, ii.=side-by-side swimming, iii.=overtaking and iv. = snap aggregation, scale bar 100 μm)

All movies are played at 60 fps and were recorded at 20 fps.

A.2. Supporting Information for Publication P2

Propulsion of Magnetic Beads Asymmetrically Covered with DNA Origami Appendages

Christoph Pauer, Aron Venczel, Mihir Dass, Tim Liedl and Joe Tlavacoli

published in

ADVANCED MATERIALS TECHNOLOGIES

Supplementary Information

S1

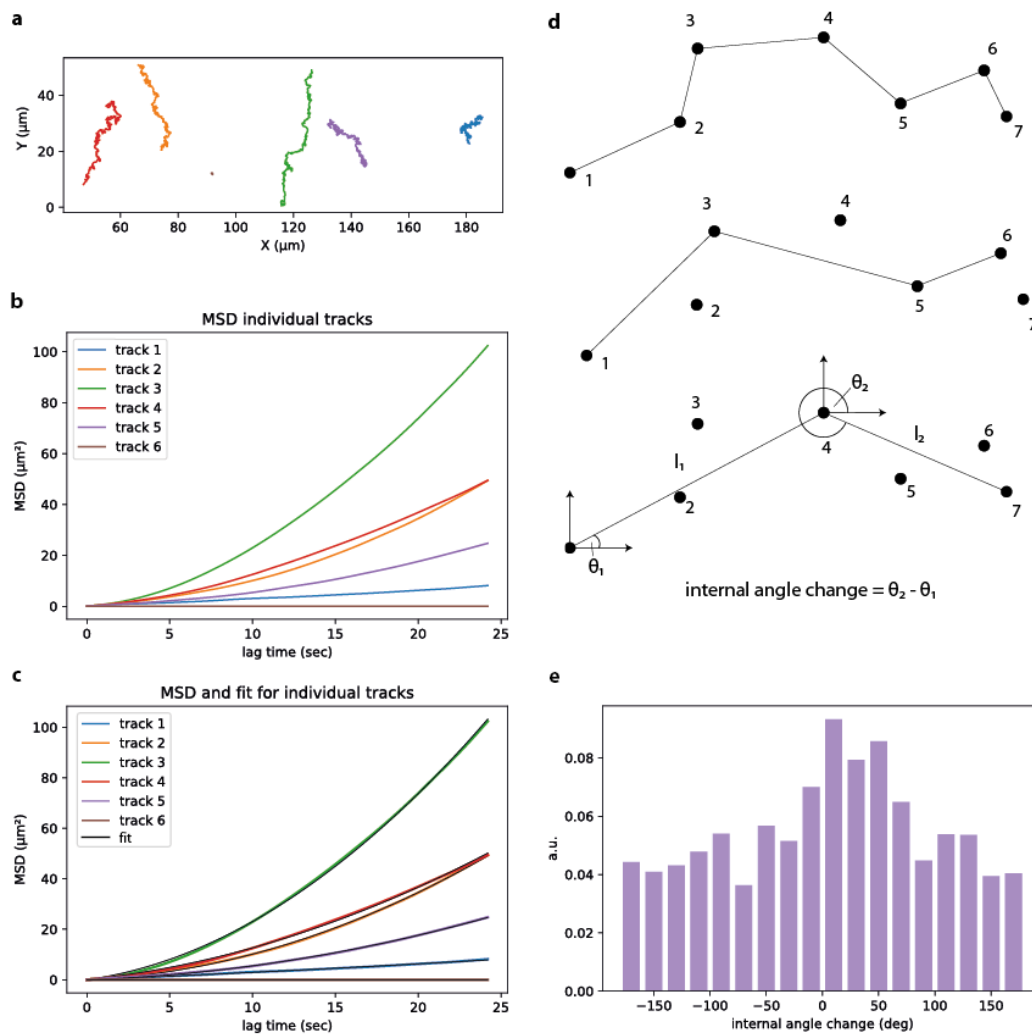


Figure S1: Description of the data analysis. **a** Tracks of the HC beads at 60 Hz over 123 seconds. **b** The mean square displacement (MSD) calculations based on the first 20% of the tracks in **a**. **c** The MSD curves fitted using the following relationship, $\langle r^2 \rangle = 4Dt + v^2t^2$ where D is the diffusion coefficient, v is velocity and t is the lag time. **d** A sketch illustrating the internal angle analysis method. The first case shows the track including every coordinate. The second includes every alternate location and the third includes every third location in the track. In our experiments, we had a frame rate of 5 fps. We included the location of the swimmer at every fifth frame, aiming for a step size of 1 second. We calculated the angle between the points and the global angle of the connecting lines. Subtracting the consecutive angles from each other gives the internal angle. **e** The histogram of the internal angle distribution, . The bins were weighted by averaging the two connecting lines (i.e. $(l_1 + l_2)/2$).

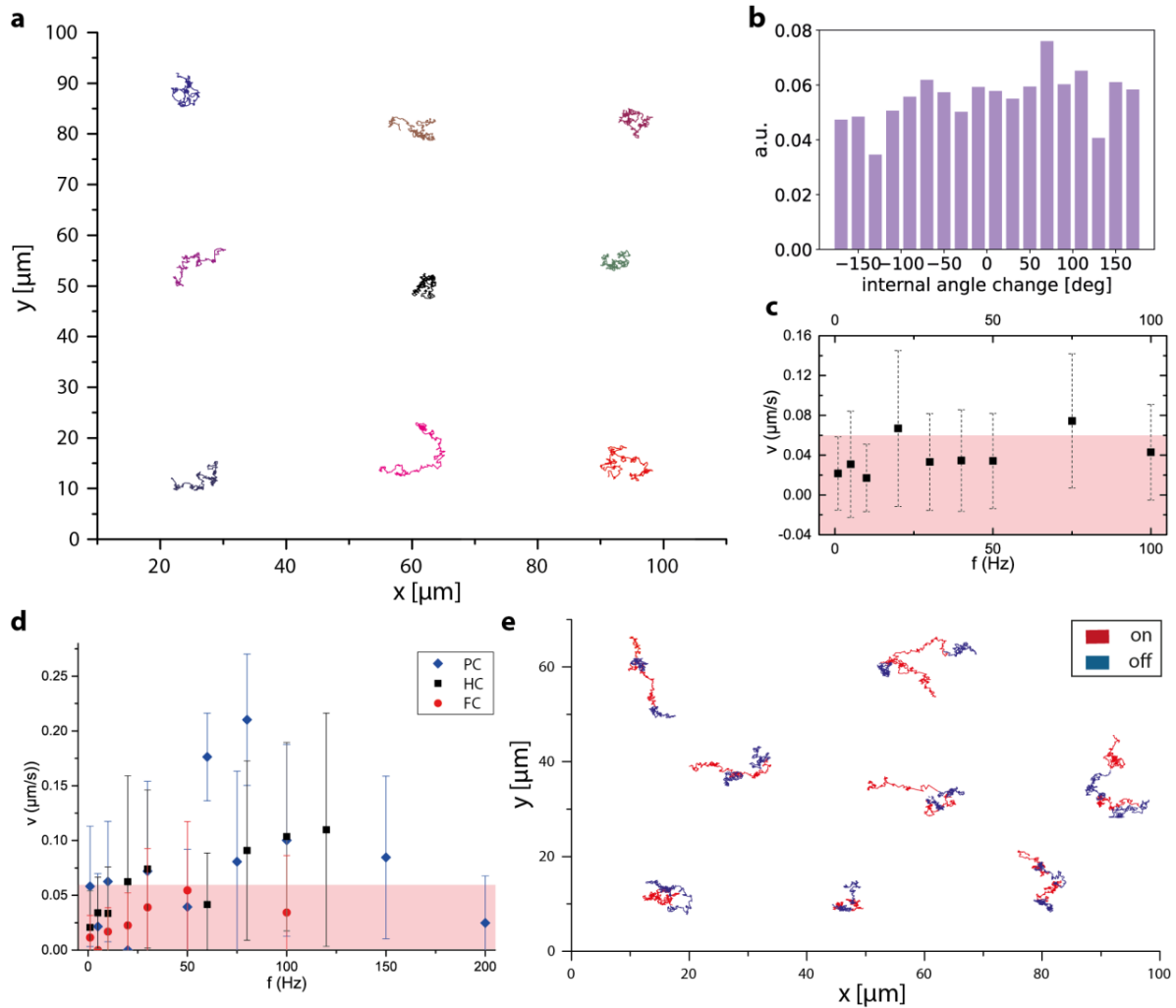


Figure S2: **a** The tracks for bare beads at 75 Hz. While at this frequency symmetry broken swimmers achieve velocities up to 500 nm/s, bare beads do not display any directionality in their movement. **b** The internal angle distribution of the tracks from **a** showing a flat distribution. **c** The velocity of the bare beads as a function of frequency. The red area depicts the range of velocities that can be attributed to drift. **d** The velocity of 6HB-monomer decorated beads as a function of frequency for different grafting methods. **e** On-off tracks for PC-monomer swimmers with a length of 40 seconds for each on/off interval. PC: Predominantly Covered beads; HC: Hemispherically Covered beads; FC: Fully Covered beads.

S3

The following equations are used to calculate the sperm number S_p [5]:

$$S_p = L \cdot \left(\frac{\xi_{\perp} \omega}{k} \right)^{\frac{1}{4}} \quad (1)$$

$$\xi_{\perp} = \frac{4\pi\eta}{\ln\left(\frac{L}{a}\right) + 0.193}$$

where k is the bending stiffness of the 6HB bundle ($k = 1.11 \cdot 10^{-26} \text{ Nm}^{-1}$ approximated by D. Turowski [1]), $\omega = 2\pi f$ with f being the applied frequency of the oscillating magnetic field, η is the viscosity, L is the length and a is the thickness of the 6HB bundle. Figure 3a shows the sperm number depending on the applied frequency of the oscillating magnetic field. The single digit values of the sperm number suggest that 6HB-monomer can support a bending wave associated with efficient swimming. The persistence length of 6HB designs as a function of the distance of crossovers, between 21bps and 42 bps, was reported to only differ by 10% in TAE based buffers [3], making the effect of the ‘fine-structure’ of the 6HB design negligible for the estimation of the Sperm number in this study. The velocity of idealized sperm-like swimmers locomoting because of a propagating sinusoidal wave ($y(x, t) = A \cdot \sin(kx - \omega t)$) is proportional to the square of the amplitude of the wave [3]. 3b shows the velocity of PC-dimer swimmers at 50 Hz depending on the field strength which is proportional to the amplitude of the oscillating field. With increasing field strength, the velocity increases monotonically, potentially quadratically, consistent with locomotion via a propagating wave.

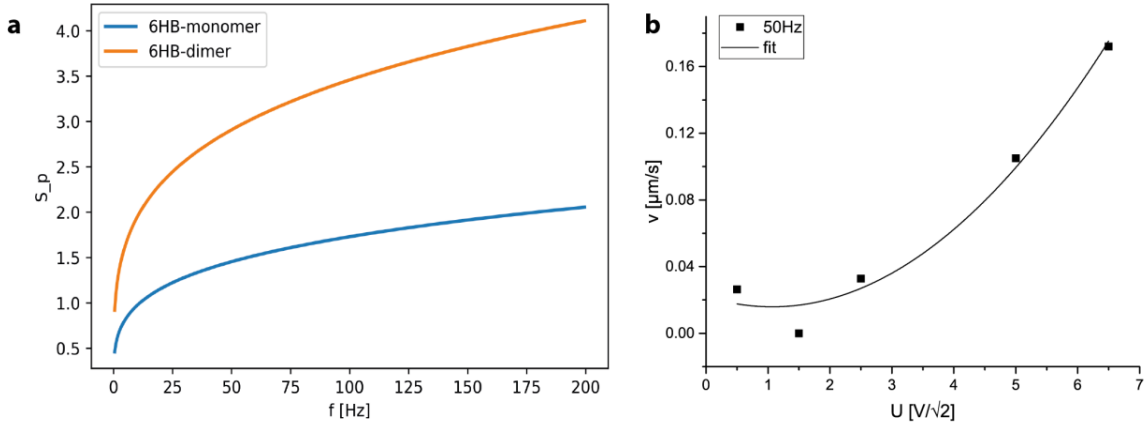


Figure S3: **a** The sperm number S_p as a factor of the frequency f calculated using Equation 1. **b** The velocity of the PC-dimer swimmer at a frequency of 50 Hz depending on the strength of the applied magnetic field.

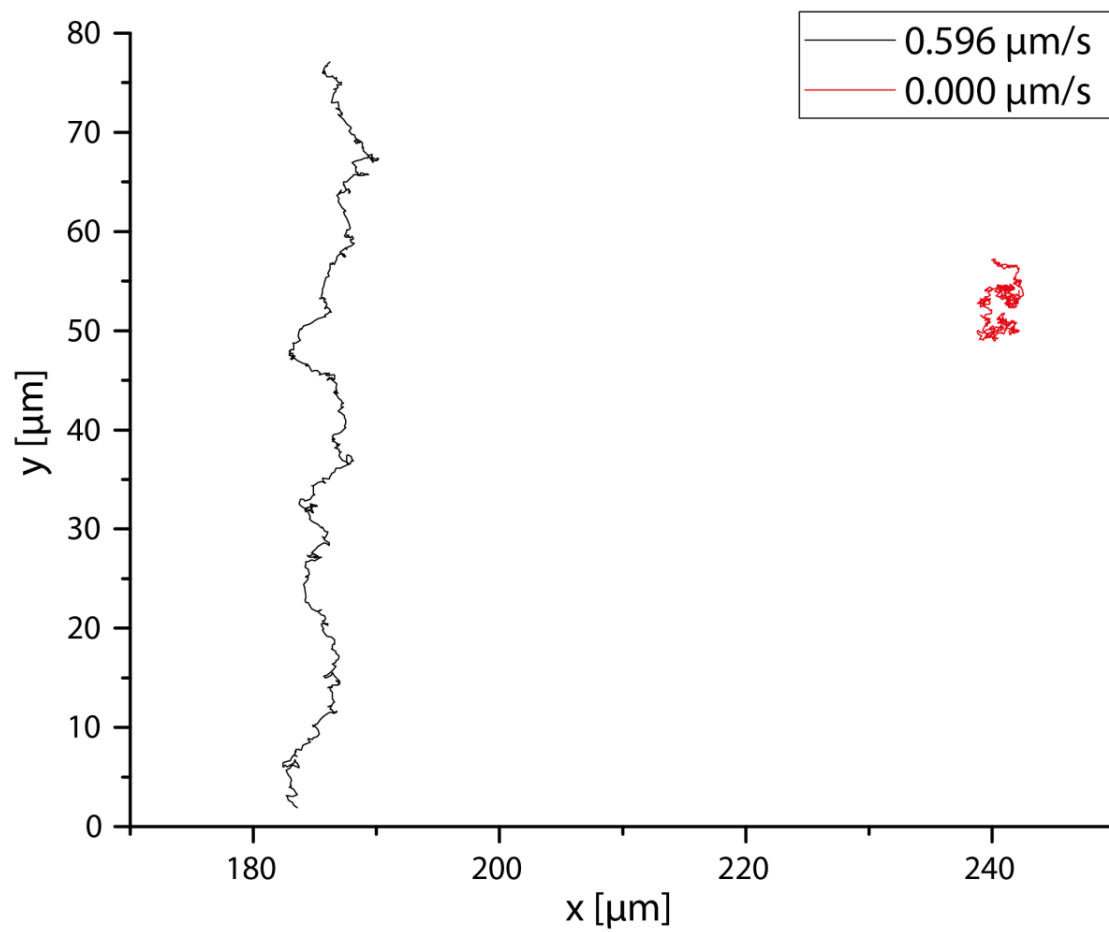


Figure S4: A comparison of the tracks of the fastest swimmer and a Brownian particle at 80 Hz.

S5

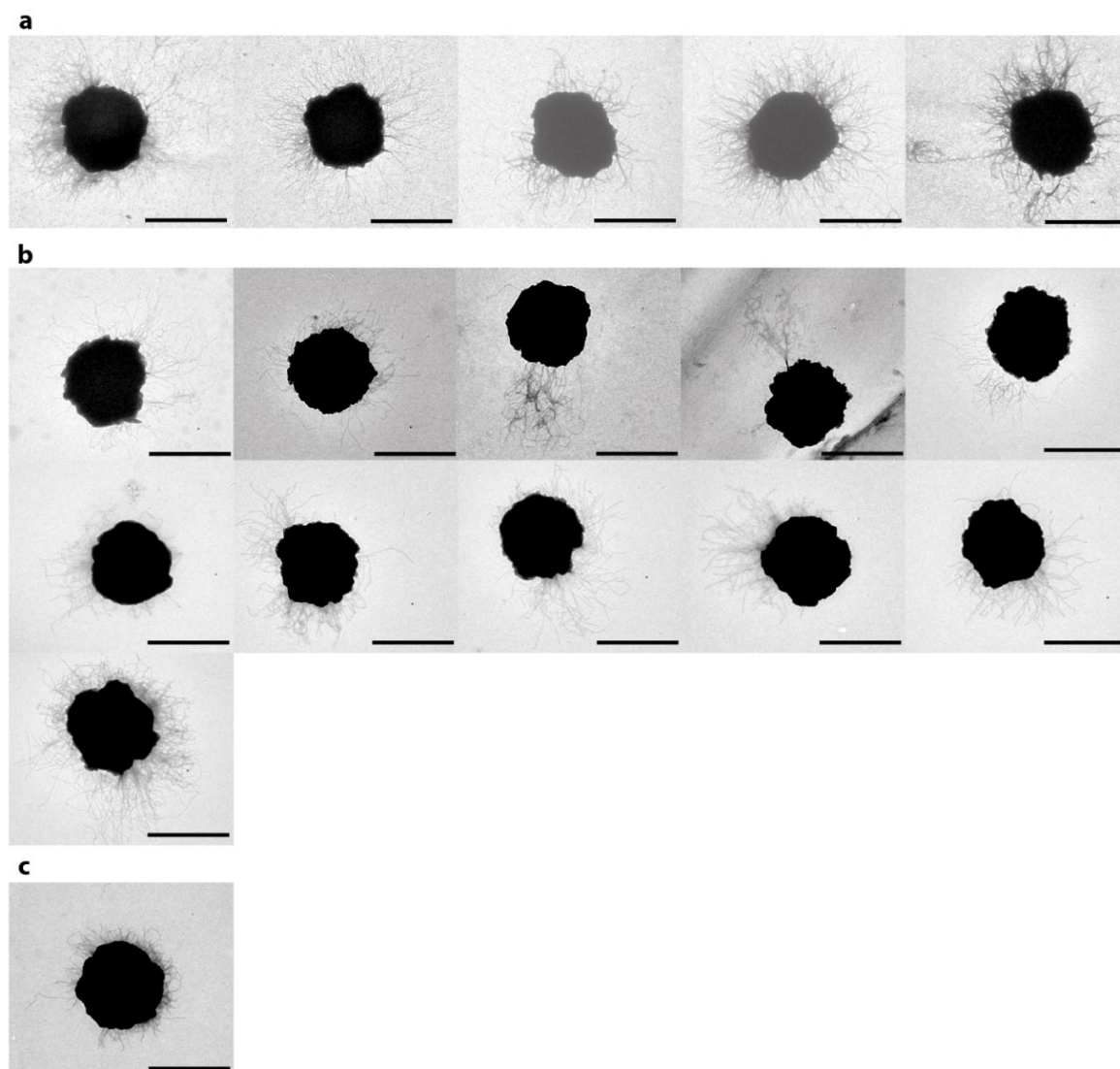


Figure S5: **a** TEM images of PC-dimer swimmers, **b** HC-dimer swimmers and **c** a HC-monomer swimmer. Scale bars are 1 μm .

S6

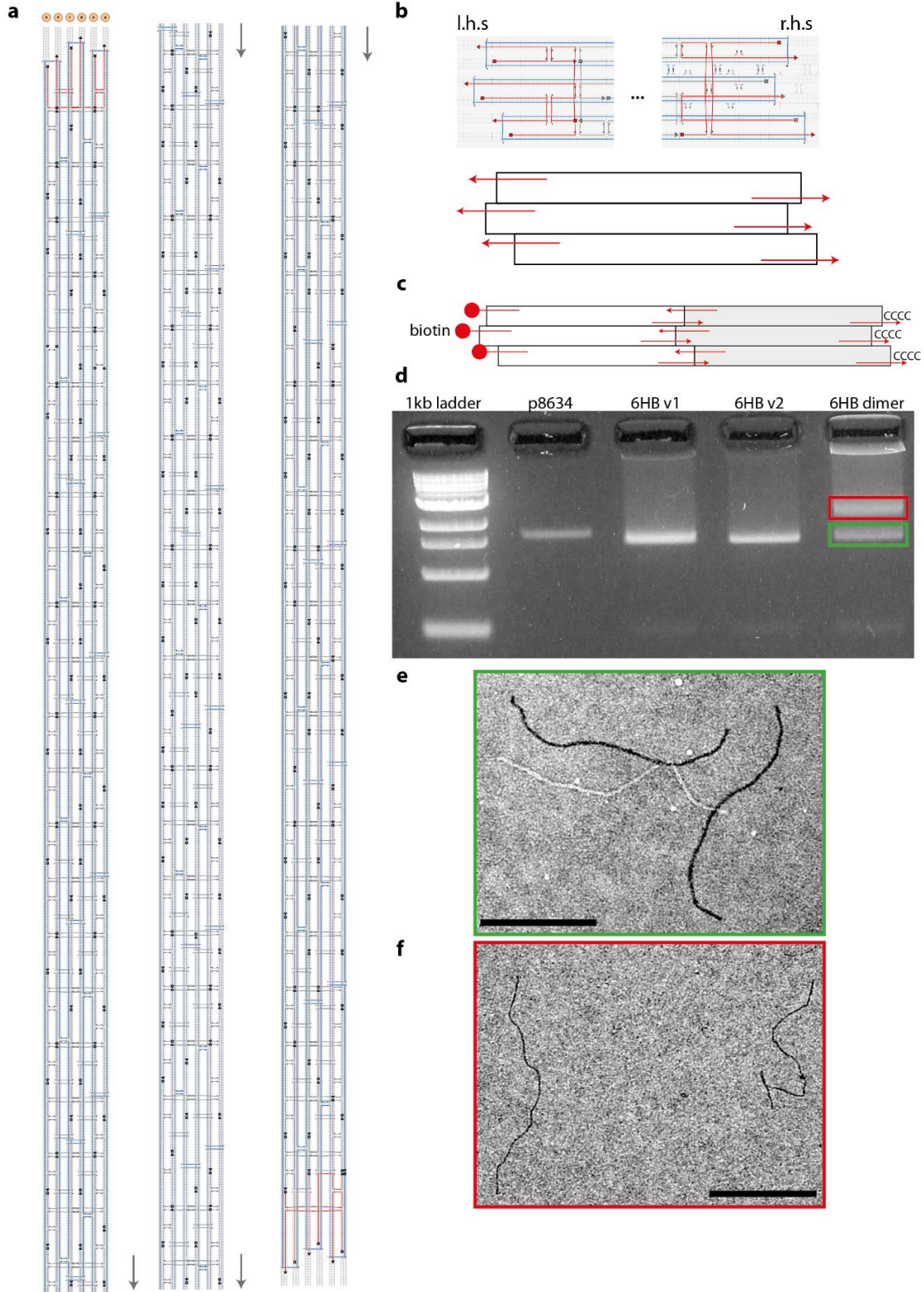


Figure S6: **a** Cadnano design with included cross section of the six-helix bundle. **b** (top) Expanded view of the left and right sides of the six-helix bundle. (bottom) a schematic of the 6HB. The red staples are exchanged depending on the purpose. To fabricate 6HB-dimers, two species of 6HB are folded. Monomer v1 (white in **c**) has biotin labeled staples sticking out of the left side (red dots), the right side has complementary intrusion ends to monomer v2 to form a dimer. Monomer v2 (grey in **c**) has the complementary intrusion ends to monomer v1 on its left site and C4-ends on the right site to prevent aggregation. **d** Gel electrophoresis analysis of the 6HB-monomers and dimers. The dimer sample is composed of 6HB v1 and v2. The 6HB-dimer lane shows two bands - the faster band composed of the remaining 6HB-monomers and a slower band with 6HB-dimers. Both the bands were excised and squeezed to extract the sample which was imaged using TEM. The TEM images are displayed on the right, 6HB-monomers (**e**) and -dimers (**f**). Scale bars are 500 nm for the dimers and 200 nm for the monomers.

The Cadnano file detailing or sequences are found in a separate file uploaded with the paper.

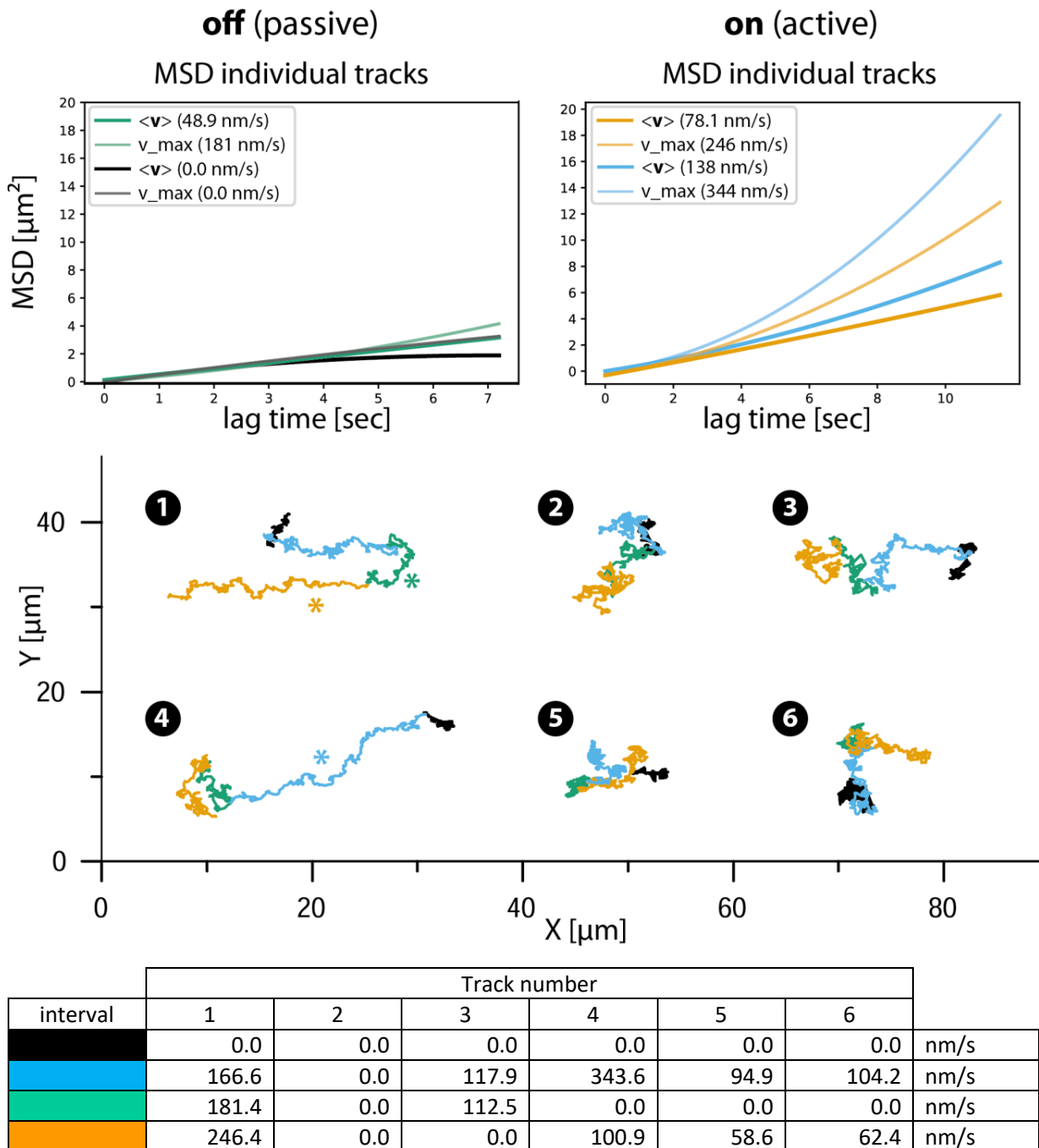


Figure S7: An in-depth analysis of Figure 3a (tracks of HC beads) from the main text. Each interval was separately analyzed. Displayed is the mean of their fitted MSD curves and the fitted MSD curve of the fastest velocity for each interval. The star marks the track interval with the fastest velocity. The individual velocities can be found in the table.

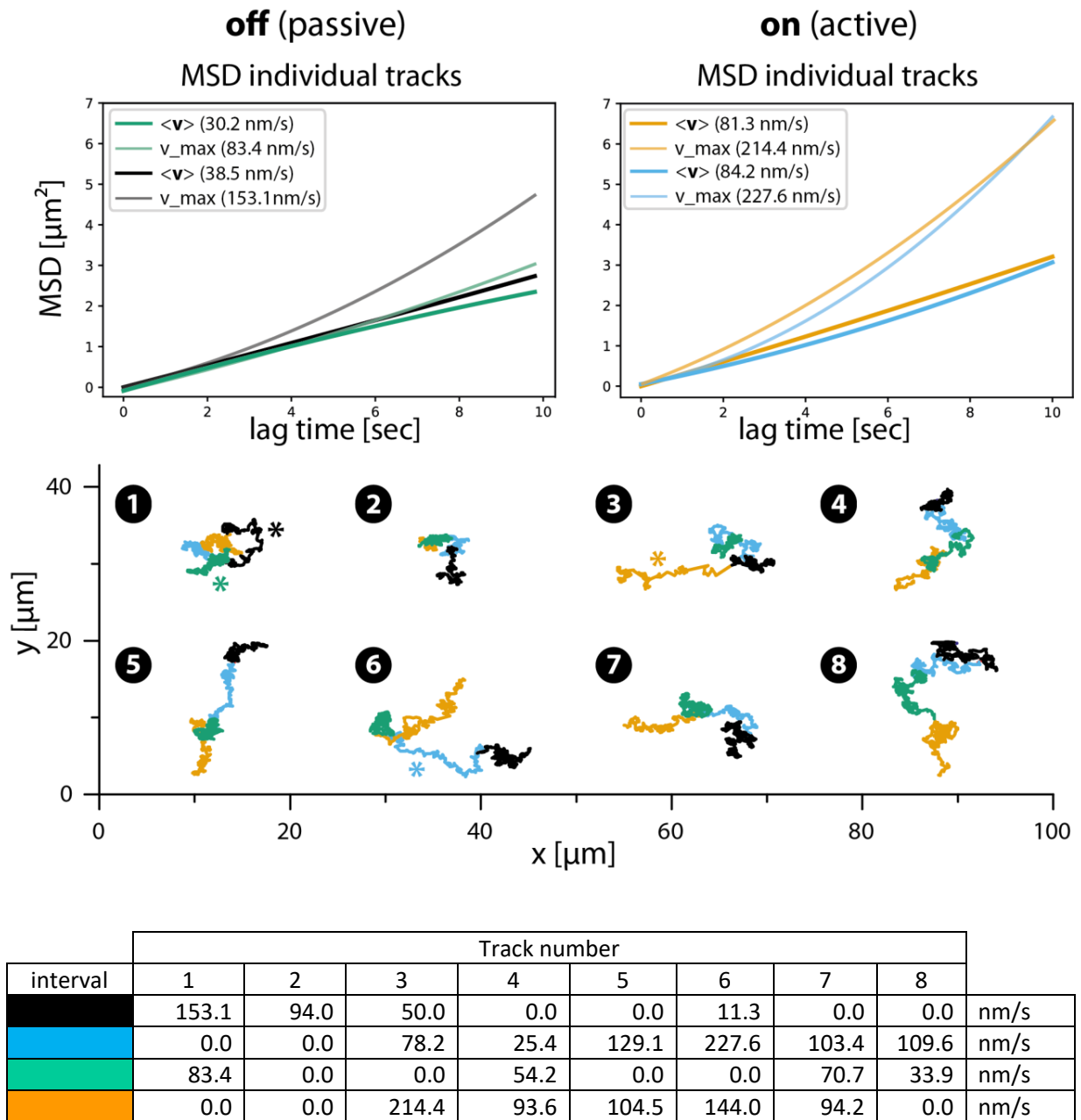


Figure S8: An in-depth analysis of Figure S2e (tracks of PC beads). Each interval was separately analyzed. Displayed is the mean of their fitted MSD curves and the fitted MSD curve of the fastest velocity for each interval. The star marks the track interval with the fastest velocity. The individual velocities can be found in the table. Each track lasted 60 seconds.

References

- [1] D. Turowski *An Investigation of Mechanical Properties of DNA Origami Nanostructures* Honors Thesis **2012**
- [2] Tony S. Yu, Eric Lauga and A. E. Hosoi *Experimental investigations of elastic tail propulsion at low Reynolds number* Phys. Fluids **2006**
- [3] Y. Xin, P. Piskunen, A. Suma, C. Li, H. Ijäs, S. Ojasalo, I. Seitz, M. A. Kostianen, G. Grundmeier, V. Linko and A. Keller *Environment-Dependent Stability and Mechanical Properties of DNA Origami Six-Helix Bundles with Different Crossovers Spacings* Small **2022**
- [4] J. Gray and G.J. Hancock *The Propulsion of Sea-Urchin Spermatozoa* J.Exp.Biol **1955**
- [5] Abbott, J. J., Peyer, K. E., Lagomarsino, M. C., Zhang, L., Dong, L., Kaliakatsos, I. K., & Nelson, B. J. *How should microrobots swim?* The international journal of Robotics Research **2009**

A.3. Protocols

Superparamagnetic particle dispersion

Mix the following chemicals in a 45 ml Falcon tube:

- 0.5 ml stock superparamagnetic particles from GE Healthcare (now available at Cytiva [98])
- 35 Methanol
- 5 ml distilled water
- 2 ml Ammonium (NH_3 , 27%)
- 0.08 ml 3-((Trimethoysilyl)propylmethacrylate

Rotate mixture slowly and continuously over night, then wash 4 times with Methanol:

- centrifuge dispersion at 3000 rcf for 25 min
- remove supernatant
- redisperse particles in 40 ml Methanol

Transfer dispersion into a smaller container, e.g. 2 ml Eppendorf tube, then:

- centrifuge dispersion at 8000 rcf for 10 min
- remove supernatant
- redisperse particles in 2 ml ETPTA
- repeat the 3 steps above 2x
- centrifuge dispersion at 8000 rcf for 10 min
- remove around 90% of the supernatant
- add 5% of the remaining volume photoinitiator and mix until a homogeneous solution is achieved

Casting superparamagnetic modules

A via e-beam lithography fabricated SU-8 waver serves as a mask to create a negative PDMS mold, by pouring the PDMS mixture (90% monomer, 10% crosslinker) over the SU-8 mask, remove any air bubbles by exposing it to a vacuum for 30 min and then dry the PDMS at 50°C over night in the oven. Then, carefully remove the mold to avoid damage on the waver. Clean the PDMS molds surface with sticky tape, then cast the desired modules by slowly dragging a droplet (15-20 μ l) of the superparamagnetic dispersion over it. Collect the excess dispersion for later usage and reticulate the casted module with a UV-lamp (254 nm) for 1 h.

Extracting superparamagnetic modules

Put a small droplet of PVP-VA on top of the hardened magnetic modules, turn mold upside down and gently place it on a glass slide. Heat the glass slide on a 200°C hotplate and gently press down the mold. After 10-30 seconds, when no bubbles are forming anymore, remove the glass slide from the hotplate and cool it down quickly by touching a metal or stone surface. Gently remove the PDMS mold, the magnetic modules remain stuck to the PVP-VA on the glass surface. That polymer can be dissolved (e.g. with ethanol) for magnetic experiments.

Heatramp for folding DNA origami

The folding program used is called OPTIMIDD and consists of the following steps:

1. 65°C for 15 min
2. Decrease temperature by 1°C every 5 min unit 59°C
3. Decrease temperature by 1°C every 45 min unit 39°C
4. Decrease temperature by 1°C every 30 min unit 36°C
5. Decrease temperature by 1°C every 5 min unit 20°C

Total time: 18 h 34 min

PEG surface modification

The protocol was taken from [80] and slightly adapted. It consists of a glass cleaning protocol followed by the PEG surface treatment. Starting with the glass cleaning:

A.3. Protocols

1. Place glass cover slips in a chemically inert rack inside a staining jar
2. Soak slide in 2 M NaOH for 20 min
3. Rinse with ddH₂O
4. Heat up 200 ml 2% Hellmanex III to 100°C, pour in staining jar and sonicate for 5 min
5. Rinse 3x with ddH₂O, fill up with ddH₂O and sonicate for 5 min
6. Dry in oven at 70°C for 5 min

Continuing with the silane-PEG-biotin modification:

1. Prepare 0.5% silane-PEG-biotin (SPB) ethanol mixture (around 40 μ l per 20x60 mm glass slide)
2. Add acetic acid (99%) to the mixture to achieve a 1% final concentration
3. Place first slide on a clean surface and add 40 μ l of the prepared SPB-solution
4. Immediately, place the next slide on top. Repeat that process until all slides are stacked up, then gently press down the stack to squeeze out remaining air bubbles
5. Incubate the stack for 30 min at 70°C in a dry oven
6. Place stack in a staining jar and sonicate it in ddH₂O for 5 min
7. Rinse it twice with ddH₂O
8. Separate slide and place them in a rack
9. Repeat step 7
10. Blow dry with N₂ and store the modified slides in a dark and dry place

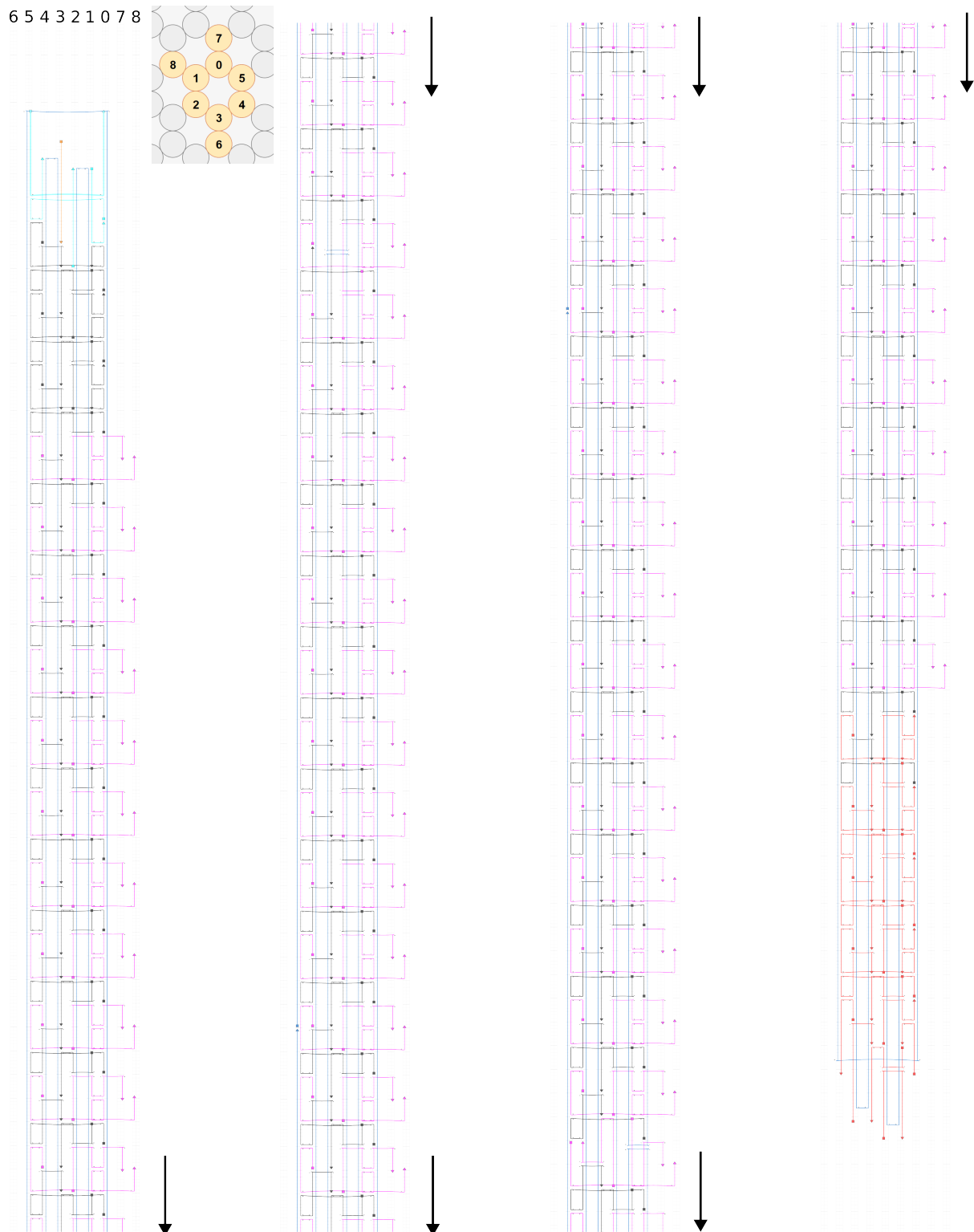


Figure A.1.: 6HB cadnano design with cross section and scaffold/staple routing, with scaffold (blue), AAAAAAAA-extensions to bind mNPs (fuchsia), TAAGTGAGACCCGTACATAT-extensions to bind dyes (red), biotin extension (orange), blunt end (turquoise) and core (black).

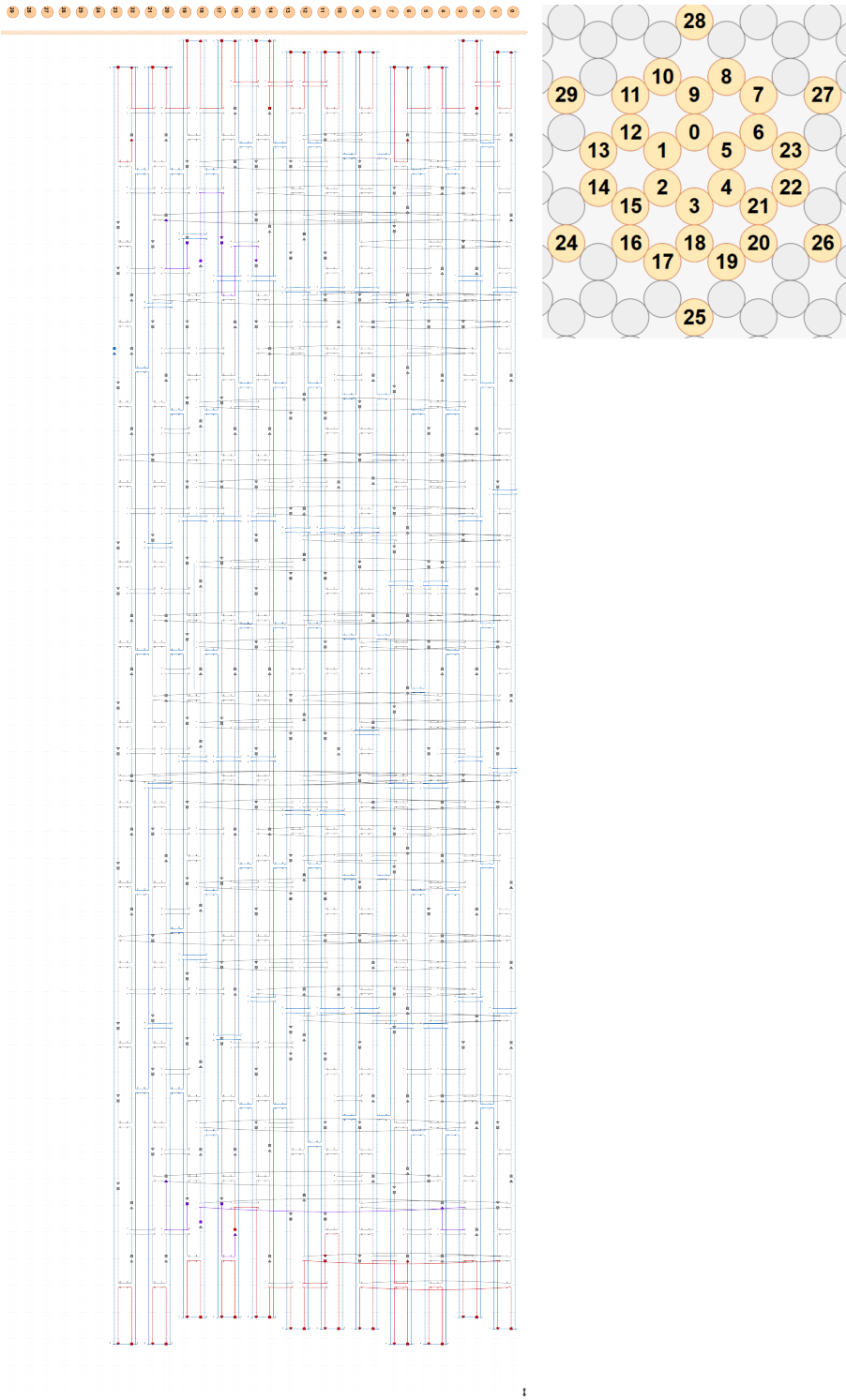


Figure A.2.: see next page for caption

A.4. Magnetic nanoswitch

Magnetic nanoswitches were fabricated on PEG modified glass surfaces as shown in figure A.3. The change in signal (figure A.3c-f) measured by DFM with a polarizer when applying a magnetic field to the nanoswitches indicate that indeed magnetic particles and gold-silver nanorods bound to the DNA origami crosses. It is still unclear whether the signal change originates from the expected behavior, shown in figure A.3b or if it originates from an aggregate of mNPs bound to the DNA origami cross. Necessary quantification by SEM for cross correlation could not be realized.

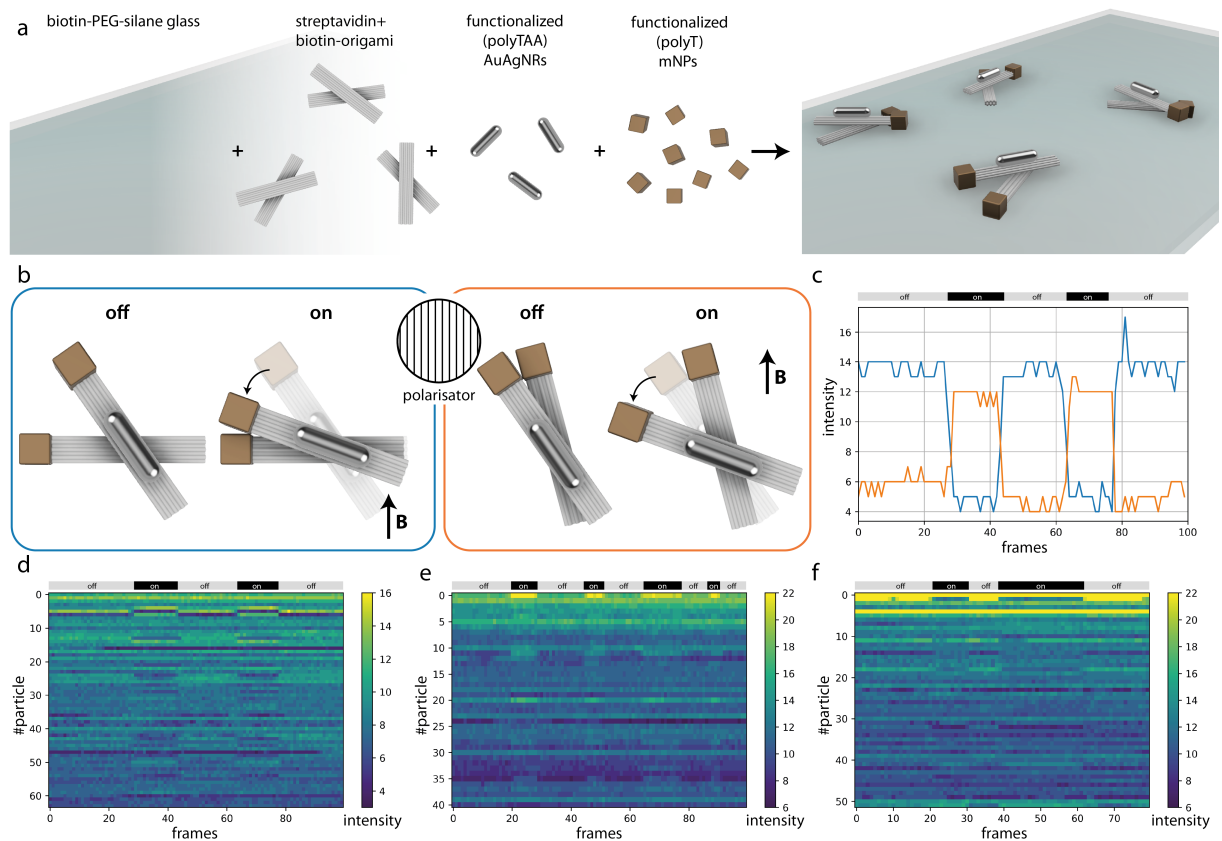


Figure A.3.: **a** shows schematically the production of the nanoswitches on surfaces. The individual components are sequentially added to a glass surface which surface is covered with a biotin-PEG-silane layer. The components are added in the following order: 1. the origami which has a streptavidin attached, 2. poly-TAA functionalized gold-silver nanorods (AuAgNRs), 3. poly-T functionalized magnetic nanoparticles (mNPs). **b** shows two possible orientations of the origami and their expected behaviour after applying an external magnetic field. The orientation of the nanorod with respect to the polarisator determines the intensity of the signal. **c** shows the behavior over time of two structures (which could be resembled by the ones shown in **b**) with switching the B-field off and on. **d-f** show the intensity traces for multiple particles, whereby **d**, **e** were different regions on the same sample and **f** is a different sample. (the length of 1 frame is equal to **c**, **d**: 750ms, **e**, **f**: 100ms)

Optimization of the image analysis algorithm

The algorithm explained in 7.2.1 is the second improved version of the algorithm. In table A.3 version 1 and version 2 of the algorithm are broken down and shown why version 2 is faster. In summary, extracting the x-y-coordinates of the particles before measuring their color parameters makes it possible to decrease the size of measured area to a minimum and thereby reducing computing time drastically. The given example in table A.3 , the computing time reduced from 15 minutes to 2-3 seconds for the same image.

	version 1	version 2
steps	<ul style="list-style-type: none"> - transform to grayscale - apply filters - transform to binary mask - get conncted components - for each component: create empty image, add the component to it and use it to measure parameters (x, y, HSV) 	<ul style="list-style-type: none"> - transform to grayscale - template matching - get x, y coordinates by extracting peaks from correlation map - for every particle: in a 20x20 px area around x, y measure HSV
speed dependencies	image size and number of particles	number of particles
major difference	creates a new full sized image for each particle	measures in a limited area around each particle, made possible by extracting the x, y coordinates beforehand
example:		
image size:	4096x2160 px	4096x2160 px
particles:	8000	8000
computing time:	15 min	2-3 sec

Table A.3.: Caption

A.5. Scripts

Functions used to process nanorotor data

```
1 import matplotlib.pyplot as plt
2 import numpy as np
3 import pandas as pd
4 from scipy.optimize import curve_fit
5
6
7 # Define a circle function
8 def circle(xy, xc, yc, r):
9     x, y = xy
10    return np.sqrt((x - xc)**2 + (y - yc)**2) - r
11
12 # Define a sinusoidal function
13 def sinusoidal_function(x, a, b, c, d):
14    return a * np.sin(b * x + c) + d
15
16
17 def fit_circle(df_data):
18    x_data, y_data = df_data['x'], df_data['y']
19    # Fit the circle to the scattered data
20    num_points = len(x_data)
21    initial_guess = (x_data.mean(), y_data.mean(), 1) # Initial guess
22    # for circle parameters (xc, yc, r)
23    popt, pcov = curve_fit(circle, (x_data, y_data), np.zeros(num_points),
24    p0=initial_guess)
25    return popt
26
27 def plot_circle(popt, df_data, ax):
28    x_data, y_data = df_data['x'], df_data['y']
29    # Extract the fitted circle parameters
30    x_circle_fit, y_circle_fit, r_fit = popt
31
32    # Plot the fitted circle
33    theta_fit = np.linspace(0, 2*np.pi, 360)
34    x_fit = x_circle_fit + r_fit * np.cos(theta_fit)
35    y_fit = y_circle_fit + r_fit * np.sin(theta_fit)
36    ax.plot(x_fit, y_fit, color='red', label='fitted circle')
37
38    # Plot circle center
```

```

37     ax.scatter(x_circle_fit, y_circle_fit, c='k', label='circle center',
38               marker='x')
39     ax.legend()
40     ax.axis('equal')
41
42 def polar_coords_cum_angle(df_data, x_y_circle_center):
43     x_data, y_data = df_data['x'], df_data['y']
44     xy_rel = np.empty([len(x_data), 2])
45     xy_rel[:,0], xy_rel[:,1] = x_data-x_y_circle_center[0] , y_data-
46     x_y_circle_center[1]
47     #polar coordinates:
48     r = np.sqrt(np.square(xy_rel[:,0]) + np.square(xy_rel[:,1]))
49     phi = np.arctan2(xy_rel[:,1], xy_rel[:,0])
50
51     corr_angles_diff=np.sign(np.sin(np.diff(phi)))*np.arccos(np.cos(np.
52     diff(phi)))
53     cum_angle=np.cumsum(corr_angles_diff)
54
55 return {'r':r, 'phi':phi, 'cum_angle':cum_angle}
56
57 def plot_pol_coord_and_cum_angle(r, phi, cum_angle):
58     fig, ax = plt.subplots(3,1)
59     ax[0].set_title('polar coordinates and cumulative angle')
60     ax[0].scatter(np.arange(len(r)), r, s=5)
61     ax[0].set_ylabel('r [px]')
62     ax[1].scatter(np.arange(len(phi)), phi, s=5)
63     ax[1].set_ylabel('phi [rad]')
64     ax[1].set_yticks([-np.pi, 0, np.pi])
65     ax[1].set_yticklabels(['-\u03C0', '0', '\u03C0'])
66     ax[2].set_xlabel('frames')
67     ax[2].plot(cum_angle)
68     ax[2].set_ylabel('cumulative \nangle [rad]')
69     plt.show()
70
71 def fit_sin(df_data, x_or_y='x' , exposure_time=10):
72     tt = df_data['frame']/(1000/exposure_time)
73     yy = df_data[x_or_y]
74
75     ff = np.fft.fftfreq(len(tt), (tt[1]-tt[0])) # assume uniform
76     spacing
77     Fyy = abs(np.fft.fft(yy))

```

```
75     guess_freq = abs(ff[np.argmax(Fyy[1:])+1]) # excluding the zero
76     frequency "peak", which is related to offset
77
78     # Fit the sinusoidal function to the scattered data
79     initial_guess = (np.sqrt(2)*yy.std(), 2*np.pi*guess_freq, 0, yy.mean
80     ()) # Initial guess for parameters (a, b, c, d)
81     try:
82         popt, pcov = curve_fit(sinusoidal_function, tt, yy, p0=
83         initial_guess)
84     except:
85         return {'omega':np.nan, 'phase':np.nan}
86
87     # Extract the fitted parameters
88     a, b, c, d = popt
89
90     return {'amplitude': a, 'omega':b, 'phase':c}
91
92 def all_freq_data(hdf5_files):
93
94     all_freq_data = {}
95
96     for file in hdf5_files:
97         file_name = file.split('\\')[1]
98
99         df_data = pd.read_hdf(file, key='locs')
100
101         freq_label = file_name.split('Hz')[0].split('ydir')[1].strip('_')
102     )
103
104     params = []
105     for i in df_data['group'].unique():
106         df = df_data[df_data['group'] == i]
107         x_y_center = fit_circle(df)[:2]
108         param = polar_coords_cum_angle(df, x_y_center)
109         params.append(param)
110     df_params = pd.DataFrame(params)
111
112     frqs = []
113     for i in df_data['group'].unique():
114         df = df_data[df_data['group'] == i][:2000]
115         popt = fit_circle(df)
```



```

114     params = polar_coords_cum_angle(df, popt[:2])
115
116     # Fit a linear regression line to cum angle
117     x_ca = np.arange(len(params['cum_angle']))
118     y_ca = params['cum_angle']
119
120     coefficients = np.polyfit(x_ca, y_ca, 1)
121
122     freq_phase_1 = fit_sin(df.reset_index(), 'x')
123     freq_phase_2 = fit_sin(df.reset_index(), 'y')
124     freq_phase = np.mean([freq_phase_1['omega'], freq_phase_2['
omega']])
125     frqs.append([    freq_phase,
126                   freq_phase_1['amplitude'],
127                   freq_phase_1['omega'],
128                   freq_phase_1['phase'],
129                   freq_phase_2['amplitude'],
130                   freq_phase_2['omega'],
131                   freq_phase_2['phase'],
132                   coefficients.round(5)[0],
133                   coefficients.round(5)[1],
134                   popt
135                   ])
136     df_frqs = pd.DataFrame(frqs, columns=['freq mean(x,y)', 'ampl_x',
', 'freq_x', 'phase_x', 'ampl_y', 'freq_y', 'phase_y', '
cum_angle_fit_a', 'cum_angle_b', 'circle_popt'])
137     df_frqs.loc[:, 'frq diff(x,y)'] = (df_frqs.loc[:, 'freq_x'] -
df_frqs.loc[:, 'freq_y']).abs()
138     df_frqs.loc[:, 'diff small'] = df_frqs.loc[:, 'frq diff(x,y)'] <
0.01*df_frqs.loc[:, 'freq mean(x,y)']
139
140     filtered_frqs = df_frqs.loc[(df_frqs.loc[:, 'cum_angle_fit_a'] >
0.0) & (df_frqs.loc[:, 'diff small'] == True), :].copy()
141
142     if '45_per_suc' in file_name:
143         freq_label = float(freq_label.replace('_', '.'))*12.5
144         filtered_frqs.loc[:, 'freq'] = filtered_frqs.loc[:, 'freq
mean(x,y)']/(2*np.pi)*12.5
145         all_freq_data[freq_label] = filtered_frqs
146     else:
147         freq_label = float(freq_label.replace('_', '.'))
148         filtered_frqs.loc[:, 'freq'] = filtered_frqs.loc[:, 'freq
mean(x,y)']/(2*np.pi)

```

```
149         all_freq_data[freq_label] = filtered_frqs
150
151     return all_freq_data
```

PUF image analysis

```
1 import imageio as io
2 import numpy as np
3 import pandas as pd
4 import cv2
5 from skimage import filters
6 from skimage.draw import disk
7 from skimage.feature import match_template, peak_local_max
8
9 #example file
10 file = 'example.tif'
11 img = io.v2.imread(file)
12
13 #calculate modes
14 def find_mode(arr):
15     freq = dict()
16     for i in arr:
17         if i in freq:
18             freq[i] += 1
19         else:
20             freq[i] = 1
21
22     _, mode = max(list(zip(freq.values(), freq.keys())))
23     return mode
24
25 #crop image to region of interest
26 roi = img[1000:1500, 1750:2250]
27 gray_roi = cv2.cvtColor(roi, cv2.COLOR_RGB2GRAY)
28 #take hue image
29 hue_roi, sat_roi, val_roi = cv2.split(cv2.cvtColor(roi, cv2.
    COLOR_RGB2HSV))
30
31 #draw circle
32 circle = np.zeros((20,20))
33 [rr,cc] = disk((9,9), 7)
34 circle[rr,cc] = 1
35 #use blurr to create a template
36 templ_cirlce = filters.gaussian(circle, sigma=3)
37 #match template
```

```

38 M = match_template(gray_roi, templ_cirlce, pad_input=True)
39 #find local peaks
40 peaks = peak_local_max(M, threshold_abs=0.9)
41
42 #measure
43 hues = np.empty_like(peaks[:,0]).astype('float64')
44 sats = np.empty_like(peaks[:,0]).astype('float64')
45 vals = np.empty_like(peaks[:,0]).astype('float64')
46 hue_modes = []
47 bw_grid = np.zeros(gray_roi.shape).astype('uint8')
48 #for each particle
49 for n in range(len(peaks[:,0])):
50     try:
51         bw_grid[peaks[n,0]-10:peaks[n,0]+10,peaks[n,1]-10:peaks[n,1]+10]
52         = (templ_cirlce > 0.2)*255
53         combined_h = hue_roi[peaks[n,0]-10:peaks[n,0]+10,peaks[n,1]-10:
54         peaks[n,1]+10] & (templ_cirlce > 0.2)*255
55         combined_s = sat_roi[peaks[n,0]-10:peaks[n,0]+10,peaks[n,1]-10:
56         peaks[n,1]+10] & (templ_cirlce > 0.2)*255
57         combined_v = val_roi[peaks[n,0]-10:peaks[n,0]+10,peaks[n,1]-10:
58         peaks[n,1]+10] & (templ_cirlce > 0.2)*255
59         #measure mean hue
60         hues[n] = combined_h[np.nonzero(combined_h)].sum()/np.size(
61         combined_h[np.nonzero(combined_h)])
62         sats[n] = combined_s[np.nonzero(combined_s)].sum()/np.size(
63         combined_s[np.nonzero(combined_s)])
64         vals[n] = combined_v[np.nonzero(combined_v)].sum()/np.size(
65         combined_v[np.nonzero(combined_v)])
66         hue_modes.append(find_mode(combined_h[np.nonzero(combined_h)]))
67         #print(hues[n])
68     except:
69         hues[n] = np.nan
70         sats[n] = np.nan
71         vals[n] = np.nan
72         hue_modes.append(np.nan)
73         pass
74
75 #write measurements in a dataframe
76 df_measurement = (pd.DataFrame(peaks, columns=['x', 'y'])
77 .join(pd.Series(hues, name='hues'))
78 .join(pd.Series(hue_modes, name='hue_modes'))
79 .join(pd.Series(sats, name='saturation')))

```

```
74     .join(pd.Series(vals, name='values'))
75
76 #save measurements as csv
77 #df_measurement.to_csv('measurement.csv')
```

PUF polarization analysis

```
1 import imageio as io
2 import matplotlib.pyplot as plt
3 import numpy as np
4 import cv2
5 from skimage import filters
6 from skimage.draw import disk
7 from skimage.feature import match_template, peak_local_max
8 from skimage.registration import phase_cross_correlation
9 from scipy.ndimage import shift
10
11 #read example file to a numpy array
12 file = 'example.avi'
13 stack = np.asarray(io.mimread(file))
14
15 #create grayscale and HSV stacks, split HSV channels
16 stack_gray = np.asarray([cv2.cvtColor(stack[i], cv2.COLOR_RGB2GRAY) for
17     i in range(stack.shape[0])])
18 stack_HSV = np.asarray([cv2.cvtColor(stack[i], cv2.COLOR_RGB2HSV) for i
19     in range(stack.shape[0])])
20 stack_hue = stack_HSV[..., 0]
21 stack_value = stack_HSV[..., 2]
22
23 #draw template
24 circle = np.zeros((20,20))
25 [rr,cc] = disk((9,9), 7)
26 circle[rr,cc] = 1
27 #use blurr to create a template
28 templ_cirlce = filters.gaussian(circle, sigma=3)
29
30 #template matching
31 fixed = match_template(stack_gray[0], templ_cirlce, pad_input=True)
32 dc_stack = []
33 lst_shift = np.zeros((stack_gray.shape[0],2))
34
35 #drift correction
36 for i in np.arange(stack_gray.shape[0]):
37     moving = match_template(stack_gray[i], templ_cirlce, pad_input=True)
```

```

36 shiftxy, _, _ = phase_cross_correlation(fixed > 0.7, moving > 0.7,
37 upsample_factor=10)
38
39 registered = np.empty_like(stack[0])
40 for n in range(3):
41     registered[:, :, n] = shift(stack[i, ..., n], shiftxy)
42     dc_stack.append(registered)
43
44 io.mimwrite('dc_stack.mp4', dc_stack, fps=30)
45
46 peaks = peak_local_max(fixed, threshold_abs=0.8)
47
48 activity = []
49 plt.figure()
50 plt.xlabel('frame')
51 plt.ylabel('hue')
52 for i, p in enumerate(peaks):
53     # Creating my extraction disk, my stencil
54     empty_im = np.zeros_like(fixed)
55     rr, cc = disk(p, 6, shape=fixed.shape)
56     empty_im[rr, cc] = 1
57
58     #Get the time trace of the data across px in my stencil
59     data = stack_value[:, empty_im.astype(bool)]
60
61     particle_activity = data.mean(1)
62     plt.plot(particle_activity, label=f'particle_{i}')
63
64     activity.append(particle_activity)
65 plt.legend()
66
67
68 activity = np.asarray(activity).astype('int')
69 plt.figure()
70 plt.imshow(activity, aspect='auto', cmap='hsv', vmin=0, vmax=180)
71 plt.xlabel('frame')
72 plt.ylabel('particle')
73
74 plt.colorbar(label='hue')

```


Bibliography

- [1] C. Pauer, O. Du Roure, J. Heuvingh, T. Liedl, and J. Tavecchi, “Programmable design and performance of modular magnetic microswimmers,” *Advanced Materials*, vol. 33, no. 16, 2021.
- [2] C. Pauer, A. Venczel, M. Dass, T. Liedl, and J. Tavecchi, “Propulsion of magnetic beads asymmetrically covered with dna origami appendages,” *Advanced Materials Technologies*, vol. 7, no. 12, 2022.
- [3] A. Lak, Y. Wang, P. J. Kolbeck, *et al.*, “Cooperative dynamics of dna-grafted magnetic nanoparticles optimize magnetic biosensing and coupling to dna origami,” *Nanoscale*, vol. 16, no. 15, 2024.
- [4] M. Dass, L. Raab, C. Pauer, *et al.*, “Self-assembled physical unclonable function labels based on plasmonic coupling,” *arXiv preprint arXiv:2310.19587*, 2023.
- [5] G. Junot, S. G. Leyva, C. Pauer, *et al.*, “Friction induces anisotropic propulsion in sliding magnetic microtriangles,” *Nano Letters*, vol. 22, no. 18, 2022.
- [6] J. Wang, *Nanomachines: fundamentals and applications*. John Wiley & Sons, 2013.
- [7] H. C. Berg, “The rotary motor of bacterial flagella,” *Annual review of biochemistry*, vol. 72, no. 1, 2003.
- [8] D. M. Phillips, “Comparative analysis of mammalian sperm motility,” *The Journal of cell biology*, vol. 53, no. 2, 1972.
- [9] S. J. Ebbens and J. R. Howse, “In pursuit of propulsion at the nanoscale,” *Soft Matter*, vol. 6, no. 4, 2010.
- [10] S. J. Ebbens and D. A. Gregory, “Catalytic janus colloids: Controlling trajectories of chemical microswimmers,” *Accounts of Chemical Research*, vol. 51, no. 9, Sep. 2018, ISSN: 0001-4842. DOI: 10.1021/acs.accounts.8b00243. [Online]. Available: <https://doi.org/10.1021/acs.accounts.8b00243>.

- [11] M. Miller, G. Prinz, S.-F. Cheng, and S. Bounnak, "Detection of a micron-sized magnetic sphere using a ring-shaped anisotropic magnetoresistance-based sensor: A model for a magnetoresistance-based biosensor," *Applied Physics Letters*, vol. 81, no. 12, 2002.
- [12] T. K. Jain, M. A. Morales, S. K. Sahoo, D. L. Leslie-Pelecky, and V. Labhasetwar, "Iron oxide nanoparticles for sustained delivery of anticancer agents," *Molecular pharmaceutics*, vol. 2, no. 3, 2005.
- [13] I. Chourpa, L. Douziech-Eyrolles, L. Ngaboni-Okassa, *et al.*, "Molecular composition of iron oxide nanoparticles, precursors for magnetic drug targeting, as characterized by confocal raman microspectroscopy," *Analyst*, vol. 130, no. 10, 2005.
- [14] M. Modo, M. Hoehn, and J. W. Bulte, "Cellular mr imaging," *Molecular imaging*, vol. 4, no. 3, 2005.
- [15] C. Burtea, S. Laurent, A. Roch, L. Vander Elst, and R. N. Muller, "C-malisa (cellular magnetic-linked immunosorbent assay), a new application of cellular elisa for mri," *Journal of inorganic biochemistry*, vol. 99, no. 5, 2005.
- [16] C. Liosis, A. Papadopoulou, E. Karvelas, T. E. Karakasidis, and I. E. Sarris, "Heavy metal adsorption using magnetic nanoparticles for water purification: A critical review," *Materials*, vol. 14, no. 24, 2021.
- [17] S. Chikazumi, *Physics of Magnetism*. Wiley, 1964.
- [18] K. H. J. Buschow, F. R. Boer, *et al.*, *Physics of magnetism and magnetic materials*. Springer, 2003, vol. 7.
- [19] U. Jeong, X. Teng, Y. Wang, H. Yang, and Y. Xia, "Superparamagnetic colloids: Controlled synthesis and niche applications," *Advanced Materials*, vol. 19, no. 1, 2007. DOI: <https://doi.org/10.1002/adma.200600674>.
- [20] M. A. M. Gijs, "Magnetic bead handling on-chip: New opportunities for analytical applications," *Microfluidics and Nanofluidics*, vol. 1, no. 1, Nov. 2004, ISSN: 1613-4990. DOI: 10.1007/s10404-004-0010-y. [Online]. Available: <https://doi.org/10.1007/s10404-004-0010-y>.
- [21] M. Kalubowilage, K. Janik, and S. H. Bossmann, "Magnetic nanomaterials for magnetically-aided drug delivery and hyperthermia," *Applied Sciences*, vol. 9, no. 14, 2019, ISSN: 2076-3417. DOI: 10.3390/app9142927. [Online]. Available: <https://www.mdpi.com/2076-3417/9/14/2927>.

-
- [22] P. Tierno, “Recent advances in anisotropic magnetic colloids: Realization, assembly and applications,” *Phys. Chem. Chem. Phys.*, vol. 16, 43 2014. DOI: 10.1039/C4CP03099K. [Online]. Available: <http://dx.doi.org/10.1039/C4CP03099K>.
- [23] J. W. Tavaoli, P. Bauër, M. Fermigier, D. Bartolo, J. Heuvingh, and O. Du Roure, “The fabrication and directed self-assembly of micron-sized superparamagnetic non-spherical particles,” *Soft Matter*, vol. 9, no. 38, 2013.
- [24] P. Tierno, J. Claret, F. Sagués, and A. Cēbers, “Overdamped dynamics of paramagnetic ellipsoids in a precessing magnetic field,” *Phys. Rev. E*, vol. 79, 2 Feb. 2009. DOI: 10.1103/PhysRevE.79.021501. [Online]. Available: <https://link.aps.org/doi/10.1103/PhysRevE.79.021501>.
- [25] X. Janssen, A. Schellekens, K. van Ommering, L. van IJzendoorn, and M. Prins, “Controlled torque on superparamagnetic beads for functional biosensors,” *Biosensors and Bioelectronics*, vol. 24, no. 7, 2009, ISSN: 0956-5663. DOI: <https://doi.org/10.1016/j.bios.2008.09.024>. [Online]. Available: <https://www.sciencedirect.com/science/article/pii/S0956566308005605>.
- [26] A. Tokarev, A. Aprelev, M. N. Zakharov, G. Korneva, Y. Gogotsi, and K. G. Kornev, “Multifunctional magnetic rotator for micro and nanorheological studies,” *Review of Scientific Instruments*, vol. 83, no. 6, Jun. 2012, ISSN: 0034-6748. DOI: 10.1063/1.4729795. [Online]. Available: <https://doi.org/10.1063/1.4729795>.
- [27] M. Doi, S. F. Edwards, and S. F. Edwards, *The theory of polymer dynamics*. oxford university press, 1988, vol. 73.
- [28] R. E. Cohen, D. Lide, and G. Trigg, *Physicist’s Desk Reference*. Springer Science & Business Media, 2003.
- [29] E. M. Purcell, “Life at low Reynolds number,” *American Journal of Physics*, vol. 45, no. 1, Jan. 1977, ISSN: 0002-9505. DOI: 10.1119/1.10903. [Online]. Available: <https://doi.org/10.1119/1.10903>.
- [30] J. Elgeti, R. G. Winkler, and G. Gompper, “Physics of microswimmers—single particle motion and collective behavior: A review,” *Reports on Progress in Physics*, vol. 78, no. 5, Apr. 2015. DOI: 10.1088/0034-4885/78/5/056601. [Online]. Available: <https://dx.doi.org/10.1088/0034-4885/78/5/056601>.
- [31] J. Happel and H. Brenner, *Low Reynolds number hydrodynamics: with special applications to particulate media*. Springer Science & Business Media, 2012, vol. 1.
- [32] J. E. Avron and O. Raz, “A geometric theory of swimming: Purcell’s swimmer and its symmetrized cousin,” *New Journal of Physics*, vol. 10, no. 6, 2008.

- [33] M. Lagomarsino, F. Capuani, and C. Lowe, “A simulation study of the dynamics of a driven filament in an aristotelian fluid,” *Journal of Theoretical Biology*, vol. 224, no. 2, 2003, ISSN: 0022-5193. DOI: [https://doi.org/10.1016/S0022-5193\(03\)00159-0](https://doi.org/10.1016/S0022-5193(03)00159-0). [Online]. Available: <https://www.sciencedirect.com/science/article/pii/S0022519303001590>.
- [34] C. H. Wiggins, D. Riveline, A. Ott, and R. E. Goldstein, “Trapping and wiggling: Elastohydrodynamics of driven microfilaments,” *Biophysical Journal*, vol. 74, no. 2, 1998, ISSN: 0006-3495. DOI: [https://doi.org/10.1016/S0006-3495\(98\)74029-9](https://doi.org/10.1016/S0006-3495(98)74029-9). [Online]. Available: <https://www.sciencedirect.com/science/article/pii/S0006349598740299>.
- [35] A. Babataheri, M. Roper, M. Fermigier, and O. Du Roure, “Tethered fleximags as artificial cilia,” *Journal of Fluid Mechanics*, vol. 678, 2011. DOI: 10.1017/S002211201100005X.
- [36] J. Hubbard and J. Beeby, “Collective motion in liquids,” *Journal of Physics C: Solid State Physics*, vol. 2, no. 3, 1969.
- [37] T. Vicsek and A. Zafeiris, “Collective motion,” *Physics reports*, vol. 517, no. 3-4, 2012.
- [38] H. Ceylan, I. C. Yasa, O. Yasa, A. F. Tabak, J. Giltinan, and M. Sitti, “3d-printed biodegradable microswimmer for theranostic cargo delivery and release,” *ACS nano*, vol. 13, no. 3, 2019.
- [39] W. Chen, Y. Wen, X. Fan, *et al.*, “Magnetically actuated intelligent hydrogel-based child-parent microrobots for targeted drug delivery,” *Journal of Materials Chemistry B*, vol. 9, no. 4, 2021.
- [40] L. Schwarz, D. D. Karausenko, F. Hebenstreit, R. Naumann, O. G. Schmidt, and M. Medina-Sánchez, “A rotating spiral micromotor for noninvasive zygote transfer,” *Advanced Science*, vol. 7, no. 18, 2020.
- [41] K. Villa, L. Krejčová, F. Novotný, Z. Heger, Z. Sofer, and M. Pumera, “Cooperative multifunctional self-propelled paramagnetic microrobots with chemical handles for cell manipulation and drug delivery,” *Advanced Functional Materials*, vol. 28, no. 43, 2018.
- [42] Z. Wu, J. Troll, H.-H. Jeong, *et al.*, “A swarm of slippery micropropellers penetrates the vitreous body of the eye,” *Science advances*, vol. 4, no. 11, 2018.

-
- [43] J. Vyskocil, C. C. Mayorga-Martinez, E. Jablonská, F. Novotny, T. Ruml, and M. Pumera, “Cancer cells microsurgery via asymmetric bent surface au/ag/ni micro-robotic scalpels through a transversal rotating magnetic field,” *ACS nano*, vol. 14, no. 7, 2020.
- [44] A. Ghosh and P. Fischer, “Controlled propulsion of artificial magnetic nanostructured propellers,” *Nano Letters*, vol. 9, no. 6, Jun. 2009, ISSN: 1530-6984. DOI: 10.1021/nl900186w. [Online]. Available: <https://doi.org/10.1021/nl900186w>.
- [45] L. Zhang, J. J. Abbott, L. Dong, B. E. Kratochvil, D. Bell, and B. J. Nelson, “Artificial bacterial flagella: Fabrication and magnetic control,” *Applied Physics Letters*, vol. 94, no. 6, Feb. 2009, ISSN: 0003-6951. DOI: 10.1063/1.3079655. [Online]. Available: <https://doi.org/10.1063/1.3079655>.
- [46] S. Tottori, L. Zhang, F. Qiu, K. K. Krawczyk, A. Franco-Obregón, and B. J. Nelson, “Magnetic helical micromachines: Fabrication, controlled swimming, and cargo transport,” *Advanced Materials*, vol. 24, no. 6, 2012. DOI: <https://doi.org/10.1002/adma.201103818>. [Online]. Available: <https://onlinelibrary.wiley.com/doi/abs/10.1002/adma.201103818>.
- [47] G. Salinas, K. Tieriekhov, P. Garrigue, N. Sojic, L. Bouffier, and A. Kuhn, “Lorentz Force-Driven Autonomous Janus Swimmers,” *Journal of the American Chemical Society*, vol. 143, no. 32, 2021. DOI: 10.1021/jacs.1c05589. [Online]. Available: <https://hal.science/hal-03451812>.
- [48] B. Dai, J. Wang, Z. Xiong, *et al.*, “Programmable artificial phototactic microswimmer,” *Nature Nanotechnology*, vol. 11, no. 12, Dec. 2016, ISSN: 1748-3395. DOI: 10.1038/nnano.2016.187. [Online]. Available: <https://doi.org/10.1038/nnano.2016.187>.
- [49] R. Dreyfus, J. Baudry, M. L. Roper, M. Fermigier, H. A. Stone, and J. Bibette, “Microscopic artificial swimmers,” *Nature*, vol. 437, no. 7060, Oct. 2005, ISSN: 1476-4687. DOI: 10.1038/nature04090. [Online]. Available: <https://doi.org/10.1038/nature04090>.
- [50] I. S. M. Khalil, H. C. Dijkslag, L. Abelmann, and S. Misra, “MagnetoSperm: A microrobot that navigates using weak magnetic fields,” *Applied Physics Letters*, vol. 104, no. 22, Jun. 2014, ISSN: 0003-6951. DOI: 10.1063/1.4880035. [Online]. Available: <https://doi.org/10.1063/1.4880035>.

- [51] C. Huang, Z. Lai, L. Zhang, X. Wu, and T. Xu, "A magnetically controlled soft miniature robotic fish with a flexible skeleton inspired by zebrafish," *Bioinspiration Biomimetics*, vol. 16, no. 6, Sep. 2021. DOI: 10.1088/1748-3190/ac23a9. [Online]. Available: <https://dx.doi.org/10.1088/1748-3190/ac23a9>.
- [52] B. J. Williams, S. V. Anand, J. Rajagopalan, and M. T. A. Saif, "A self-propelled biohybrid swimmer at low reynolds number," *Nature Communications*, vol. 5, no. 1, Jan. 2014, ISSN: 2041-1723. DOI: 10.1038/ncomms4081. [Online]. Available: <https://doi.org/10.1038/ncomms4081>.
- [53] W. Gao, S. Sattayasamitsathit, K. M. Manesh, D. Weihs, and J. Wang, "Magnetically powered flexible metal nanowire motors," *Journal of the American Chemical Society*, vol. 132, no. 41, Oct. 2010, ISSN: 0002-7863. DOI: 10.1021/ja1072349. [Online]. Available: <https://doi.org/10.1021/ja1072349>.
- [54] S. Palagi, A. G. Mark, S. Y. Reigh, *et al.*, "Structured light enables biomimetic swimming and versatile locomotion of photoresponsive soft microrobots," *Nature Materials*, vol. 15, no. 6, Jun. 2016, ISSN: 1476-4660. DOI: 10.1038/nmat4569. [Online]. Available: <https://doi.org/10.1038/nmat4569>.
- [55] P. J. Lu and D. A. Weitz, "Colloidal particles: Crystals, glasses, and gels," *Annu. Rev. Condens. Matter Phys.*, vol. 4, no. 1, 2013.
- [56] D. G. Aarts, M. Schmidt, and H. N. Lekkerkerker, "Direct visual observation of thermal capillary waves," *Science*, vol. 304, no. 5672, 2004.
- [57] J. N. Israelachvili, *Intermolecular and Surface Forces (Third Edition)*, Third Edition. San Diego: Academic Press, 2011. DOI: <https://doi.org/10.1016/B978-0-12-375182-9.10026-0>. [Online]. Available: <https://www.sciencedirect.com/science/article/pii/B9780123751829100260>.
- [58] B. Ninham, "On progress in forces since the dlvo theory," *Advances in Colloid and Interface Science*, vol. 83, no. 1, 1999, ISSN: 0001-8686. DOI: [https://doi.org/10.1016/S0001-8686\(99\)00008-1](https://doi.org/10.1016/S0001-8686(99)00008-1). [Online]. Available: <https://www.sciencedirect.com/science/article/pii/S0001868699000081>.
- [59] A. Travers and G. Muskhelishvili, "Dna structure and function," *The FEBS Journal*, vol. 282, no. 12, 2015. DOI: <https://doi.org/10.1111/febs.13307>. [Online]. Available: <https://febs.onlinelibrary.wiley.com/doi/abs/10.1111/febs.13307>.

- [60] J. D. WATSON and F. H. C. CRICK, “Molecular structure of nucleic acids: A structure for deoxyribose nucleic acid,” *Nature*, vol. 171, no. 4356, Apr. 1953, ISSN: 1476-4687. DOI: 10.1038/171737a0. [Online]. Available: <https://doi.org/10.1038/171737a0>.
- [61] S. Neidle *et al.*, *DNA structure and recognition*. IRL Press at Oxford University Press, 1994.
- [62] 17.05.2024. [Online]. Available: <https://www.rcsb.org/chemical-sketch>.
- [63] C. Bancroft, T. Bowler, B. Bloom, and C. T. Clelland, “Long-term storage of information in dna,” *Science*, vol. 293, no. 5536, 2001.
- [64] Y. K. Sunkari, T.-L. Nguyen, V. K. Siripuram, and M. Flajolet, “Impact of organic chemistry conditions on dna durability in the context of dna-encoded library technology,” *Iscience*, vol. 26, no. 9, 2023.
- [65] J. Chen and N. C. Seeman, “Synthesis from dna of a molecule with the connectivity of a cube,” *Nature*, vol. 350, no. 6319, 1991.
- [66] E. Winfree, F. Liu, L. A. Wenzler, and N. C. Seeman, “Design and self-assembly of two-dimensional dna crystals,” *Nature*, vol. 394, no. 6693, 1998.
- [67] W. Liu, H. Zhong, R. Wang, and N. C. Seeman, “Crystalline two-dimensional dna origami arrays,” *Angewandte Chemie (International ed. in English)*, vol. 50, no. 1, 2011.
- [68] J. Zheng, J. J. Birktoft, Y. Chen, *et al.*, “From molecular to macroscopic via the rational design of a self-assembled 3d dna crystal,” *Nature*, vol. 461, no. 7260, 2009.
- [69] P. W. Rothemund, “Scaffolded dna origami: From generalized multicrossovers to polygonal networks,” in *Nanotechnology: Science and Computation*, Springer, 2006.
- [70] 11.06.2024. [Online]. Available: <https://eu.idtdna.com/pages>.
- [71] 11.06.2024. [Online]. Available: <https://eurofinsgenomics.eu/de/>.
- [72] S. M. Douglas, H. Dietz, T. Liedl, B. Högberg, F. Graf, and W. M. Shih, “Self-assembly of dna into nanoscale three-dimensional shapes,” *Nature*, vol. 459, no. 7245, 2009.
- [73] P. C. Nickels, B. Wünsch, P. Holzmeister, *et al.*, “Molecular force spectroscopy with a dna origami-based nanoscopic force clamp,” *Science*, vol. 354, no. 6310, 2016.
- [74] K. F. Wagenbauer, C. Sigl, and H. Dietz, “Gigadalton-scale shape-programmable dna assemblies,” *Nature*, vol. 552, no. 7683, 2017.

- [75] A. Kuzyk, R. Schreiber, H. Zhang, A. O. Govorov, T. Liedl, and N. Liu, “Reconfigurable 3d plasmonic metamolecules,” *Nature materials*, vol. 13, no. 9, 2014.
- [76] G. Tikhomirov, P. Petersen, and L. Qian, “Fractal assembly of micrometre-scale dna origami arrays with arbitrary patterns,” *Nature*, vol. 552, no. 7683, 2017.
- [77] T. A. Meyer, C. Zhang, G. Bao, and Y. Ke, “Programmable assembly of iron oxide nanoparticles using dna origami,” *Nano letters*, vol. 20, no. 4, 2020.
- [78] C. Vietz, I. Kaminska, M. Sanz Paz, P. Tinnefeld, and G. P. Acuna, “Broadband fluorescence enhancement with self-assembled silver nanoparticle optical antennas,” *ACS nano*, vol. 11, no. 5, 2017.
- [79] G. Posnjak, X. Yin, P. Butler, *et al.*, “Diamond-lattice photonic crystals assembled from dna origami,” *Science*, vol. 384, no. 6697, 2024. DOI: 10.1126/science.ad12733. [Online]. Available: <https://www.science.org/doi/abs/10.1126/science.ad12733>.
- [80] E. Kopperger, J. List, S. Madhira, F. Rothfischer, D. C. Lamb, and F. C. Simmel, “A self-assembled nanoscale robotic arm controlled by electric fields,” *Science*, vol. 359, no. 6373, 2018.
- [81] A.-K. Pumm, W. Engelen, E. Kopperger, *et al.*, “A dna origami rotary ratchet motor,” *Nature*, vol. 607, no. 7919, 2022.
- [82] A. M. Maier, C. Weig, P. Oswald, E. Frey, P. Fischer, and T. Liedl, “Magnetic propulsion of microswimmers with dna-based flagellar bundles,” *Nano letters*, vol. 16, no. 2, 2016.
- [83] L. Kilwing, P. Lill, B. Nathwani, J. K. D. Singh, T. Liedl, and W. M. Shih, “Three-phase dna-origami stepper mechanism based on multi-leg interactions,” *Biophysical Journal*, vol. 121, no. 24, 2022.
- [84] A. Peil, L. Xin, S. Both, *et al.*, “Dna assembly of modular components into a rotary nanodevice,” *ACS nano*, vol. 16, no. 4, 2022.
- [85] T. Gerling, K. F. Wagenbauer, A. M. Neuner, and H. Dietz, “Dynamic dna devices and assemblies formed by shape-complementary, non-base pairing 3d components,” *Science*, vol. 347, no. 6229, 2015.
- [86] T. Liedl and F. C. Simmel, “Switching the conformation of a dna molecule with a chemical oscillator,” *Nano letters*, vol. 5, no. 10, 2005.

-
- [87] A. Kuzyk, Y. Yang, X. Duan, *et al.*, “A light-driven three-dimensional plasmonic nanosystem that translates molecular motion into reversible chiroptical function,” *Nature communications*, vol. 7, no. 1, 2016.
- [88] E. M. Willner, Y. Kamada, Y. Suzuki, *et al.*, “Single-molecule observation of the photoregulated conformational dynamics of dna origami nanoscissors,” *Angewandte Chemie International Edition*, vol. 56, no. 48, 2017.
- [89] Y. Klapper, N. Sinha, T. W. S. Ng, and D. Lubrich, “A rotational dna nanomotor driven by an externally controlled electric field,” *Small*, vol. 6, no. 1, 2010.
- [90] M. Vogt, M. Langecker, M. Gouder, *et al.*, “Storage of mechanical energy in dna nanorobotics using molecular torsion springs,” *Nature Physics*, vol. 19, no. 5, 2023.
- [91] M. Vogt, J. List, M. Langecker, I. Santiago, F. C. Simmel, and E. Kopperger, “Electrokinetic torque generation by dna nanorobotic arms studied via single-molecule fluctuation analysis,” *The Journal of Physical Chemistry B*, vol. 127, no. 50, 2023.
- [92] A. Büchl, E. Kopperger, M. Vogt, M. Langecker, F. C. Simmel, and J. List, “Energy landscapes of rotary dna origami devices determined by fluorescence particle tracking,” *Biophysical Journal*, vol. 121, no. 24, 2022.
- [93] F. Rothfischer, M. Vogt, E. Kopperger, U. Gerland, and F. C. Simmel, “From brownian to deterministic motor movement in a dna-based molecular rotor,” *Nano Letters*, 2024.
- [94] S. Lauback, K. R. Mattioli, A. E. Marras, *et al.*, “Real-time magnetic actuation of dna nanodevices via modular integration with stiff micro-levers,” *Nature communications*, vol. 9, no. 1, 2018.
- [95] M. A. Götzfried, “Towards molecular machines: Dynamic dna nanostructures actuated by hydrophobic and magnetic stimuli,” Ph.D. dissertation, Technische Universität München, 2021.
- [96] M. Lin, J.-u. Lee, Y. Kim, *et al.*, “A magnetically powered nanomachine with a dna clutch,” *Nature Nanotechnology*, 2024.
- [97] M. Endo and H. Sugiyama, “Dna origami nanomachines,” *Molecules*, vol. 23, no. 7, 2018.
- [98] 13.06.2024. [Online]. Available: <https://www.cytivalifesciences.com/en/de>.
- [99] J. W. Tavecchi, J. Heuvingh, and O. Du Roure, “Assembly modulated by particle position and shape: A new concept in self-assembly,” *Materials*, vol. 10, no. 11, 2017.

- [100] S. Dey, C. Fan, K. V. Gothelf, *et al.*, “Dna origami,” *Nature Reviews Methods Primers*, vol. 1, no. 1, Jan. 2021, ISSN: 2662-8449. DOI: 10.1038/s43586-020-00009-8. [Online]. Available: <https://doi.org/10.1038/s43586-020-00009-8>.
- [101] S. Takami, “Surface modification of inorganic nanoparticles by organic functional groups,” in *Nanoparticle technology handbook*, Elsevier, 2018.
- [102] G. Pacchioni, “A not-so-strong bond,” *Nature Reviews Materials*, vol. 4, no. 4, Apr. 2019, ISSN: 2058-8437. DOI: 10.1038/s41578-019-0094-3. [Online]. Available: <https://doi.org/10.1038/s41578-019-0094-3>.
- [103] K. F. Wagenbauer, F. A. Engelhardt, E. Stahl, *et al.*, “How we make dna origami,” *ChemBioChem*, vol. 18, no. 19, 2017.
- [104] E. Stahl, T. G. Martin, F. Praetorius, and H. Dietz, “Facile and scalable preparation of pure and dense dna origami solutions,” *Angewandte Chemie*, vol. 126, no. 47, 2014.
- [105] 13.06.2024. [Online]. Available: <https://www.biochempeg.com/product/Silane-PEG-Biotin.html>.
- [106] “Phase contrast microscopy and darkfield microscopy,” in *Fundamentals of Light Microscopy and Electronic Imaging*. John Wiley Sons, Ltd, 2012, ch. 7. DOI: <https://doi.org/10.1002/9781118382905.ch7>. [Online]. Available: <https://onlinelibrary.wiley.com/doi/abs/10.1002/9781118382905.ch7>.
- [107] “Fluorescence microscopy,” in *Fundamentals of Light Microscopy and Electronic Imaging*. John Wiley Sons, Ltd, 2012, ch. 11. DOI: <https://doi.org/10.1002/9781118382905.ch11>. [Online]. Available: <https://onlinelibrary.wiley.com/doi/abs/10.1002/9781118382905.ch11>.
- [108] 18.05.2024. [Online]. Available: <https://www.edinst.com/blog/what-is-the-stokes-shift/>.
- [109] “Fluorescence imaging of dynamic molecular processes,” in *Fundamentals of Light Microscopy and Electronic Imaging*. John Wiley Sons, Ltd, 2012, ch. 12. DOI: <https://doi.org/10.1002/9781118382905.ch12>. [Online]. Available: <https://onlinelibrary.wiley.com/doi/abs/10.1002/9781118382905.ch12>.
- [110] “Diffraction and spatial resolution,” in *Fundamentals of Light Microscopy and Electronic Imaging*. John Wiley Sons, Ltd, 2012, ch. 6. DOI: <https://doi.org/10.1002/9781118382905.ch6>. [Online]. Available: <https://onlinelibrary.wiley.com/doi/abs/10.1002/9781118382905.ch6>.

-
- [111] S. Amelinckx and J. Van Landuyt, “Transmission electron microscopy,” in *Encyclopedia of Physical Science and Technology (Third Edition)*, R. A. Meyers, Ed., Third Edition, New York: Academic Press, 2003. DOI: <https://doi.org/10.1016/B0-12-227410-5/00789-4>. [Online]. Available: <https://www.sciencedirect.com/science/article/pii/B0122274105007894>.
- [112] 12.06.2024. [Online]. Available: <https://www.microscopeclub.com/bright-field-microscope/>.
- [113] 12.06.2024. [Online]. Available: <https://www.olympus-ims.com/de/microscope/terms/feature14/>.
- [114] 12.06.2024. [Online]. Available: <https://www.laserfocusworld.com/biooptics/bioimaging/microscopy/article/14190504/perfecting-tirf-optics>.
- [115] 12.06.2024. [Online]. Available: <https://www.technologynetworks.com/analysis/articles/sem-vs-tem-331262>.
- [116] P. Liao, L. Xing, S. Zhang, and D. Sun, “Magnetically driven undulatory microswimmers integrating multiple rigid segments,” *Small*, vol. 15, no. 36, 2019.
- [117] P. Bauër, J. Tavacoli, T. Pujol, J. Planade, J. Heuvingh, and O. Du Roure, “A new method to measure mechanics and dynamic assembly of branched actin networks,” *Scientific reports*, vol. 7, no. 1, 2017.
- [118] J. Schnitzbauer, M. T. Strauss, T. Schlichthaerle, F. Schueder, and R. Jungmann, “Super-resolution microscopy with dna-paint,” *Nature Protocols*, vol. 12, no. 6, Jun. 2017, ISSN: 1750-2799. DOI: 10.1038/nprot.2017.024. [Online]. Available: <https://doi.org/10.1038/nprot.2017.024>.
- [119] 18.05.2024. [Online]. Available: <https://github.com/jungmannlab/picasso>.
- [120] L. Koens and T. D. Montenegro-Johnson, “Local drag of a slender rod parallel to a plane wall in a viscous fluid,” *Phys. Rev. Fluids*, vol. 6, 6 Jun. 2021. DOI: 10.1103/PhysRevFluids.6.064101. [Online]. Available: <https://link.aps.org/doi/10.1103/PhysRevFluids.6.064101>.
- [121] J. Lipfert, J. W. J. Kerssemakers, T. Jager, and N. H. Dekker, “Magnetic torque tweezers: Measuring torsional stiffness in dna and reca-dna filaments,” *Nature Methods*, vol. 7, no. 12, Dec. 2010, ISSN: 1548-7105. DOI: 10.1038/nmeth.1520. [Online]. Available: <https://doi.org/10.1038/nmeth.1520>.
- [122] K. Lang, *Investigation of dynamic nano control of dna origami using magnetic fields*, Master’s thesis, 2023.